

Cylindrical wave pattern produced in a ripple tank. When not modified by the no-slip condition at solid surfaces, waves are nearly inviscid and well represented by the potential theory of this chapter. (Courtesy of Dr. E. R. Degginger/Color-Pic Inc.)

Chapter 8

Potential Flow and Computational Fluid Dynamics

Motivation. The basic partial differential equations of mass, momentum, and energy were discussed in Chap. 4. A few solutions were then given for incompressible *potential* flow in Sec. 4.10 and for incompressible *viscous* flow in Sec. 4.11. The viscous solutions were limited to simple geometries and unidirectional flows, where the difficult nonlinear convective terms were neglected. The potential flows were not limited by such nonlinear terms. Then, in Chap. 7, we found an approximation: patching *boundary-layer flows* onto an outer inviscid flow pattern. For more complicated viscous flows, we found no theory or solutions, just experimental data.

The purposes of the present chapter are (1) to explore more examples of potential theory and (2) to indicate some flows which can be approximated by computational fluid dynamics (CFD). The combination of these two gives us a good picture of incompressible-flow theory and its relation to experiment. One of the most important applications of potential-flow theory is to aerodynamics and marine hydrodynamics. First, however, we will review and extend the concepts of Sec. 4.10.

8.1 Introduction and Review

Figure 8.1 reminds us of the problems to be faced. A free stream approaches two closely spaced bodies, creating an “internal” flow between them and “external” flows above and below them. The fronts of the bodies are regions of favorable gradient (decreasing pressure along the surface), and the boundary layers will be attached and thin: Inviscid theory will give excellent results for the outer flow if $Re > 10^4$. For the internal flow between bodies, the boundary layers will grow and eventually meet, and the inviscid core vanishes. Inviscid theory works well in a “short” duct $L/D < 10$, such as the nozzle of a wind tunnel. For longer ducts we must estimate boundary-layer growth and be cautious about using inviscid theory.

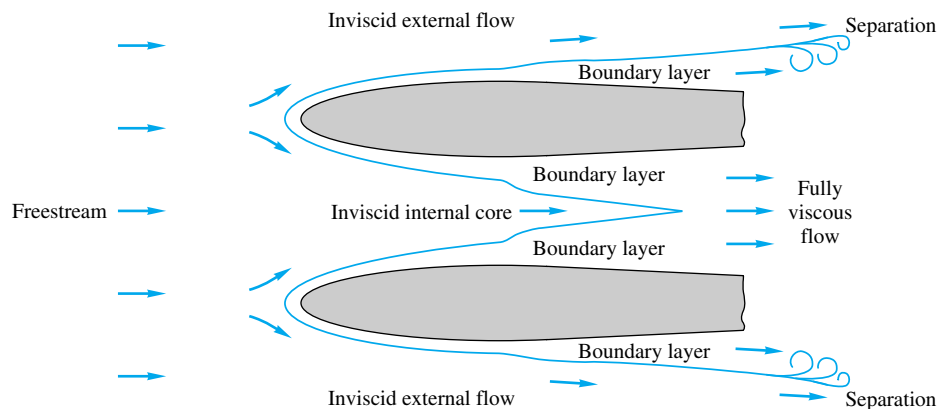


Fig. 8.1 Patching viscous- and inviscid-flow regions. Potential theory in this chapter does not apply to the boundary-layer regions

For the external flows above and below the bodies in Fig. 8.1, inviscid theory should work well for the outer flows, until the surface pressure gradient becomes adverse (increasing pressure) and the boundary layer separates or stalls. After the separation point, boundary-layer theory becomes inaccurate, and the outer flow streamlines are deflected and have a strong interaction with the viscous near-wall regions. The theoretical analysis of separated-flow regions is an active research area at present.

Review of Velocity-Potential Concepts

Recall from Sec. 4.9 that if viscous effects are neglected, low-speed flows are irrotational, $\nabla \times \mathbf{V} = 0$, and the velocity potential ϕ exists, such that

$$\mathbf{V} = \nabla \phi \quad \text{or} \quad u = \frac{\partial \phi}{\partial x} \quad v = \frac{\partial \phi}{\partial y} \quad w = \frac{\partial \phi}{\partial z} \quad (8.1)$$

The continuity equation (4.73), $\nabla \cdot \mathbf{V} = 0$, reduces to Laplace's equation for ϕ :

$$\nabla^2 \phi = \frac{\partial^2 \phi}{\partial x^2} + \frac{\partial^2 \phi}{\partial y^2} + \frac{\partial^2 \phi}{\partial z^2} = 0 \quad (8.2)$$

and the momentum equation (4.74) reduces to Bernoulli's equation:

$$\frac{\partial \phi}{\partial t} + \frac{p}{\rho} + \frac{1}{2} V^2 + gz = \text{const} \quad \text{where } V = |\nabla \phi| \quad (8.3)$$

Typical boundary conditions are known free-stream conditions

$$\text{Outer boundaries:} \quad \text{Known } \frac{\partial \phi}{\partial x}, \frac{\partial \phi}{\partial y}, \frac{\partial \phi}{\partial z} \quad (8.4)$$

and no velocity normal to the boundary at the body surface:

$$\text{Solid surfaces:} \quad \frac{\partial \phi}{\partial n} = 0 \quad \text{where } n \text{ is perpendicular to body} \quad (8.5)$$

Unlike the no-slip condition in viscous flow, here there is *no* condition on the tangential surface velocity $V_s = \partial \phi / \partial s$, where s is the coordinate along the surface. This velocity is determined as part of the solution to the problem.

Occasionally the problem involves a free surface, for which the boundary pressure is known and equal to p_a , usually a constant. The Bernoulli equation (8.3) then supplies a relation at the surface between V and the elevation z of the surface. For steady flow, e.g.,

$$\text{Free surface:} \quad V^2 = |\nabla\phi|^2 = \text{const} - 2gz_{\text{surf}} \quad (8.6)$$

It should be clear to the reader that this use of Laplace's equation, with known values of the derivative of ϕ along the boundaries, is much easier than a direct attack using the fully viscous Navier-Stokes equations. The analysis of Laplace's equation is very well developed and is termed *potential theory*, with whole books written about the general theory [1] and its application to fluid mechanics [2 to 4]. There are many analytical techniques, including superposition of elementary functions, conformal mapping, numerical finite differences [5], numerical finite elements [6], numerical boundary elements [7], and electric or mechanical analogs [8] now outdated. Having found $\phi(x, y, z, t)$ from such an analysis, we then compute \mathbf{V} by direct differentiation in Eq. (8.1), after which we compute p from Eq. (8.3). The procedure is quite straightforward, and many interesting albeit idealized results can be obtained.

Review of Stream Function Concepts

Recall from Sec. 4.7 that if a flow is described by only two coordinates, the stream function ψ also exists as an alternate approach. For plane incompressible flow in xy coordinates, the correct form is

$$u = \frac{\partial\psi}{\partial y} \quad v = -\frac{\partial\psi}{\partial x} \quad (8.7)$$

The condition of irrotationality reduces to Laplace's equation for ψ also:

$$2\omega_z = 0 = \frac{\partial v}{\partial x} - \frac{\partial u}{\partial y} = \frac{\partial}{\partial x} \left(-\frac{\partial\psi}{\partial x} \right) - \frac{\partial}{\partial y} \left(\frac{\partial\psi}{\partial y} \right)$$

$$\text{or} \quad \frac{\partial^2\psi}{\partial x^2} + \frac{\partial^2\psi}{\partial y^2} = 0 \quad (8.8)$$

The boundary conditions again are known velocity in the stream and no flow through any solid surface:

$$\text{Free stream:} \quad \text{Known } \frac{\partial\psi}{\partial x}, \frac{\partial\psi}{\partial y} \quad (8.9a)$$

$$\text{Solid surface:} \quad \psi_{\text{body}} = \text{const} \quad (8.9b)$$

Equation (8.9b) is particularly interesting because *any* line of constant ψ in a flow can therefore be interpreted as a body shape and may lead to interesting applications.

For the applications in this chapter, we may compute either ϕ or ψ or both, and the solution will be an *orthogonal flow net* as in Fig. 8.2. Once found, either set of lines may be considered the ϕ lines, and the other set will be the ψ lines. Both sets of lines are laplacian and could be useful.

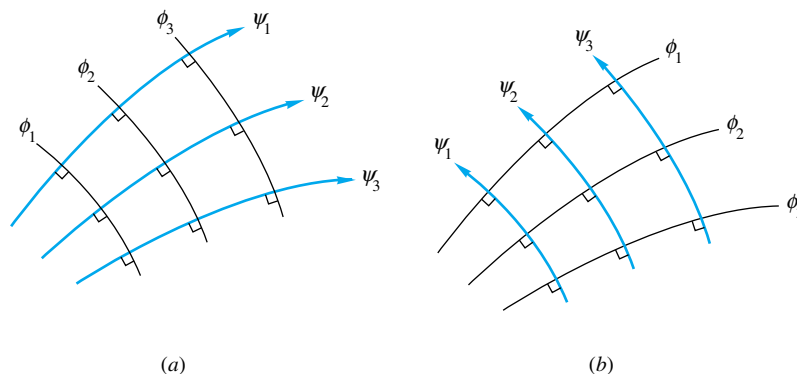


Fig. 8.2 Streamlines and potential lines are orthogonal and may reverse roles if results are useful: (a) typical inviscid-flow pattern; (b) same as (a) with roles reversed.

Plane Polar Coordinates

Many solutions in this chapter are conveniently expressed in polar coordinates (r, θ) . Both the velocity components and the differential relations for ϕ and ψ are then changed, as follows:

$$v_r = \frac{\partial \phi}{\partial r} = \frac{1}{r} \frac{\partial \psi}{\partial \theta} \quad v_\theta = \frac{1}{r} \frac{\partial \phi}{\partial \theta} = -\frac{\partial \psi}{\partial r} \quad (8.10)$$

Laplace's equation takes the form

$$\frac{1}{r} \frac{\partial}{\partial r} \left(r \frac{\partial \phi}{\partial r} \right) + \frac{1}{r^2} \frac{\partial^2 \phi}{\partial \theta^2} = 0 \quad (8.11)$$

Exactly the same equation holds for the polar-coordinate form of $\psi(r, \theta)$.

An intriguing facet of potential flow with no free surface is that the governing equations (8.2) and (8.8) contain no parameters, nor do the boundary conditions. Therefore the solutions are purely geometric, depending only upon the body shape, the free-stream orientation, and—surprisingly—the position of the rear stagnation point.¹ There is no Reynolds, Froude, or Mach number to complicate the dynamic similarity. Inviscid flows are kinematically similar without additional parameters—recall Fig. 5.6a.

8.2 Elementary Plane-Flow Solutions

Recall from Sec. 4.10 that we defined three elementary potential flows which are quite useful: (1) uniform stream in the x direction, (2) line source or sink at the origin, and (3) line vortex at the origin. (Recall Fig. 4.12 for these geometries.) Let us review these special cases here:

$$\text{Uniform stream } \mathbf{i}U: \quad \psi = Uy \quad \phi = Ux \quad (8.12a)$$

$$\text{Line source or sink:} \quad \psi = m\theta \quad \phi = m \ln r \quad (8.12b)$$

$$\text{Line vortex:} \quad \psi = -K \ln r \quad \phi = K\theta \quad (8.12c)$$

¹ The rear stagnation condition establishes the net amount of “circulation” about the body, giving rise to a lift force. Otherwise the solution could not be unique. See Sec. 8.4.

The source “strength” m and the vortex “strength” K have the same dimensions, namely, velocity times length, or $\{L^2/T\}$.

If the uniform stream is written in plane polar coordinates, it becomes

$$\text{Uniform stream } \mathbf{i}U: \quad \psi = Ur \sin \theta \quad \phi = Ur \cos \theta \quad (8.13)$$

This makes it easier to superimpose, say, a stream and a source or vortex by using the same coordinates. If the uniform stream is moving at angle α with respect to the x -axis, i.e.,

$$u = U \cos \alpha = \frac{\partial \psi}{\partial y} = \frac{\partial \phi}{\partial x} \quad v = U \sin \alpha = -\frac{\partial \psi}{\partial x} = \frac{\partial \phi}{\partial y}$$

then by integration we obtain the correct functions for flow at an angle:

$$\psi = U(y \cos \alpha - x \sin \alpha) \quad \phi = U(x \cos \alpha + y \sin \alpha) \quad (8.14)$$

These expressions are useful in airfoil angle-of-attack problems (Sec. 8.7).

Circulation

The line-vortex flow is irrotational everywhere except at the origin, where the vorticity $\nabla \times \mathbf{V}$ is infinite. This means that a certain line integral called the *fluid circulation* Γ does not vanish when taken around a vortex center.

With reference to Fig. 8.3, the circulation is defined as the counterclockwise line integral, around a closed curve C , of arc length ds times the velocity component tangent to the curve

$$\Gamma = \oint_C V \cos \alpha \, ds = \int_C \mathbf{V} \cdot d\mathbf{s} = \int_C (u \, dx + v \, dy + w \, dz) \quad (8.15)$$

From the definition of ϕ , $\mathbf{V} \cdot d\mathbf{s} = \nabla \phi \cdot d\mathbf{s} = d\phi$ for an irrotational flow; hence normally Γ in an irrotational flow would equal the final value of ϕ minus the initial value of ϕ . Since we start and end at the same point, we compute $\Gamma = 0$, but not for vortex flow: With $\phi = K\theta$ from Eq. (8.12c) there is a change in ϕ of amount $2\pi K$ as we make one complete circle:

$$\text{Path enclosing a vortex:} \quad \Gamma = 2\pi K \quad (8.16)$$

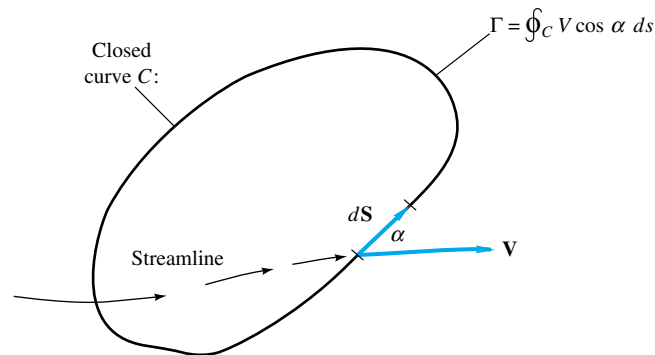


Fig. 8.3 Definition of the fluid circulation Γ .

Alternately the calculation can be made by defining a circular path of radius r around the vortex center, from Eq. (8.15)

$$\Gamma = \int_C v_\theta ds = \int_0^{2\pi} \frac{K}{r} r d\theta = 2\pi K \quad (8.17)$$

In general, Γ denotes the net algebraic strength of all the vortex filaments contained within the closed curve. In the next section we shall see that a region of finite circulation within a flowing stream will be subjected to a lift force proportional to both U_∞ and Γ .

It is easy to show, by using Eq. (8.15), that a source or sink creates no circulation. If there are no vortices present, the circulation will be zero for any path enclosing any number of sources and sinks.

8.3 Superposition of Plane-Flow Solutions

We can now form a variety of interesting potential flows by summing the velocity-potential and stream functions of a uniform stream, source or sink, and vortex. Most of the results are classic, of course, needing only a brief treatment here.

Graphical Method of Superposition

A simple means of accomplishing $\psi_{\text{tot}} = \sum \psi_i$ graphically is to plot the individual stream functions separately and then look at their intersections. The value of ψ_{tot} at each intersection is the sum of the individual values ψ_i which cross there. Connecting intersections with the same value of ψ_{tot} creates the desired superimposed flow streamlines.

A simple example is shown in Fig. 8.4, summing two families of streamlines ψ_a and ψ_b . The individual components are plotted separately, and four typical intersections are shown. Dashed lines are then drawn through intersections representing the same sum of $\psi_a + \psi_b$. These dashed lines are the desired solution. Often this graphical method is a quick means of evaluating the proposed superposition before a full-blown numerical plot routine is executed.

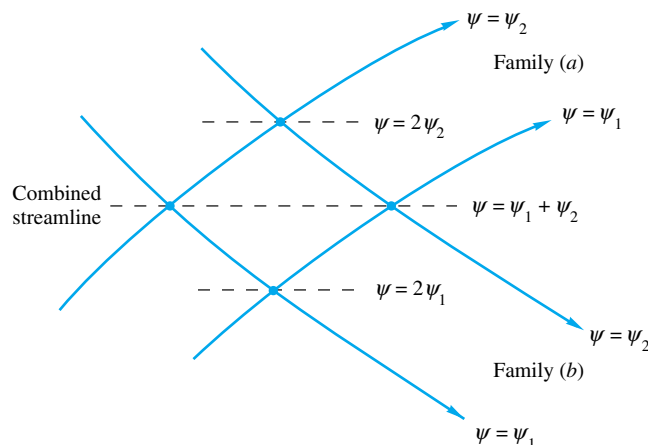


Fig. 8.4 Intersections of elementary streamlines can be joined to form a combined streamline.

Some Examples from Chap. 4

In Sec. 4.10 we discussed a number of superposition examples.

1. Source m at $(-a, 0)$ plus an equal sink at $(+a, 0)$, Eq. (4.133), and Fig. 4.13:

$$\psi = -m \tan^{-1} \frac{2ay}{x^2 + y^2 - a^2} \quad \phi = \frac{1}{2} m \ln \frac{(x+a)^2 + y^2}{(x-a)^2 + y^2} \quad (4.133)$$

The streamlines and potential lines are two families of orthogonal circles as plotted in Fig. 4.13. They resemble a magnet with poles at $(x, y) = (\pm a, 0)$.

2. Sink m plus a vortex K , both at the origin, Eq. (4.134), and Fig. 4.14:

$$\psi = m\theta - K \ln r \quad \phi = m \ln r + K\theta \quad (4.134)$$

The streamlines are logarithmic spirals swirling into the origin, as in Fig. 4.14. They resemble a tornado or a bathtub vortex.

3. Uniform stream iU_∞ plus a source m at the origin, Eq. (4.135) and Fig. 4.15, the Rankine half-body:

$$\psi = U_\infty r \sin \theta + m\theta \quad \phi = U_\infty r \cos \theta + m \ln r \quad (4.135)$$

If the origin contains a source, a plane half-body is formed with its nose to the left, as in Fig. 8.5a. If the origin is a sink, $m < 0$, the half-body nose is to the right, as in Fig. 8.5c. In either case the stagnation point is at a position $a = m/U_\infty$ away from the origin.

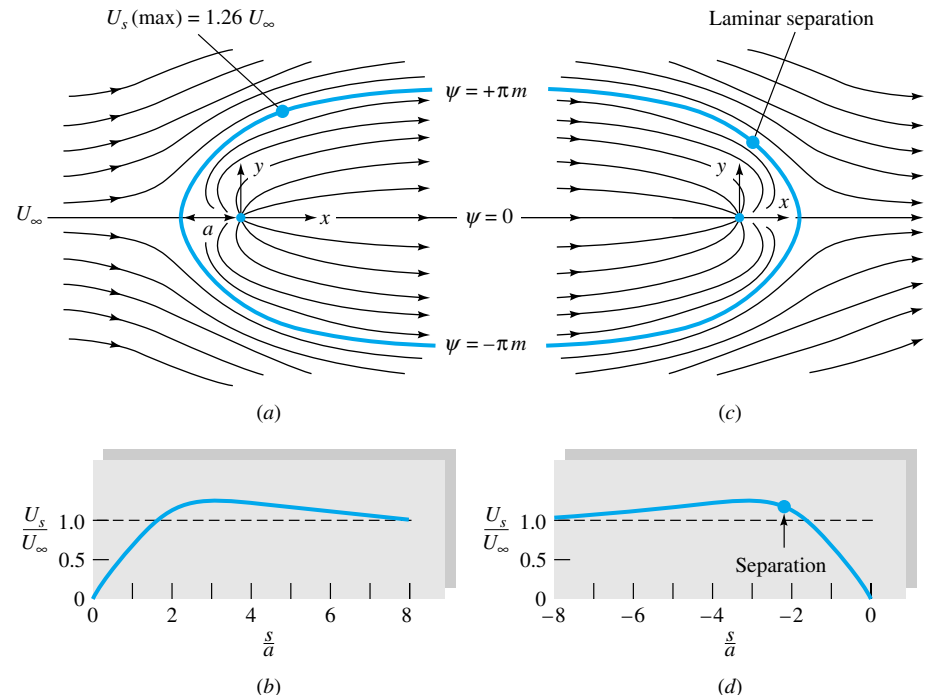


Fig. 8.5 The Rankine half-body; pattern (c) is not found in a real fluid because of boundary-layer separation: (a) uniform stream plus a source equals a half-body; stagnation point at $x = -a = -m/U_\infty$; (b) slight adverse gradient for s/a greater than 3.0: no separation; (c) uniform stream plus a sink equals the rear of a half-body; stagnation point at $x = a = m/U_\infty$; (d) strong adverse gradient for $s/a > -3.0$: separation.

Boundary-Layer Separation on a Half-Body

Although the inviscid-flow patterns, Fig. 8.5*a* and *c*, are mirror images, their viscous (boundary-layer) behavior is different. The body shape and the velocity along the surface are repeated here from Sec. 4.10:

$$V^2 = U_\infty^2 \left(1 + \frac{a^2}{r^2} + \frac{2a}{r} \cos \theta \right) \quad \text{along} \quad r = \frac{m(\pi - \theta)}{U_\infty \sin \theta} \quad (8.18)$$

The computed surface velocities are plotted along the half-body contours in Fig. 8.5*b* and *d* as a function of arc length s/a measured from the stagnation point. These plots are also mirror images. However, if the nose is in front, Fig. 8.5*b*, the pressure gradient there is *favorable* (decreasing pressure along the surface). In contrast, the pressure gradient is *adverse* (increasing pressure along the surface) when the nose is in the rear, Fig. 8.5*d*, and boundary-layer separation may occur.

Application to Fig. 8.5*b* of Thwaites' laminar-boundary method from Eqs. (7.54) and (7.56) reveals that separation does not occur on the front nose of the half-body. Therefore Fig. 8.5*a* is a very realistic picture of streamlines past a half-body nose. In contrast, when applied to the tail, Fig. 8.5*c*, Thwaites' method predicts separation at about $s/a \approx -2.2$, or $\theta \approx 110^\circ$. Thus, if a half-body is a solid surface, Fig. 8.5*c* is *not* realistic and a broad separated wake will form. However, if the half-body tail is a *fluid line* separating the sink-directed flow from the outer stream, as in Example 8.1, then Fig. 8.5*c* is quite realistic and useful. Computations for turbulent boundary-layer theory would be similar: separation on the tail, no separation on the nose.

EXAMPLE 8.1

An offshore power plant cooling-water intake sucks in $1500 \text{ ft}^3/\text{s}$ in water 30 ft deep, as in Fig. E8.1. If the tidal velocity approaching the intake is 0.7 ft/s , (a) how far downstream does the intake effect extend and (b) how much width L of tidal flow is entrained into the intake?

Solution

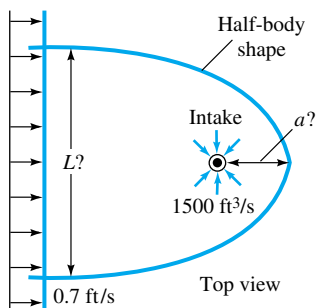
Recall from Eq. (4.131) that the sink strength m is related to the volume flow Q and the depth b into the paper

$$m = \frac{Q}{2\pi b} = \frac{1500 \text{ ft}^3/\text{s}}{2\pi(30 \text{ ft})} = 7.96 \text{ ft}^2/\text{s}$$

Therefore from Fig. 8.5 the desired lengths a and L are

$$a = \frac{m}{U_\infty} = \frac{7.96 \text{ ft}^2/\text{s}}{0.7 \text{ ft/s}} = 11.4 \text{ ft} \quad \text{Ans. (a)}$$

$$L = 2\pi a = 2\pi(11.4 \text{ ft}) = 71 \text{ ft} \quad \text{Ans. (b)}$$



E8.1

Flow Past a Vortex

Consider a uniform stream U_∞ in the x direction flowing past a vortex of strength K with center at the origin. By superposition the combined stream function is

$$\psi = \psi_{\text{stream}} + \psi_{\text{vortex}} = U_\infty r \sin \theta - K \ln r \quad (8.19)$$

The velocity components are given by

$$v_r = \frac{1}{r} \frac{\partial \psi}{\partial \theta} = U_\infty \cos \theta \quad v_\theta = -\frac{\partial \psi}{\partial r} = -U_\infty \sin \theta + \frac{K}{r} \quad (8.20)$$

The streamlines are plotted in Fig. 8.6 by the graphical method, intersecting the circular streamlines of the vortex with the horizontal lines of the uniform stream.

By setting $v_r = v_\theta = 0$ from (8.20) we find a stagnation point at $\theta = 90^\circ$, $r = a = K/U_\infty$, or $(x, y) = (0, a)$. This is where the counterclockwise vortex velocity K/r exactly cancels the stream velocity U_∞ .

Probably the most interesting thing about this example is that there is a nonzero lift force normal to the stream on the surface of any region enclosing the vortex, but we postpone this discussion until the next section.

An Infinite Row of Vortices

Consider an infinite row of vortices of equal strength K and equal spacing a , as in Fig. 8.7a. This case is included here to illustrate the interesting concept of a *vortex sheet*.

From Eq. (8.12c), the i th vortex in Fig. 8.7a has a stream function $\psi_i = -K \ln r_i$, so that the total infinite row has a combined stream function

$$\psi = -K \sum_{i=1}^{\infty} \ln r_i \quad (8.21)$$

It can be shown [2, sec. 4.51] that this infinite sum of logarithms is equivalent to a closed-form function

$$\psi = -\frac{1}{2}K \ln \left[\frac{1}{2} \left(\cosh \frac{2\pi y}{a} - \cos \frac{2\pi x}{a} \right) \right] \quad (8.22)$$

Since the proof uses the complex variable $z = x + iy$, $i = (-1)^{1/2}$, we are not going to show the details here.

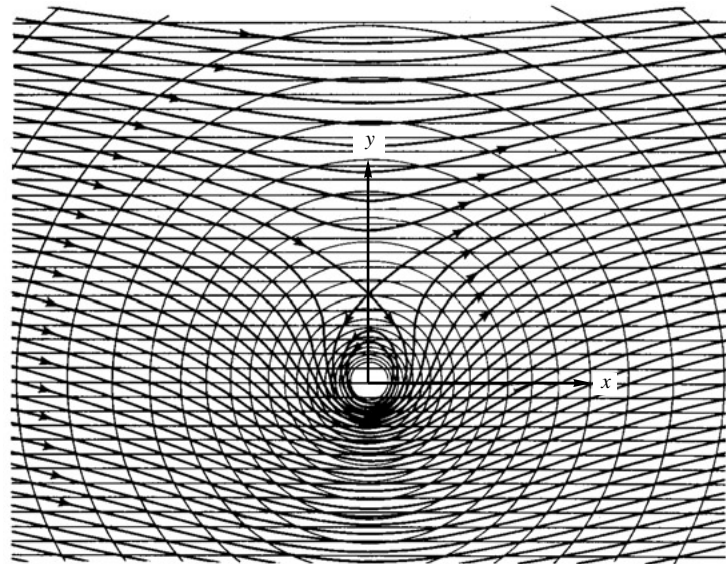


Fig. 8.6 Flow of a uniform stream past a vortex constructed by the graphical method.

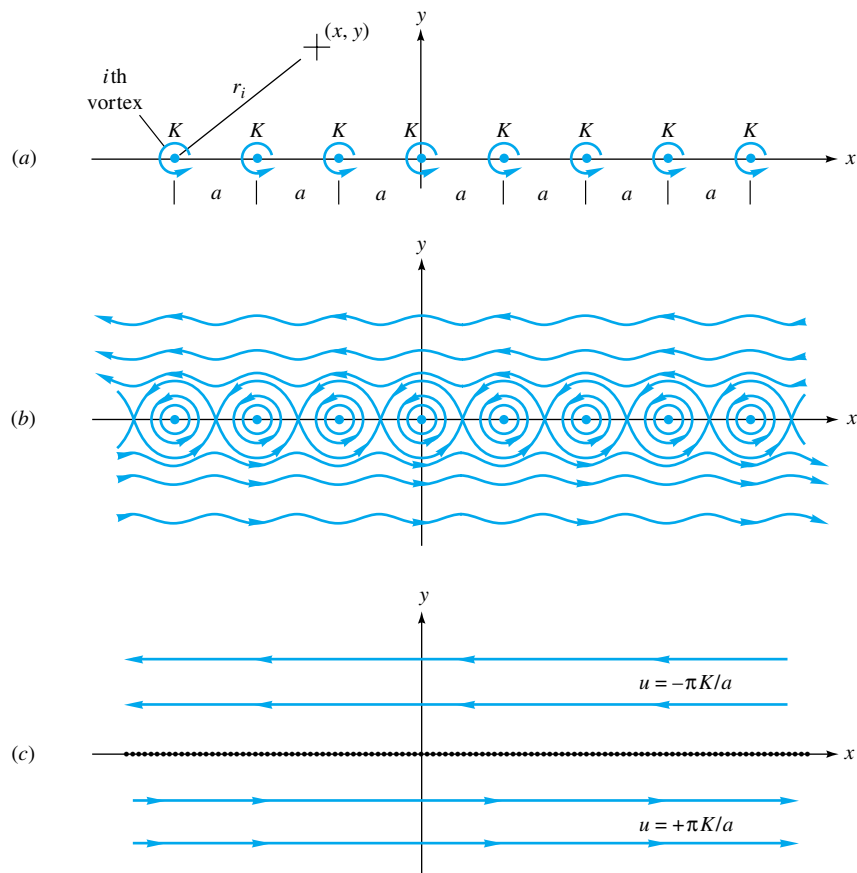


Fig. 8.7 Superposition of vortices: (a) an infinite row of equal strength; (b) streamline pattern for part (a); (c) vortex sheet: part (b) viewed from afar.

The streamlines from Eq. (8.22) are plotted in Fig. 8.7*b*, showing what is called a *cat's-eye* pattern of enclosed flow cells surrounding the individual vortices. Above the cat's eyes the flow is entirely to the left, and below the cat's eyes the flow is to the right. Moreover, these left and right flows are uniform if $|y| \gg a$, which follows by differentiating Eq. (8.22)

$$u = \frac{\partial \psi}{\partial y} \Big|_{|y| \gg a} = \pm \frac{\pi K}{a} \quad (8.23)$$

where the plus sign applies below the row and the minus sign above the row. This uniform left and right streaming is sketched in Fig. 8.7*c*. We stress that this effect is induced by the row of vortices: There is no uniform stream approaching the row in this example.

The Vortex Sheet

When Fig. 8.7*b* is viewed from afar, the streaming motion is uniform left above and uniform right below, as in Fig. 8.7*c*, and the vortices are packed so closely together

that they are smudged into a continuous *vortex sheet*. The strength of the sheet is defined as

$$\gamma = \frac{2\pi K}{a} \quad (8.24)$$

and in the general case γ can vary with x . The circulation about any closed curve which encloses a short length dx of the sheet would be, from Eqs. (8.15) and (8.23),

$$d\Gamma = u_l dx - u_u dx = (u_l - u_u) dx = \frac{2\pi K}{a} dx = \gamma dx \quad (8.25)$$

where the subscripts l and u stand for lower and upper, respectively. Thus the sheet strength $\gamma = d\Gamma/dx$ is the circulation per unit length of the sheet. Thus when a vortex sheet is immersed in a uniform stream, γ is proportional to the lift per unit length of any surface enclosing the sheet.

Note that there is no velocity normal to the sheet at the sheet surface. Therefore a vortex sheet can simulate a thin-body shape, e.g., plate or thin airfoil. This is the basis of the thin-airfoil theory mentioned in Sec. 8.7.

The Doublet

As we move far away from the source-sink pair of Fig. 4.13, the flow pattern begins to resemble a family of circles tangent to the origin, as in Fig. 8.8. This limit of vanishingly small distance a is called a *doublet*. To keep the flow strength large enough to exhibit decent velocities as a becomes small, we specify that the product $2am$ remain constant. Let us call this constant λ . Then the stream function of a doublet is

$$\psi = \lim_{\substack{a \rightarrow 0 \\ 2am = \lambda}} \left(-m \tan^{-1} \frac{2ay}{x^2 + y^2 - a^2} \right) = -\frac{2amy}{x^2 + y^2} = -\frac{\lambda y}{x^2 + y^2} \quad (8.26)$$

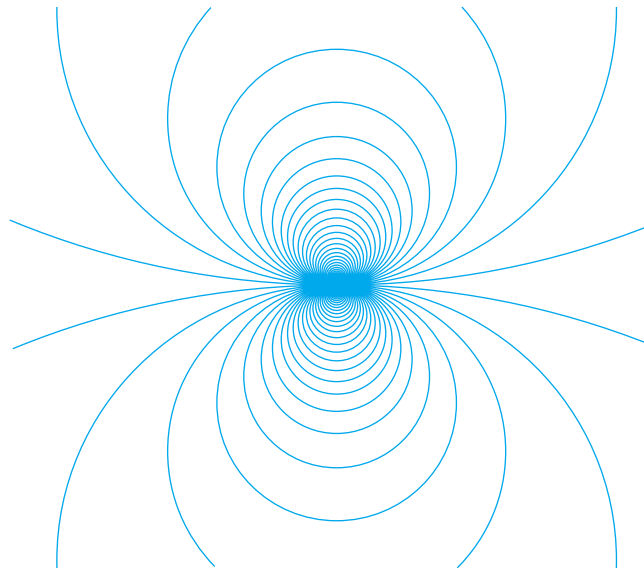


Fig. 8.8 A doublet, or source-sink pair, is the limiting case of Fig. 4.13 viewed from afar. Streamlines are circles tangent to the x -axis at the origin. This figure was prepared using the *contour* feature of MATLAB [34, 35].

We have used the fact that $\tan^{-1} \alpha \approx \alpha$ as α becomes small. The quantity λ is called the *strength* of the doublet.

Equation (8.26) can be rearranged to yield

$$x^2 + \left(y + \frac{\lambda}{2\psi}\right)^2 = \left(\frac{\lambda}{2\psi}\right)^2$$

so that, as advertised, the streamlines are circles tangent to the origin with centers on the y -axis. This pattern is sketched in Fig. 8.8.

Although the author has in the past laboriously sketched streamlines by hand, this is no longer necessary. Figure 8.8 was computer-drawn, using the *contour* feature of the student version of MATLAB [35]. Simply set up a grid of points, spell out the stream function, and call for a contour. For Fig. 8.8, the actual statements were

```
[X,Y] = meshgrid(-1:.02:1);
PSI = -Y./(X.^2 + Y.^2);
contour(X,Y,PSI,100)
```

This would produce 100 contour lines of ψ from Eq. (8.26), with $\lambda = 1$ for convenience. The plot would include grid lines, scale markings, and a surrounding box, and the circles might look a bit elliptical. These blemishes can be eliminated with three statements of cosmetic improvement:

```
axis square
grid off
axis off
```

The final plot, Fig. 8.8, has no markings but the streamlines themselves. MATLAB is thus a recommended tool and, in addition, has scores of other uses. All this chapter's problem assignments which call for "sketch the streamlines/potential lines" can be completed using this contour feature. For further details, consult Ref. 34.

In a similar manner the velocity potential of a doublet is found by taking the limit of Eq. (4.133) as $a \rightarrow 0$ and $2am = \lambda$

$$\phi_{\text{doublet}} = \frac{\lambda x}{x^2 + y^2}$$

or

$$\left(x - \frac{\lambda}{2\phi}\right)^2 + y^2 = \left(\frac{\lambda}{2\phi}\right)^2 \quad (8.27)$$

The potential lines are circles tangent to the origin with centers on the x -axis. Simply turn Fig. 8.8 clockwise 90° to visualize the ϕ lines, which are everywhere normal to the streamlines.

The doublet functions can also be written in polar coordinates

$$\psi = -\frac{\lambda \sin \theta}{r} \quad \phi = \frac{\lambda \cos \theta}{r} \quad (8.28)$$

These forms are convenient for the cylinder flows of the next section.

8.4 Plane Flow Past Closed-Body Shapes

A variety of closed-body external flows can be constructed by superimposing a uniform stream with sources, sinks, and vortices. The body shape will be closed only if the net source outflow equals the net sink inflow.

The Rankine Oval

A cylindrical shape called a *Rankine oval*, which is long compared with its height, is formed by a source-sink pair aligned parallel to a uniform stream, as in Fig. 8.9a.

From Eqs. (8.12a) and (4.133) the combined stream function is

$$\psi = U_{\infty}y - m \tan^{-1} \frac{2ay}{x^2 + y^2 - a^2} = U_{\infty}r \sin \theta + m(\theta_1 - \theta_2) \quad (8.29)$$

When streamlines of constant ψ are plotted from Eq. (8.29), an oval body shape appears, as in Fig. (8.9b). The half-length L and half-height h of the oval depend upon the relative strength of source and stream, i.e., the ratio $m/(U_{\infty}a)$, which equals 1.0 in Fig. 8.9b. The circulating streamlines inside the oval are uninteresting and not usually shown. The oval is the line $\psi = 0$.

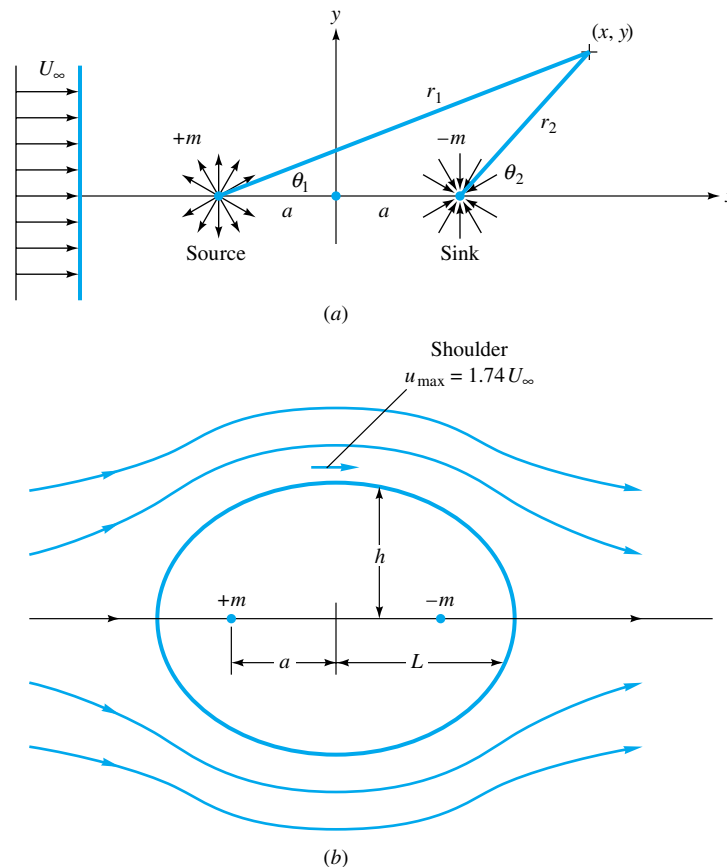


Fig. 8.9 Flow past a Rankine oval: (a) uniform stream plus a source-sink pair; (b) oval shape and streamlines for $m/(U_{\infty}a) = 1.0$.

There are stagnation points at the front and rear, $x = \pm L$, and points of maximum velocity and minimum pressure at the shoulders, $y = \pm h$, of the oval. All these parameters are a function of the basic dimensionless parameter $m/(U_\infty a)$, which we can determine from Eq. (8.29):

$$\frac{h}{a} = \cot \frac{h/a}{2m/(U_\infty a)} \quad \frac{L}{a} = \left(1 + \frac{2m}{U_\infty a}\right)^{1/2} \quad (8.30)$$

$$\frac{u_{\max}}{U_\infty} = 1 + \frac{2m/(U_\infty a)}{1 + h^2/a^2}$$

As we increase $m/(U_\infty a)$ from zero to large values, the oval shape increases in size and thickness from a flat plate of length $2a$ to a huge, nearly circular cylinder. This is shown in Table 8.1. In the limit as $m/(U_\infty a) \rightarrow \infty$, $L/h \rightarrow 1.0$ and $u_{\max}/U_\infty \rightarrow 2.0$, which is equivalent to flow past a circular cylinder.

All the Rankine ovals except very thin ones have a large adverse pressure gradient on their leeward surface. Thus boundary-layer separation will occur in the rear with a broad wake flow, and the inviscid pattern is unrealistic in that region.

Flow Past a Circular Cylinder with Circulation

From Table 8.1 at large source strength the Rankine oval becomes a large circle, much greater in diameter than the source-sink spacing $2a$. Viewed on the scale of the cylinder, this is equivalent to a uniform stream plus a doublet. We also throw in a vortex at the doublet center, which does not change the shape of the cylinder.

Thus the stream function for flow past a circular cylinder with circulation, centered at the origin, is a uniform stream plus a doublet plus a vortex

$$\psi = U_\infty r \sin \theta - \frac{\lambda \sin \theta}{r} - K \ln r + \text{const} \quad (8.31)$$

The doublet strength λ has units of velocity times length squared. For convenience, let $\lambda = U_\infty a^2$, where a is a length, and let the arbitrary constant in Eq. (8.31) equal $K \ln a$. Then the stream function becomes

$$\psi = U_\infty \sin \theta \left(r - \frac{a^2}{r} \right) - K \ln \frac{r}{a} \quad (8.32)$$

The streamlines are plotted in Fig. 8.10 for four different values of the dimensionless vortex strength $K/(U_\infty a)$. For all cases the line $\psi = 0$ corresponds to the circle $r =$

Table 8.1 Rankine-Oval Parameters from Eq. (8.30)

$m/(U_\infty a)$	h/a	L/a	L/h	u_{\max}/U_∞
0.0	0.0	1.0	∞	1.0
0.01	0.031	1.010	32.79	1.020
0.1	0.263	1.095	4.169	1.187
1.0	1.307	1.732	1.326	1.739
10.0	4.435	4.583	1.033	1.968
100.0	14.130	14.177	1.003	1.997
∞	∞	∞	1.000	2.000

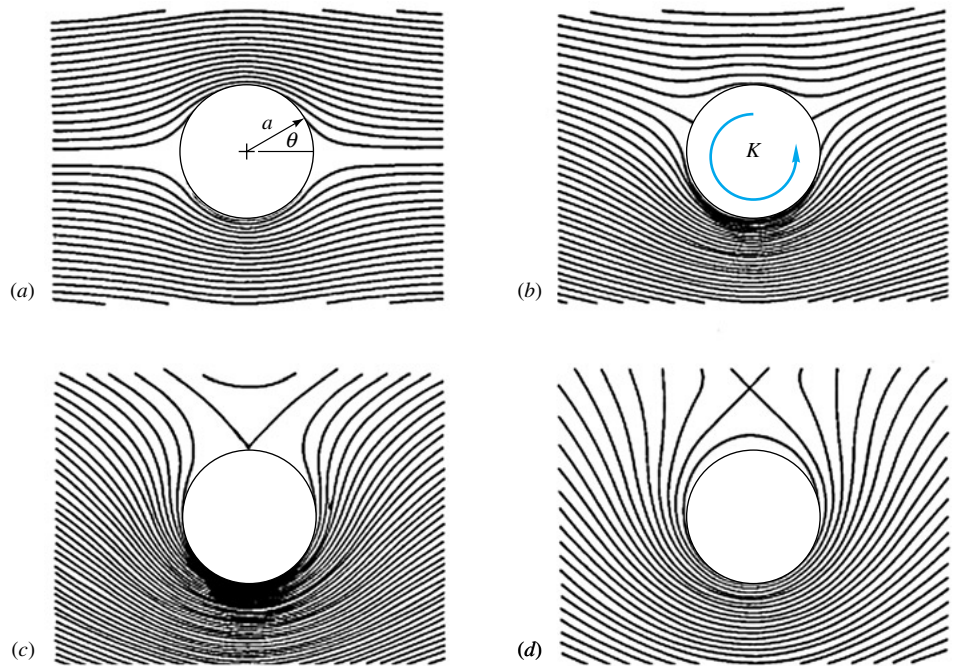


Fig. 8.10 Flow past a circular cylinder with circulation for values of $K/(U_\infty a)$ of (a) 0, (b) 1.0, (c) 2.0, and (d) 3.0.

a , that is, the shape of the cylindrical body. As circulation $\Gamma = 2\pi K$ increases, the velocity becomes faster and faster below the cylinder and slower and slower above it. The velocity components in the flow are given by

$$\begin{aligned} v_r &= \frac{1}{r} \frac{\partial \psi}{\partial \theta} = U_\infty \cos \theta \left(1 - \frac{a^2}{r^2} \right) \\ v_\theta &= -\frac{\partial \psi}{\partial r} = -U_\infty \sin \theta \left(1 + \frac{a^2}{r^2} \right) + \frac{K}{r} \end{aligned} \quad (8.33)$$

The velocity at the cylinder surface $r = a$ is purely tangential, as expected

$$v_r(r = a) = 0 \quad v_\theta(r = a) = -2U_\infty \sin \theta + \frac{K}{a} \quad (8.34)$$

For small K , two stagnation points appear on the surface at angles θ_s where $v_\theta = 0$, or, from Eq. (8.34),

$$\sin \theta_s = \frac{K}{2U_\infty a} \quad (8.35)$$

Figure 8.10a is for $K = 0$, $\theta_s = 0$ and 180° , or doubly symmetric inviscid flow past a cylinder with no circulation. Figure 8.10b is for $K/(U_\infty a) = 1$, $\theta_s = 30$ and 150° , and Fig. 8.10c is the limiting case where the two stagnation points meet at the top, $K/(U_\infty a) = 2$, $\theta_s = 90^\circ$.

For $K > 2U_\infty a$, Eq. (8.35) is invalid, and the single stagnation point is above the cylinder, as in Fig. 8.10d, at a point $y = h$ given by

$$\frac{h}{a} = \frac{1}{2} [\beta + (\beta^2 - 4)^{1/2}] \quad \beta = \frac{K}{U_\infty a} > 2 \quad (8.36)$$

In Fig. 8.10d, $K/(U_\infty a) = 3.0$, and $h/a = 2.6$.

The Kutta-Joukowski Lift Theorem

For the cylinder flows of Fig. 8.10b to d there is a downward force, or negative lift, called the *Magnus effect*, which is proportional to stream velocity and vortex strength. We can see from the streamline pattern that the velocity on the top of the cylinder is less and therefore the pressure higher from Bernoulli's equation; this explains the force. There is no viscous force, of course, because our theory is inviscid.

The surface velocity is given by Eq. (8.34). From Bernoulli's equation (8.4), neglecting gravity, the surface pressure p_s is given by

$$p_\infty + \frac{1}{2} \rho U_\infty^2 = p_s + \frac{1}{2} \rho \left(-2U_\infty \sin \theta + \frac{K}{a} \right)^2$$

$$\text{or} \quad p_s = p_\infty + \frac{1}{2} \rho U_\infty^2 (1 - 4 \sin^2 \theta + 4\beta \sin \theta - \beta^2) \quad (8.37)$$

where $\beta = K/(U_\infty a)$ and p_∞ is the free-stream pressure. If b is the cylinder depth into the paper, the drag D is the integral over the surface of the horizontal component of pressure force

$$D = - \int_0^{2\pi} (p_s - p_\infty) \cos \theta \, ba \, d\theta$$

where $p_s - p_\infty$ is substituted from Eq. (8.37). But the integral of $\cos \theta$ times any power of $\sin \theta$ over a full cycle 2π is identically zero. Thus we obtain the (perhaps surprising) result

$$D(\text{cylinder with circulation}) = 0 \quad (8.38)$$

This is a special case of d'Alembert's paradox, mentioned in Sec. 1.10:

According to inviscid theory, the drag of any body of any shape immersed in a uniform stream is identically zero.

D'Alembert published this result in 1752 and pointed out himself that it did not square with the facts for real fluid flows. This unfortunate paradox caused everyone to overreact and reject all inviscid theory until 1904, when Prandtl first pointed out the profound effect of the thin viscous boundary layer on the flow pattern in the rear, as in Fig. 7.2b, for example.

The lift force L normal to the stream, taken positive upward, is given by summation of vertical pressure forces

$$L = - \int_0^{2\pi} (p_s - p_\infty) \sin \theta \, ba \, d\theta$$

Since the integral over 2π of any odd power of $\sin \theta$ is zero, only the third term in the parentheses in Eq. (8.37) contributes to the lift:

$$L = - \frac{1}{2} \rho U_\infty^2 \frac{4K}{aU_\infty} \, ba \int_0^{2\pi} \sin^2 \theta \, d\theta = -\rho U_\infty (2\pi K) b$$

or
$$\frac{L}{b} = -\rho U_\infty \Gamma \quad (8.39)$$

Notice that the lift is independent of the radius a of the cylinder. Actually, though, as we shall see in Sec. 8.7, the circulation Γ depends upon the body size and orientation through a physical requirement.

Equation (8.39) was generalized by W. M. Kutta in 1902 and independently by N. Joukowski in 1906 as follows:

According to inviscid theory, the lift per unit depth of any cylinder of any shape immersed in a uniform stream equals $\rho u_\infty \Gamma$, where Γ is the total net circulation contained within the body shape. The direction of the lift is 90° from the stream direction, rotating opposite to the circulation.

The problem in airfoil analysis, Sec. 8.7, is thus to determine the circulation Γ as a function of airfoil shape and orientation.

Experimental Lift and Drag of Rotating Cylinders

It is nearly impossible to test Fig. 8.10 by constructing a doublet and vortex with the same center and then letting a stream flow past them. But one physical realization would be a rotating cylinder in a stream. The viscous no-slip condition would cause the fluid in contact with the cylinder to move tangentially at the cylinder peripheral speed $v_\theta = a\omega$. A net circulation Γ would be set up by this no-slip mechanism, but it turns out to be less than 50 percent of the value expected from inviscid theory, primarily because of flow separation behind the cylinder.

Figure 8.11 shows experimental lift and drag coefficients, based on planform area $2ba$, of rotating cylinders. From Eq. (8.38) the theoretical drag is zero, but the actual C_D is quite large, more even than the stationary cylinder of Fig. 5.3. The theoretical lift follows from Eq. (8.39)

$$C_L = \frac{L}{\frac{1}{2}\rho U_\infty^2(2ba)} = \frac{2\pi\rho U_\infty K b}{\rho U_\infty^2 b a} = \frac{2\pi v_{\theta s}}{U_\infty} \quad (8.40)$$

where $v_{\theta s} = K/a$ is the peripheral speed of the cylinder.

Figure 8.11 shows that the theoretical lift from Eq. (8.40) is much too high, but the measured lift is quite respectable, much larger in fact than a typical airfoil of the same chord length, e.g., Fig. 7.25. Thus rotating cylinders have practical possibilities. The Flettner rotor ship built in Germany in 1924 employed rotating vertical cylinders which developed a thrust due to any winds blowing past the ship. The Flettner design did not gain any popularity, but such inventions may be more attractive in this era of high energy costs.

EXAMPLE 8.2

The experimental Flettner rotor sailboat at the University of Rhode Island is shown in Fig. E8.2. The rotor is 2.5 ft in diameter and 10 ft long and rotates at 220 r/min. It is driven by a small lawnmower engine. If the wind is a steady 10 kn and boat relative motion is neglected, what is the maximum thrust expected for the rotor? Assume standard air and water density.

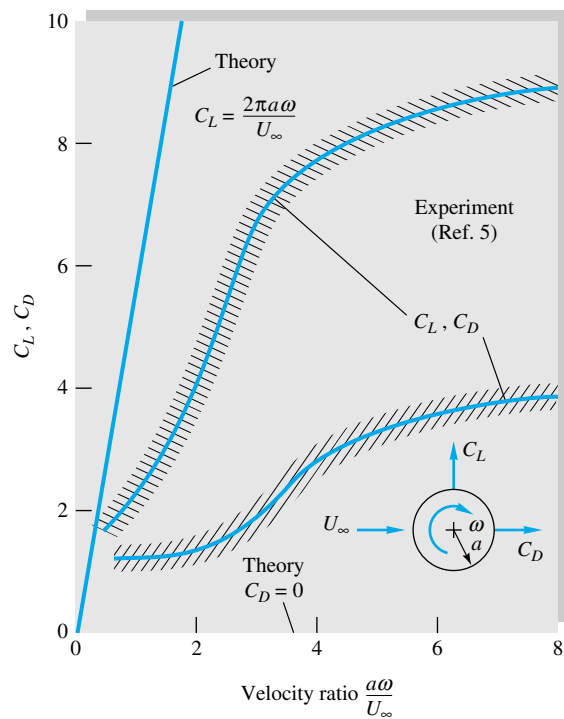


Fig. 8.11 Theoretical and experimental lift and drag of a rotating cylinder. (From Ref. 22.)



E8.2

(Courtesy of R. C. Lessmann, University of Rhode Island.)

Solution

Convert the rotation rate to $\omega = 2\pi(220)/60 = 23.04$ rad/s. The wind velocity is 10 kn = 16.88 ft/s, so the velocity ratio is

$$\frac{a\omega}{U_\infty} = \frac{(1.25 \text{ ft})(23.04 \text{ rad/s})}{16.88 \text{ ft/s}} = 1.71$$

Entering Fig. 8.11, we read $C_L \approx 3.3$ and $C_D \approx 1.2$. From Table A.6, standard air density is 0.002377 slug/ft³. Then the estimated rotor lift and drag are

$$\begin{aligned} L &= C_{L\frac{1}{2}} \rho U_\infty^2 2ba = 3.3\left(\frac{1}{2}\right)(0.002377)(16.88)^2(2)(10)(1.25) \\ &= 27.9 \text{ lbf} \end{aligned}$$

$$D = C_{D\frac{1}{2}} \rho U_\infty^2 2ba = L \frac{C_D}{C_L} = 27.9 \left(\frac{1.2}{3.3} \right) = 10.2 \text{ lbf}$$

The maximum thrust available is the resultant of these two

$$F = [(27.9)^2 + (10.2)^2]^{1/2} = 29 \text{ lbf} \quad \text{Ans.}$$

If aligned along the boat's keel, this thrust will drive the boat at a speed of about 5 kn through the water.

The Kelvin Oval

A family of body shapes taller than they are wide can be formed by letting a uniform stream flow normal to a vortex pair. If U_∞ is to the right, the negative vortex $-K$ is placed at $y = +a$ and the counterclockwise vortex $+K$ placed at $y = -a$, as in Fig. 8.12. The combined stream function is

$$\psi = U_\infty y - \frac{1}{2} K \ln \frac{x^2 + (y + a)^2}{x^2 + (y - a)^2} \quad (8.41)$$

The body shape is the line $\psi = 0$, and some of these shapes are shown in Fig. 8.12. For $K/(U_\infty a) > 10$ the shape is within 1 percent of a Rankine oval (Fig. 8.9) turned 90° , but for small $K/(U_\infty a)$ the waist becomes pinched in, and a figure-eight shape occurs at 0.5 . For $K/(U_\infty a) < 0.5$ the stream blasts right between the vortices and isolates two more or less circular body shapes, one surrounding each vortex.

A closed body of practically any shape can be constructed by proper superposition of sources, sinks, and vortices. See the advanced work in Refs. 2 to 4 for further details. A summary of elementary potential flows is given in Table 8.2.

Potential-Flow Analogs

For complicated potential-flow geometries, one can resort to other methods than superposition of sources, sinks, and vortices. There are a variety of devices which simulate solutions to Laplace's equation.

From 1897 to 1900 Hele-Shaw [9] developed a technique whereby laminar flow between very closely spaced parallel plates simulated potential flow when viewed from above the plates. Obstructions simulate body shapes, and dye streaks represent the streamlines. The Hele-Shaw apparatus makes an excellent laboratory demonstration of potential flow [10, pp. 8–10]. Figure 8.13a illustrates Hele-Shaw (potential) flow

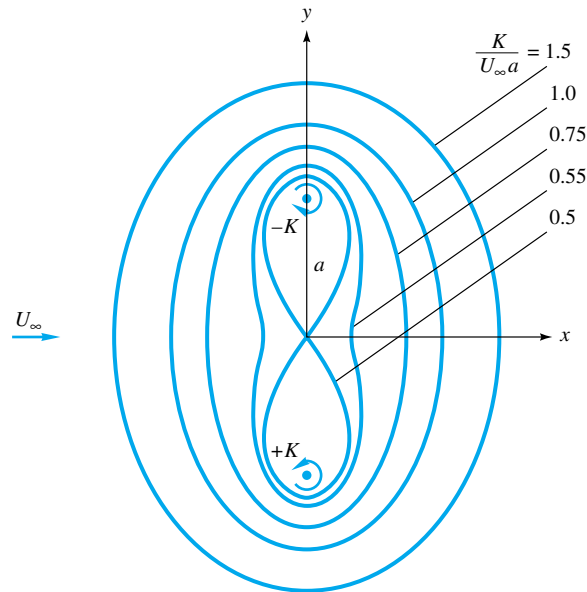


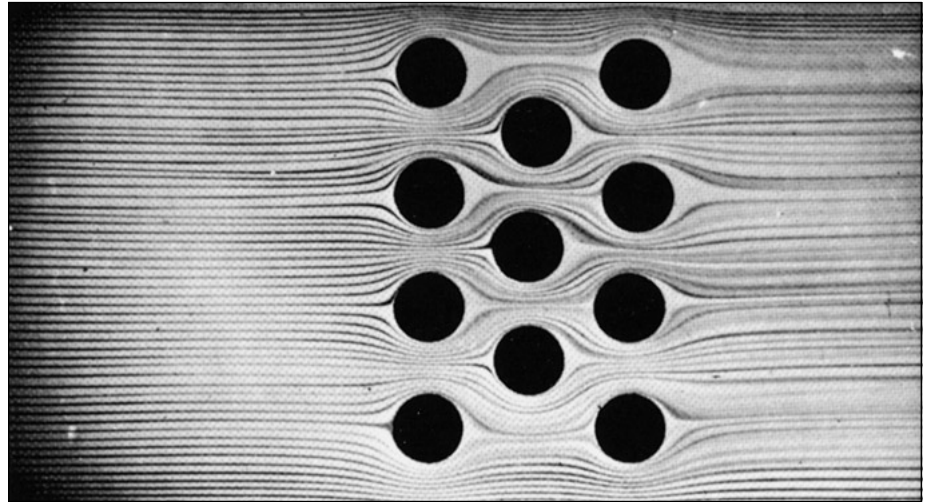
Fig. 8.12 Kelvin-oval body shapes as a function of the vortex-strength parameter $K/(U_\infty a)$; outer streamlines not shown.

through an array of cylinders, a flow pattern that would be difficult to analyze just using Laplace's equation. However beautiful this array pattern may be, it is not a good approximation to real (laminar viscous) array flow. Figure 8.13*b* shows experimental streakline patterns for a similar staggered-array flow at $Re \approx 6400$. We see that the interacting wakes of the real flow (Fig. 8.13*b*) cause intensive mixing and transverse motion, not the smooth streaming passage of the potential-flow model (Fig. 8.13*a*). The moral is that this is an internal flow with multiple bodies and, therefore, not a good candidate for a realistic potential-flow model.

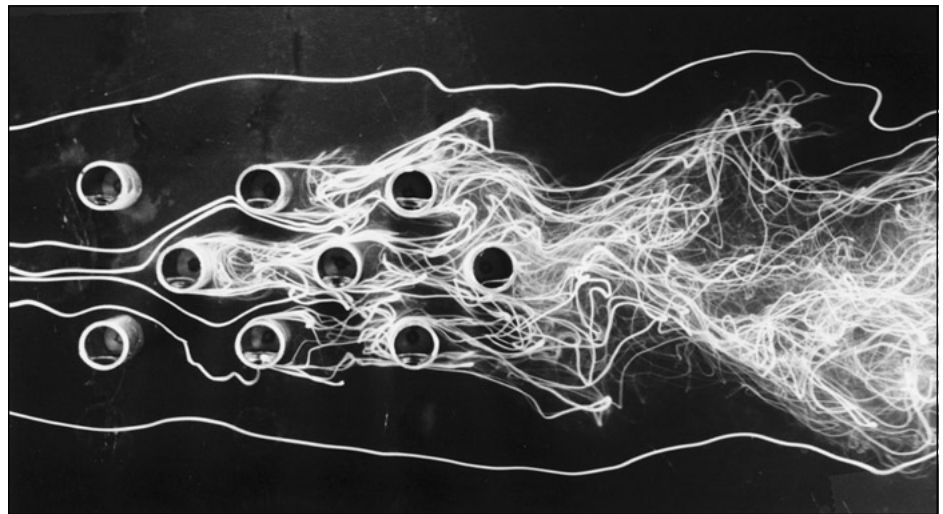
Other flow-mapping techniques are discussed in Ref. 8. Electromagnetic fields also satisfy Laplace's equation, with voltage analogous to velocity potential and current lines analogous to streamlines. At one time commercial analog field plotters were available, using thin conducting paper cut to the shape of the flow geometry. Potential lines (voltage contours) were plotted by probing the paper with a potentiometer pointer.

Table 8.2 Summary of Plane Incompressible Potential Flows

Type of flow	Potential functions	Remarks
Stream iU	$\psi = Uy$ $\phi = Ux$	See Fig. 4.12 <i>a</i>
Line source ($m > 0$) or sink ($m < 0$)	$\psi = m\theta$ $\phi = m \ln r$	See Fig. 4.12 <i>b</i>
Line vortex	$\psi = -K \ln r$ $\phi = K\theta$	See Fig. 4.12 <i>c</i>
Half-body	$\psi = Ur \sin \theta + m\theta$ $\phi = Ur \cos \theta + m \ln r$	See Fig. 8.5
Doublet	$\psi = \frac{-\lambda \sin \theta}{r}$ $\phi = \frac{\lambda \cos \theta}{r}$	See Fig. 8.8
Rankine oval	$\psi = Ur \sin \theta + m(\theta_1 - \theta_2)$	See Fig. 8.9
Cylinder with circulation	$\psi = U \sin \theta \left(r - \frac{a^2}{r} \right) - K \ln \frac{r}{a}$	See Fig. 8.10



(a)



(b)

Fig. 8.13 Flow past a staggered array of cylinders: (a) potential-flow model using the Hele-Shaw apparatus (Tecquipment Ltd., Nottingham, England); (b) experimental streaklines for actual staggered-array flow at $Re_D \approx 6400$. (From Ref. 36, courtesy of Jack Hoyt, with the permission of the American Society of Mechanical Engineers.)

Hand-sketching “curvilinear square” techniques were also popular. The availability and the simplicity of digital-computer potential-flow methods [5 to 7] have made analog models obsolete.

EXAMPLE 8.3

A Kelvin oval from Fig. 8.12 has $K/(U_\infty a) = 1.0$. Compute the velocity at the top shoulder of the oval in terms of U_∞ .

Solution

We must locate the shoulder $y = h$ from Eq. (8.41) for $\psi = 0$ and then compute the velocity by differentiation. At $\psi = 0$ and $y = h$ and $x = 0$, Eq. (8.41) becomes

$$\frac{h}{a} = \frac{K}{U_\infty a} \ln \frac{h/a + 1}{h/a - 1}$$

With $K/(U_\infty a) = 1.0$ and the initial guess $h/a \approx 1.5$ from Fig. 8.12, we iterate and find the location $h/a = 1.5434$.

By inspection $v = 0$ at the shoulder because the streamline is horizontal. Therefore the shoulder velocity is, from Eq. (8.41),

$$u \Big|_{y=h} = \frac{\partial \psi}{\partial y} \Big|_{y=h} = U_\infty + \frac{K}{h-a} - \frac{K}{h+a}$$

Introducing $K = U_\infty a$ and $h = 1.5434a$, we obtain

$$u_{\text{shoulder}} = U_\infty(1.0 + 1.84 - 0.39) = 2.45U_\infty \quad \text{Ans.}$$

Because they are short-waisted compared with a circular cylinder, all the Kelvin ovals have shoulder velocity greater than the cylinder result $2.0U_\infty$ from Eq. (8.34).

8.5 Other Plane Potential Flows²

References 2 to 4 treat many other potential flows of interest in addition to the cases presented in Secs. 8.3 and 8.4. In principle, any plane potential flow can be solved by the method of *conformal mapping*, by using the complex variable

$$z = x + iy \quad i = (-1)^{1/2}$$

It turns out that any arbitrary analytic function of this complex variable z has the remarkable property that both its real and its imaginary parts are solutions of Laplace's equation. If

$$f(z) = f(x + iy) = f_1(x, y) + i f_2(x, y)$$

then

$$\frac{\partial^2 f_1}{\partial x^2} + \frac{\partial^2 f_1}{\partial y^2} = 0 = \frac{\partial^2 f_2}{\partial x^2} + \frac{\partial^2 f_2}{\partial y^2} \quad (8.42)$$

We shall assign the proof of this as a problem. Even more remarkable if you have never seen it before is that lines of constant f_1 will be everywhere perpendicular to lines of constant f_2 :

$$\left(\frac{dy}{dx} \right)_{f_1=C} = - \frac{1}{(dy/dx)_{f_2=C}} \quad (8.43)$$

We also leave this proof as a problem exercise. This is true for totally arbitrary $f(z)$ as long as this function is analytic; i.e., it must have a unique derivative df/dz at every point in the region.

The net result of Eqs. (8.42) and (8.43) is that the functions f_1 and f_2 can be interpreted to be the potential lines and streamlines of an inviscid flow. By long custom we

² This section may be omitted without loss of continuity.

let the real part of $f(z)$ be the velocity potential and the imaginary part be the stream function

$$f(z) = \phi(x, y) + i\psi(x, y) \quad (8.44)$$

We try various functions $f(z)$ and see whether any interesting flow pattern results. Of course, most of them have already been found, and we simply report on them here.

We shall not go into the details, but there are excellent treatments of this complex-variable technique on both an introductory [4, chap. 5; 10, chap. 5] and a more advanced [2, 3,] level. The method is less important now because of the popularity of digital-computer techniques.

As a simple example, consider the linear function

$$f(z) = U_\infty z = U_\infty x + iU_\infty y$$

It follows from Eq. (8.44) that $\phi = U_\infty x$ and $\psi = U_\infty y$, which, we recall from Eq. (8.12a), represents a uniform stream in the x direction. Once you get used to the complex variable, the solution practically falls in your lap.

To find the velocities, you may either separate ϕ and ψ from $f(z)$ and differentiate or differentiate f directly

$$\frac{df}{dz} = \frac{\partial\phi}{\partial x} + i\frac{\partial\psi}{\partial x} = -i\frac{\partial\phi}{\partial y} + \frac{\partial\psi}{\partial y} = u - iv \quad (8.45)$$

Thus the real part of df/dz equals $u(x, y)$, and the imaginary part equals $-v(x, y)$. To get a practical result, the derivative df/dz must exist and be unique, hence the requirement that f be an analytic function. For Eq. (8.45), $df/dz = U_\infty = u$, since it is real, and $v = 0$, as expected.

Sometimes it is convenient to use the polar-coordinate form of the complex variable

$$z = x + iy = re^{i\theta} = r \cos \theta + ir \sin \theta$$

where
$$r = (x^2 + y^2)^{1/2} \quad \theta = \tan^{-1} \frac{y}{x}$$

This form is especially convenient when powers of z occur.

Uniform Stream at an Angle of Attack

All the elementary plane flows of Sec. 8.2 have a complex-variable formulation. The uniform stream U_∞ at an angle of attack α has the complex potential

$$f(z) = U_\infty z e^{-i\alpha} \quad (8.46)$$

Compare this form with Eq. (8.14).

Line Source at a Point z_0

Consider a line source of strength m placed off the origin at a point $z_0 = x_0 + iy_0$. Its complex potential is

$$f(z) = m \ln(z - z_0) \quad (8.47)$$

This can be compared with Eq. (8.12b), which is valid only for the source at the origin. For a line sink, the strength m is negative.

Line Vortex at a Point z_0

If a line vortex of strength K is placed at point z_0 , its complex potential is

$$f(z) = -iK \ln(z - z_0) \quad (8.48)$$

to be compared with Eq. (8.12c). Also compare to Eq. (8.47) to see that we reverse the meaning of ϕ and ψ simply by multiplying the complex potential by $-i$.

Flow around a Corner of Arbitrary Angle

Corner flow is an example of a pattern that cannot be conveniently produced by superimposing sources, sinks, and vortices. It has a strikingly simple complex representation

$$f(z) = Az^n = Ar^n e^{in\theta} = Ar^n \cos n\theta + iAr^n \sin n\theta$$

where A and n are constants.

It follows from Eq. (8.44) that for this pattern

$$\phi = Ar^n \cos n\theta \quad \psi = Ar^n \sin n\theta \quad (8.49)$$

Streamlines from Eq. (8.49) are plotted in Fig. 8.14 for five different values of n . The flow is seen to represent a stream turning through an angle $\beta = \pi/n$. Patterns in Fig. 8.14d and e are not realistic on the downstream side of the corner, where separation will occur due to the adverse pressure gradient and sudden change of direction. In general, separation always occurs downstream of salient, or protruding corners, except in creeping flows at low Reynolds number $Re < 1$.

Since $360^\circ = 2\pi$ is the largest possible corner, the patterns for $n < \frac{1}{2}$ do not represent corner flow. They are peculiar-looking, and we ask you to plot one as a problem.

If we expand the plot of Fig. 8.14a to c to double size, we can represent stagnation flow toward a corner of angle $2\beta = 2\pi/n$. This is done in Fig. 8.15 for $n = 3, 2$, and

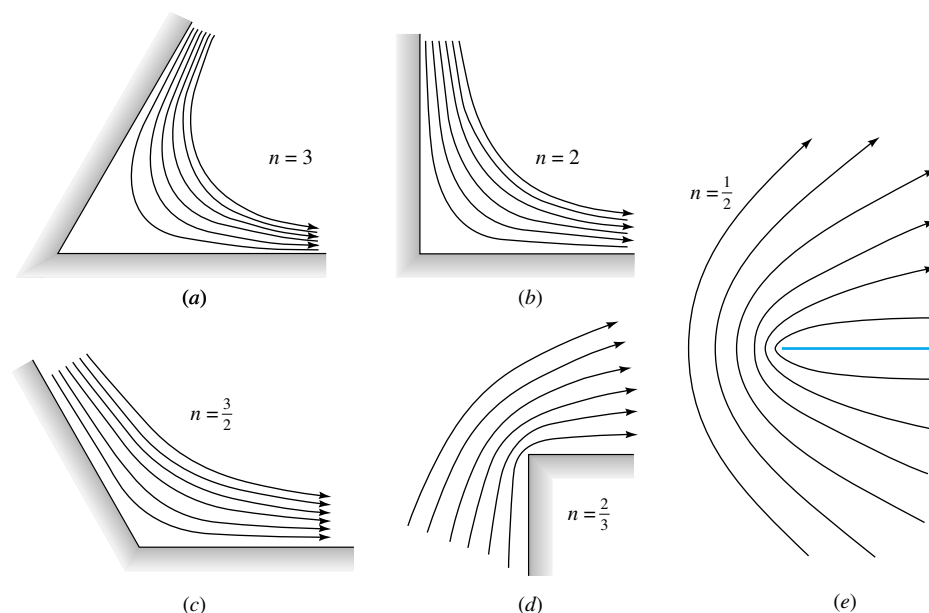


Fig. 8.14 Streamlines for corner flow, Eq. (8.49) for corner angle β of (a) 60° , (b) 90° , (c) 120° , (d) 270° , and (e) 360° .

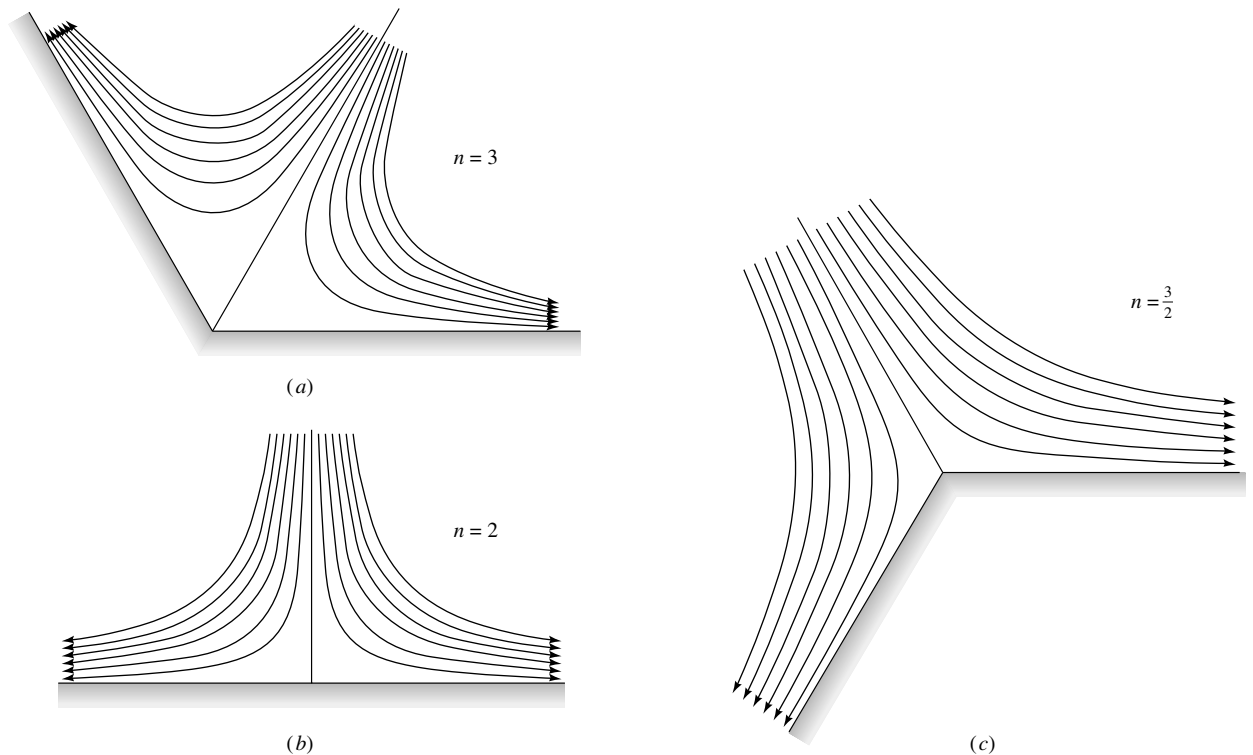


Fig. 8.15 Streamlines for stagnation flow from Eq. (8.49) for corner angle 2β of (a) 120° , (b) 180° , and (c) 240° .

1.5. These are very realistic flows; although they slip at the wall, they can be patched to boundary-layer theories very successfully. We took a brief look at corner flows before, in Examples 4.5 and 4.9 and in Probs. 4.49 to 4.51.

Flow Normal to a Flat Plate

We treat this case separately because the Kelvin ovals of Fig. 8.12 failed to degenerate into a flat plate as K became small. The flat plate normal to a uniform stream is an extreme case worthy of our attention.

Although the result is quite simple, the derivation is very complicated and is given, e.g., in Ref. 2, sec. 9.3. There are three changes of complex variable, or *mappings*, beginning with the basic cylinder-flow solution of Fig. 8.10a. First the uniform stream is rotated to be vertical upward, then the cylinder is squeezed down into a plate shape, and finally the free stream is rotated back to the horizontal. The final result for complex potential is

$$f(z) = \phi + i\psi = U_\infty(z^2 + a^2)^{1/2} \quad (8.50)$$

where $2a$ is the height of the plate. To isolate ϕ or ψ , square both sides and separate real and imaginary parts

$$\phi^2 - \psi^2 = U_\infty^2(x^2 - y^2 + a^2) \quad \phi\psi = U_\infty^2xy$$

We can solve for ψ to determine the streamlines

$$\psi^4 + \psi^2 U_\infty^2 (x^2 - y^2 + a^2) = U_\infty^4 x^2 y^2 \quad (8.51)$$

Equation (8.51) is plotted in Fig. 8.16a, revealing a doubly symmetric pattern of streamlines which approach very closely to the plate and then deflect up and over, with very high velocities and low pressures near the plate tips.

The velocity v_s along the plate surface is found by computing $d\psi/dz$ from Eq. (8.50) and isolating the imaginary part

$$\frac{v_s}{U_\infty} \Big|_{\text{plate surface}} = \frac{y/a}{(1 - y^2/a^2)^{1/2}} \quad (8.52)$$

Some values of surface velocity can be tabulated as follows:

y/a	0.0	0.2	0.4	0.6	0.71	0.8	0.9	1.0
v_s/U_∞	0.0	0.204	0.436	0.750	1.00	1.33	2.07	∞

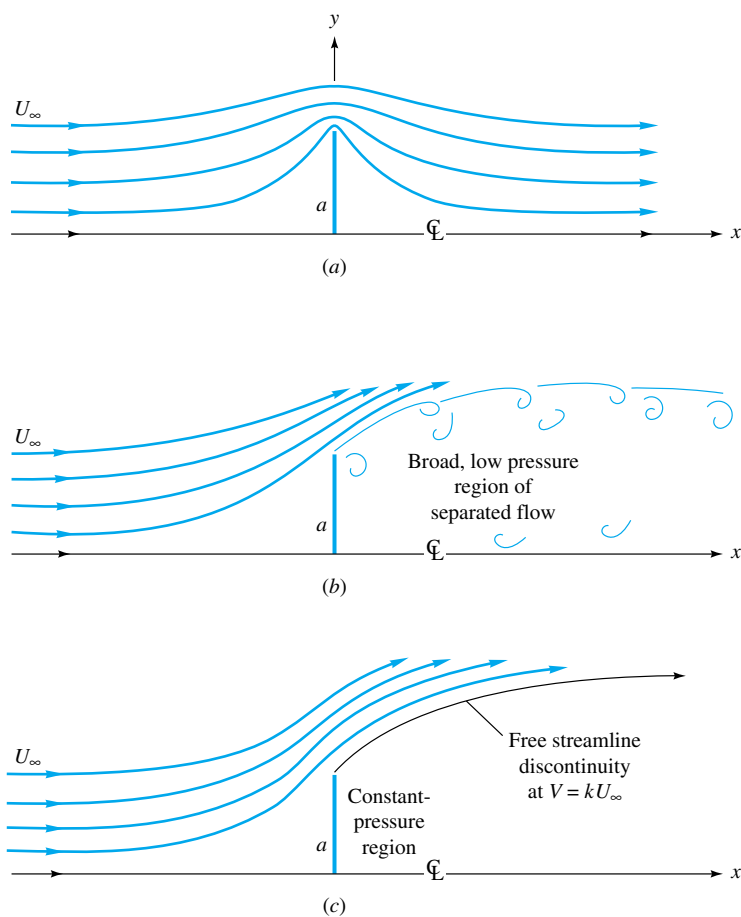


Fig. 8.16 Streamlines in upper half-plane for flow normal to a flat plate of height $2a$: (a) continuous potential-flow theory, Eq. (8.51); (b) actual measured flow pattern; (c) discontinuous potential theory with $k \approx 1.5$.

The origin is a stagnation point; then the velocity grows linearly at first and very rapidly near the tip, with both velocity and acceleration being infinite at the tip.

As you might guess, Fig. 8.16a is not realistic. In a real flow the sharp salient edge causes separation, and a broad, low-pressure wake forms in the lee, as in Fig. 8.16b. Instead of being zero, the drag coefficient is very large, $C_D \approx 2.0$ from Table 7.2.

A discontinuous-potential-flow theory which accounts for flow separation was devised by Helmholtz in 1868 and Kirchhoff in 1869. This free-streamline solution is shown in Fig. 8.16c, with the streamline which breaks away from the tip having a constant velocity $V = kU_\infty$. From Bernoulli's equation the pressure in the dead-water region behind the plate will equal $p_r = p_\infty + \frac{1}{2}\rho U_\infty^2(1 - k^2)$ to match the pressure along the free streamline. For $k = 1.5$ this Helmholtz-Kirchhoff theory predicts $p_r = p_\infty - 0.625\rho U_\infty^2$ and an average pressure on the front $p_f = p_\infty + 0.375\rho U_\infty^2$, giving an overall drag coefficient of 2.0, in agreement with experiment. However, the coefficient k is a priori unknown and must be tuned to experimental data, so free-streamline theory can be considered only a qualified success. For further details see Ref. 2, sec. 11.2.

8.6 Images³

The previous solutions have all been for unbounded flows, such as a circular cylinder immersed in a broad expanse of uniformly streaming fluid, Fig. 8.10a. However, many practical problems involve a nearby rigid boundary constraining the flow, e.g., (1) groundwater flow near the bottom of a dam, (2) an airfoil near the ground, simulating landing or takeoff, or (3) a cylinder mounted in a wind tunnel with narrow walls. In such cases the basic unbounded-potential-flow solutions can be modified for wall effects by the method of *images*.

Consider a line source placed a distance a from a wall, as in Fig. 8.17a. To create the desired wall, an image source of identical strength is placed the same distance below the wall. By symmetry the two sources create a plane-surface streamline between them, which is taken to be the wall.

In Fig. 8.17b a vortex near a wall requires an image vortex the same distance below but of *opposite* rotation. We have shaded in the wall, but of course the pattern could also be interpreted as the flow near a vortex pair in an unbounded fluid.

In Fig. 8.17c an airfoil in a uniform stream near the ground is created by an image airfoil below the ground of opposite circulation and lift. This looks easy, but actually it is not because the airfoils are so close together that they interact and distort each other's shapes. A rule of thumb is that nonnegligible shape distortion occurs if the body shape is within two chord lengths of the wall. To eliminate distortion, a whole series of "corrective" images must be added to the flow to recapture the shape of the original isolated airfoil. Reference 2, sec. 7.75, has a good discussion of this procedure, which usually requires digital-computer summation of the multiple images needed.

Figure 8.17d shows a source constrained between two walls. One wall required only one image in Fig. 8.17a, but *two* walls require an infinite array of image sources above and below the desired pattern, as shown. Usually computer summation is necessary, but sometimes a closed-form summation can be achieved, as in the infinite vortex row of Eq. (8.22).

³ This section may be omitted without loss of continuity.

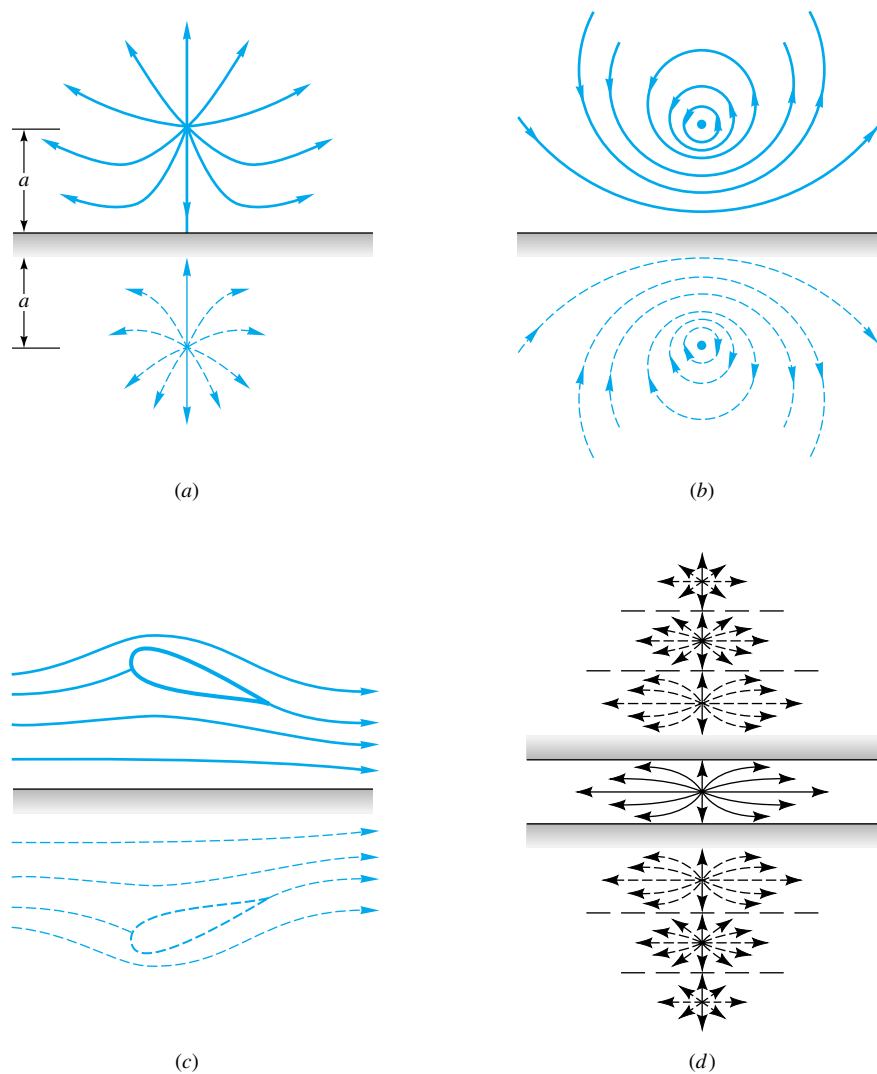


Fig. 8.17 Constraining walls can be created by image flows: (a) source near a wall with identical image source; (b) vortex near a wall with image vortex of opposite sense; (c) airfoil in ground effect with image airfoil of opposite circulation; (d) source between two walls requiring an infinite row of images.

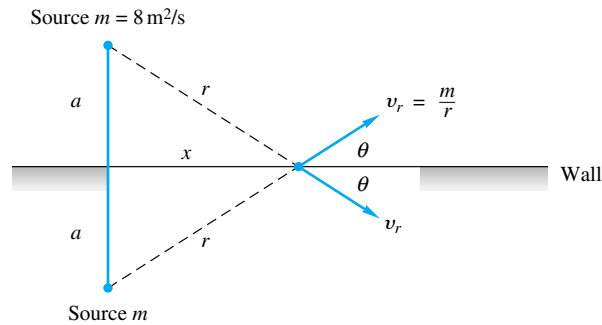
EXAMPLE 8.4

For the source near a wall as in Fig. 8.17a, the wall velocity is zero between the sources, rises to a maximum moving out along the wall, and then drops to zero far from the sources. If the source strength is $8 \text{ m}^2/\text{s}$, how far from the wall should the source be to ensure that the maximum velocity along the wall will be 5 m/s ?

Solution

At any point x along the wall, as in Fig. E8.4, each source induces a radial outward velocity $v_r = m/r$, which has a component $v_r \cos \theta$ along the wall. The total wall velocity is thus

E8.4



$$u_{\text{wall}} = 2v_r \cos \theta$$

From the geometry of Fig. E8.4, $r = (x^2 + a^2)^{1/2}$ and $\cos \theta = x/r$. Then the total wall velocity can be expressed as

$$u = \frac{2mx}{x^2 + a^2}$$

This is zero at $x = 0$ and at $x \rightarrow \infty$. To find the maximum velocity, differentiate and set equal to zero

$$\frac{du}{dx} = 0 \quad \text{at} \quad x = a \quad \text{and} \quad u_{\text{max}} = \frac{m}{a}$$

We have omitted a bit of algebra in giving these results. For the given source strength and maximum velocity, the proper distance a is

$$a = \frac{m}{u_{\text{max}}} = \frac{8 \text{ m}^2/\text{s}}{5 \text{ m/s}} = 1.625 \text{ m} \quad \text{Ans.}$$

For $x > a$, there is an adverse pressure gradient along the wall, and boundary-layer theory should be used to predict separation.

8.7 Airfoil Theory⁴

As mentioned in conjunction with the Kutta-Joukowski lift theorem, Eq. (8.39), the problem in airfoil theory is to determine the net circulation Γ as a function of airfoil shape and free-stream angle of attack α .

The Kutta Condition

Even if the airfoil shape and free-stream angle of attack are specified, the potential-flow-theory solution is nonunique: An infinite family of solutions can be found corresponding to different values of circulation Γ . Four examples of this nonuniqueness were shown for the cylinder flows in Fig. 8.10. The same is true of the airfoil, and Fig. 8.18 shows three mathematically acceptable “solutions” to a given airfoil flow for small (Fig. 8.18a), large (Fig. 8.18b), and medium (Fig. 8.18c) net circulation. You can guess

⁴ This section may be omitted without loss of continuity.

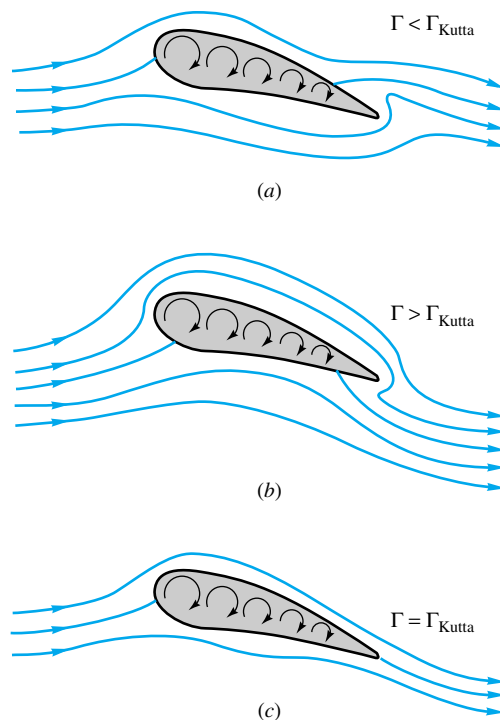


Fig. 8.18 The Kutta condition properly simulates the flow about an airfoil; (a) too little circulation, stagnation point on rear upper surface; (b) too much, stagnation point on rear lower surface; (c) just right, Kutta condition requires smooth flow at trailing edge.

which case best simulates a real airfoil from the earlier discussion of transient-lift development in Fig. 7.23. It is the case (Fig. 8.18c) where the upper and lower flows meet and leave the trailing edge smoothly. If the trailing edge is rounded slightly, there will be a stagnation point there. If the trailing edge is sharp, approximating most airfoil designs, the upper- and lower-surface flow velocities will be equal as they meet and leave the airfoil.

This statement of the physically proper value of Γ is generally attributed to W. M. Kutta, hence the name *Kutta condition*, although some texts give credit to Joukowski and/or Chaplygin. All airfoil theories use the Kutta condition, which is in good agreement with experiment. It turns out that the correct circulation Γ_{Kutta} depends upon flow velocity, angle of attack, and airfoil shape.

Flat-Plate Airfoil Vortex-Sheet Theory

The flat plate is the simplest airfoil, having no thickness or “shape,” but even its theory is not so simple. The problem can be solved by a complex-variable mapping [2, p. 480], but here we shall use a vortex-sheet approach. Figure 8.19a shows a flat plate of length C simulated by a vortex sheet of variable strength $\gamma(x)$. The free stream U_∞ is at an angle of attack α with respect to the plate chord line.

To make the lift “up” with flow from left to right as shown, we specify here that the circulation is positive clockwise. Recall from Fig. 8.7c that there is a jump in tangential velocity across a sheet equal to the local strength

$$u_u - u_l = \gamma(x) \quad (8.53)$$

If we omit the free stream, the sheet should cause a rightward flow $\delta u = +\frac{1}{2}\gamma$ on the upper surface and an equal and opposite leftward flow on the lower surface, as shown in Fig. 8.19a. The Kutta condition for this sharp trailing edge requires that this velocity difference vanish at the trailing edge to keep the exit flow smooth and parallel

$$\gamma(C) = 0 \quad (8.54)$$

The proper solution must satisfy this condition, after which the total lift can be computed by summing the sheet strength over the whole airfoil. From Eq. (8.39) for a foil of depth b

$$L = \rho U_\infty b \Gamma \quad \Gamma = \int_0^C \gamma(x) dx \quad (8.55)$$

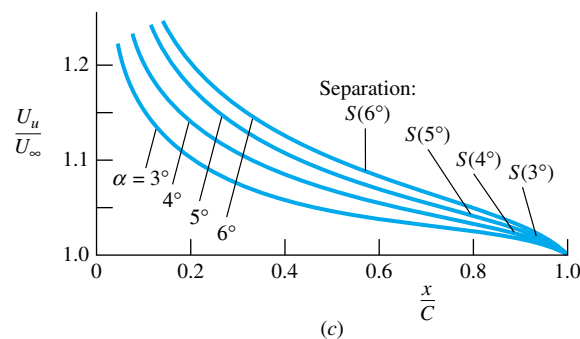
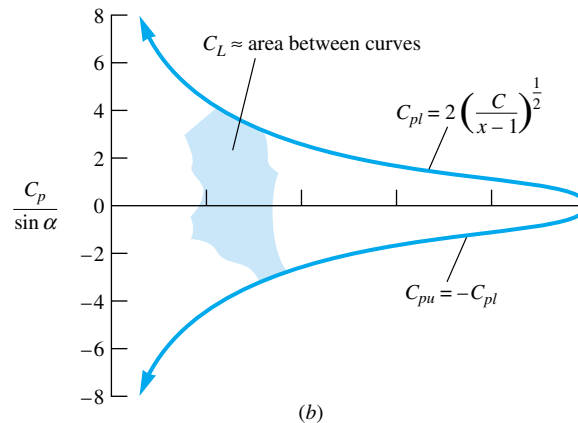
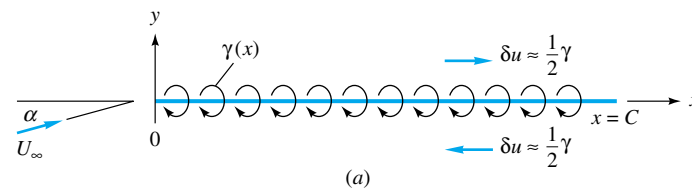


Fig. 8.19 Vortex-sheet solution for the flat-plate airfoil; (a) sheet geometry; (b) theoretical pressure coefficient on upper and lower surfaces; (c) upper-surface velocity with laminar separation points S .

An alternate way to compute lift is from the dimensionless pressure coefficient C_p on the upper and lower surfaces

$$C_{p_{u,l}} = \frac{p_{u,l} - p_\infty}{\frac{1}{2}\rho U_\infty^2} = 1 - \frac{U_{u,l}^2}{U_\infty^2} \quad (8.56)$$

where the last expression follows from Bernoulli's equation. The surface velocity squared is given by combining the uniform stream and the vortex-sheet velocity components from Fig. 8.19a:

$$\begin{aligned} U_{u,l}^2 &= (U_\infty \cos \alpha \pm \delta u)^2 + (U_\infty \sin \alpha)^2 \\ &= U_\infty^2 \pm 2U_\infty \delta u \cos \alpha + \delta u^2 \approx U_\infty^2 \left(1 \pm \frac{2\delta u}{U_\infty}\right) \end{aligned} \quad (8.57)$$

where we have made the approximations $\delta u \ll U_\infty$ and \cos in the last expression, assuming a small angle of attack. Equations (8.56) and (8.57) combine to the first-order approximation

$$C_{p_{u,l}} = \mp \frac{2\delta u}{U_\infty} = \mp \frac{\gamma}{U_\infty} \quad (8.58)$$

The lift force is the integral of the pressure difference over the length of the airfoil, assuming depth b

$$L = \int_0^C (p_l - p_u) b \, dx$$

or

$$C_L = \frac{L}{\frac{1}{2}\rho U_\infty^2 b C} = \int_0^1 (C_{p_l} - C_{p_u}) \frac{dx}{C} = 2 \int_0^1 \frac{\gamma}{U_\infty} d\left(\frac{x}{C}\right) \quad (8.59)$$

Equations (8.55) and (8.59) are entirely equivalent within the small-angle approximations.

The sheet strength $\gamma(x)$ is computed from the requirement that the net normal velocity $v(x)$ be zero at the sheet ($y = 0$), since the sheet represents a solid plate or stream surface. Consider a small piece of sheet $\gamma \, dx$ located at position x_0 . The velocity v at point x on the sheet is that of an infinitesimal line vortex of strength $d\Gamma = -\gamma \, dx$

$$dv \Big|_x = \frac{d\Gamma}{2\pi r|_{x_0 \rightarrow x}} = \frac{-\gamma \, dx}{2\pi(x_0 - x)}$$

The total normal velocity induced by the entire sheet at point x is thus

$$v_{\text{sheet}} = - \int_0^C \frac{-\gamma \, dx}{2\pi(x_0 - x)} \quad (8.60)$$

Meanwhile, from Fig. 8.19a, the uniform stream induces a constant normal velocity at every point on the sheet given by

$$v_{\text{stream}} = U_\infty \sin \alpha$$

Setting the sum of v_{sheet} and v_{stream} equal to zero gives the integral equation

$$\int_0^C \frac{\gamma \, dx}{x_0 - x} = 2\pi U_\infty \sin \alpha \quad (8.61)$$

to be solved for $\gamma(x)$ subject to the Kutta condition $\gamma(C) = 0$ from Eq. (8.54).

Although Eq. (8.61) is quite formidable (and not only for beginners), in fact it was solved long ago by using integral formulas developed by Poisson in the nineteenth century. The sheet strength which satisfies Eq. (8.61) is

$$\gamma(x) = 2U_\infty \sin \alpha \left(\frac{C}{x} - 1 \right)^{1/2} \quad (8.62)$$

From Eq. (8.58) the surface-pressure coefficients are thus

$$C_{p_{u,l}} = \mp 2 \sin \alpha \left(\frac{C}{x} - 1 \right)^{1/2} \quad (8.63)$$

Details of the calculations are given in advanced texts [for example, 11, chap. 5].

The pressure coefficients from Eq. (8.63) are plotted in Fig. 8.19*b*, showing that the upper surface has pressure continually increasing with x , that is, an adverse gradient. The upper-surface velocity $U_u \approx U_\infty + \delta u = U_\infty + \frac{1}{2}\gamma$ is plotted in Fig. 8.19*c* for various angles of attack. Above $\alpha = 5^\circ$ the sheet contribution δu is about 20 percent of U_∞ so that the small-disturbance assumption is violated. Figure 8.19*c* also shows separation points computed by Thwaites' laminar-boundary-layer method, Eqs. (7.54) and (7.55). The prediction is that a flat plate would be extensively stalled on the upper surface for $\alpha > 6^\circ$, which is approximately correct.

The lift coefficient of the airfoil is proportional to the area between c_{p_l} and c_{p_u} in Fig. 8.19*b*, from Eq. (8.59):

$$C_L = 2 \int_0^1 \frac{\gamma}{U} d\left(\frac{x}{C}\right) = 4 \sin \alpha \int_0^1 \left(\frac{C}{x} - 1\right)^{1/2} d\left(\frac{x}{C}\right) = 2\pi \sin \alpha \approx 2\pi\alpha \quad (8.64)$$

This is a classic result which was alluded to earlier in Eq. (7.70) without proof.

Also of interest is the moment coefficient about the leading edge (LE) of the airfoil, taken as positive counterclockwise

$$C_{M_{LE}} = \frac{M_{LE}}{\frac{1}{2}\rho U_\infty^2 b C^2} = \int_0^1 (C_{p_l} - C_{p_u}) \frac{x}{C} d\left(\frac{x}{C}\right) = \frac{\pi}{2} \sin \alpha = \frac{1}{4} C_L \quad (8.65)$$

Thus the *center of pressure* (CP), or position of the resultant lift force, is at the one-quarter-chord point

$$\left(\frac{x}{C}\right)_{CP} = \frac{1}{4} \quad (8.66)$$

This theoretical result is independent of the angle of attack.

These results can be compared with experimental results for NACA airfoils in Fig. 8.20). The thinnest NACA airfoil is $t/C = 0.06$, and the thickest is 24 percent, or $t/C = 0.24$. The lift-curve slope $dC_L/d\alpha$ is within 9 percent of the theoretical value of 2π for all the various airfoil families at all thicknesses. Increasing thickness tends to increase both $C_{L,max}$ and the stall angle. The stall angle at $t/C = 0.06$ is about 8° and would be even less for a flat plate, verifying the boundary-layer separation estimates in Fig. 8.19*c*. Best performance is usually at about the 12 percent thickness point for any airfoil.

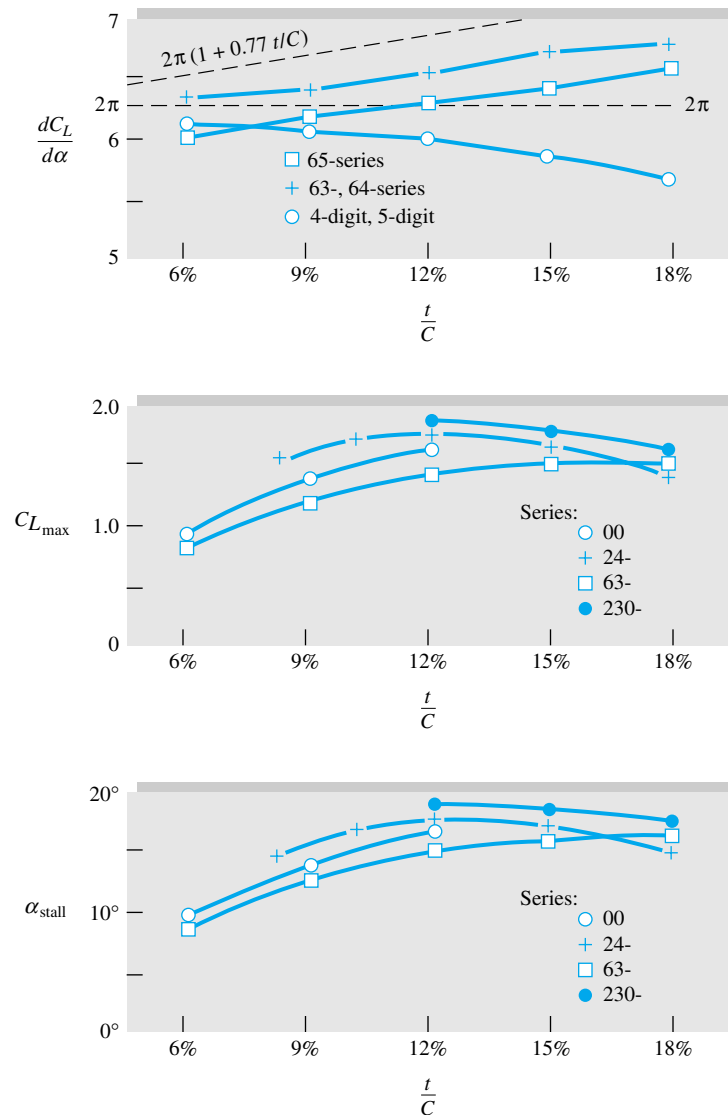


Fig. 8.20 Lift characteristics of smooth NACA airfoils as a function of thickness ratio, for infinite aspect ratio. (From Ref. 12.)

Potential Theory for Thick Cambered Airfoils

The theory of thick cambered airfoils is covered in advanced texts [for example, 2 to 4]; Ref. 13 has a thorough and comprehensive review of both inviscid and viscous aspects of airfoil behavior.

Basically the theory uses a complex-variable mapping which transforms the flow about a cylinder with circulation in Fig. 8.10 into flow about a foil shape with circulation. The circulation is then adjusted to match the Kutta condition of smooth exit flow from the trailing edge.

Regardless of the exact airfoil shape, the inviscid mapping theory predicts that the correct circulation for any thick cambered airfoil is

$$\Gamma_{\text{Kutta}} = \pi b C U_{\infty} \left(1 + 0.77 \frac{t}{C} \right) \sin(\alpha + \beta) \quad (8.67)$$

where $\beta = \tan^{-1}(2h/C)$ and h is the maximum camber, or maximum deviation of the airfoil midline from its chord line, as in Fig. 8.21a.

The lift coefficient of the infinite-span airfoil is thus

$$C_L = \frac{\rho U_{\infty} \Gamma}{\frac{1}{2} \rho U_{\infty}^2 b C} = 2\pi \left(1 + 0.77 \frac{t}{C} \right) \sin(\alpha + \beta) \quad (8.68)$$

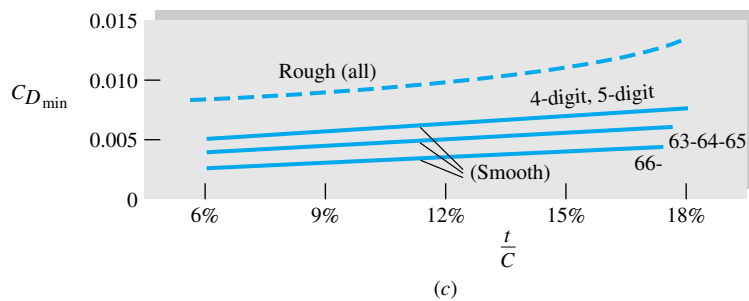
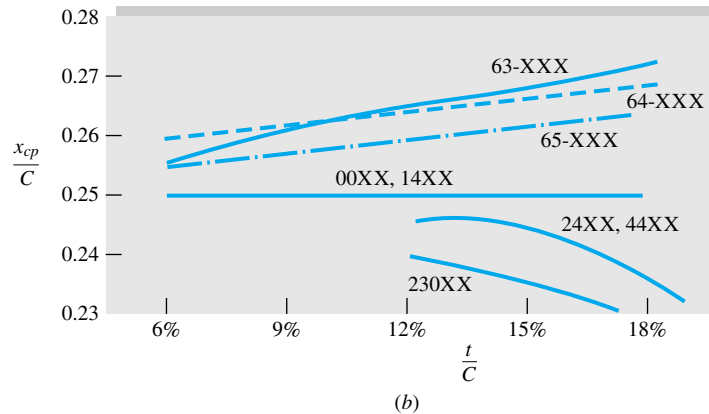
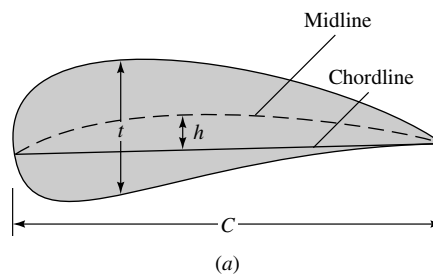


Fig. 8.21 Characteristics of NACA airfoils: (a) typical thick cambered airfoil; (b) center-of-pressure data; and (c) minimum drag coefficient.

This reduces to Eq. (8.64) when the thickness and camber are zero. Figure 8.20 shows that the thickness effect $1 + 0.77t/C$ is not verified by experiment. Some airfoils increase lift with thickness, others decrease, and none approach the theory very closely, the primary reason being the boundary-layer growth on the upper surface affecting the airfoil “shape.” Thus it is customary to drop the thickness effect from the theory

$$C_L \approx 2\pi \sin(\alpha + \beta) \quad (8.69)$$

The theory correctly predicts that a cambered airfoil will have finite lift at zero angle of attack and zero lift (ZL) at an angle

$$\alpha_{ZL} = -\beta = -\tan^{-1} \frac{2h}{C} \quad (8.70)$$

Equation (8.70) overpredicts the measured zero-lift angle by 1° or so, as shown in Table 8.3. The measured values are essentially independent of thickness. The designation XX in the NACA series indicates the thickness in percent, and the other digits refer to camber and other details. For example, the 2415 airfoil has 2 percent maximum camber (the first digit) occurring at 40 percent chord (the second digit) with 15 percent maximum thickness (the last two digits). The maximum thickness need not occur at the same position as the maximum camber.

Figure 8.21b shows the measured position of the center of pressure of the various NACA airfoils, both symmetric and cambered. In all cases x_{CP} is within 0.02 chord length of the theoretical quarter-chord point predicted by Eq. (8.66). The standard cambered airfoils (24, 44, and 230 series) lie slightly forward of $x/C = 0.25$ and the low-drag (60 series) foils slightly aft. The symmetric airfoils are at 0.25.

Figure 8.21c shows the minimum drag coefficient of NACA airfoils as a function of thickness. As mentioned earlier in conjunction with Fig. 7.25, these foils when smooth actually have less drag than turbulent flow parallel to a flat plate, especially the low-drag 60 series. However, for standard surface roughness all foils have about the same minimum drag, roughly 30 percent greater than that for a smooth flat plate.

Wings of Finite Span

The results of airfoil theory and experiment in the previous subsection were for two-dimensional, or infinite-span, wings. But all real wings have tips and are therefore of finite span or finite aspect ratio AR, defined by

$$AR = \frac{b^2}{A_p} = \frac{b}{C} \quad (8.71)$$

Table 8.3 Zero-Lift Angle of NACA Airfoils

Airfoil series	Camber h/C , %	Measured α_{ZL} , deg	Theory $-\beta$, deg
24XX	2.0	-2.1	-2.3
44XX	4.0	-4.0	-4.6
230XX	1.8	-1.3	-2.1
63-2XX	2.2	-1.8	-2.5
63-4XX	4.4	-3.1	-5.0
64-1XX	1.1	-0.8	-1.2

where b is the span length from tip to tip and A_p is the planform area of the wing as seen from above. The lift and drag coefficients of a finite-aspect-ratio wing depend strongly upon the aspect ratio and slightly upon the planform shape of the wing.

Vortices cannot end in a fluid; they must either extend to the boundary or form a closed loop. Figure 8.22*a* shows how the vortices which provide the wing circulation bend downstream at finite wing tips and extend far behind the wing to join the starting vortex (Fig. 7.23) downstream. The strongest vortices are shed from the tips, but

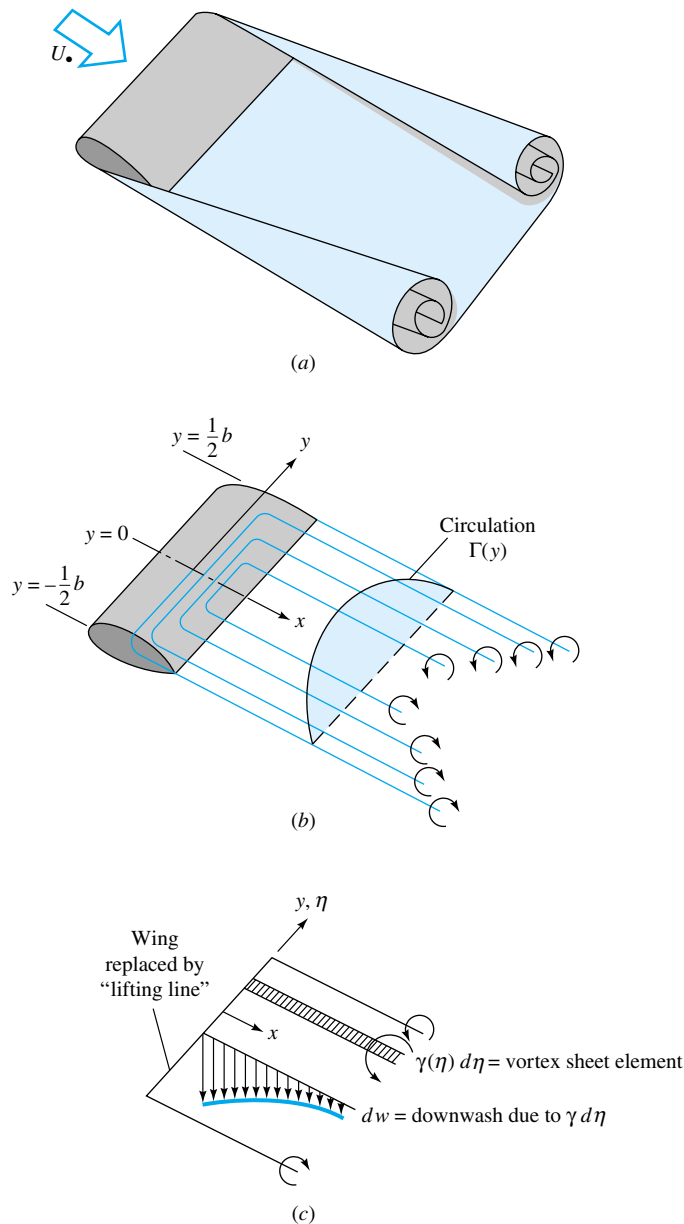


Fig. 8.22 Lifting-line theory for a finite wing: (a) actual trailing-vortex system behind a wing; (b) simulation by vortex system "bound" to the wing; (c) downwash on the wing due to an element of the trailing-vortex system.

some are shed from the body of the wing, as sketched schematically in Fig. 8.22*b*. The effective circulation $\Gamma(y)$ of these trailing shed vortices is zero at the tips and usually a maximum at the center plane, or root, of the wing. In 1918 Prandtl successfully modeled this flow by replacing the wing by a single lifting line and a continuous sheet of semi-infinite trailing vortices of strength $\gamma(y) = d\Gamma/dy$, as in Fig. 8.22*c*. Each elemental piece of trailing sheet $\gamma(\eta) d\eta$ induces a downwash, or downward velocity, $dw(y)$, given by

$$dw(y) = \frac{\gamma(\eta) d\eta}{4\pi(y - \eta)}$$

at position y on the lifting line. Note the denominator term 4π rather than 2π because the trailing vortex extends only from 0 to ∞ rather than from $-\infty$ to $+\infty$.

The total downwash $w(y)$ induced by the entire trailing vortex system is thus

$$w(y) = \frac{1}{4\pi} \int_{-(1/2)b}^{(1/2)b} \frac{\gamma(\eta) d\eta}{y - \eta} \quad (8.72)$$

When the downwash is vectorially added to the approaching free stream U_∞ , the effective angle of attack at this section of the wing is reduced to

$$\alpha_{\text{eff}} = \alpha - \alpha_i \quad \alpha_i = \tan^{-1} \frac{w}{U_\infty} \approx \frac{w}{U_\infty} \quad (8.73)$$

where we have used a small-amplitude approximation $w \ll U_\infty$.

The final step is to assume that the local circulation $\Gamma(y)$ is equal to that of a two-dimensional wing of the same shape and same effective angle of attack. From thin-airfoil theory, Eqs. (8.55) and (8.64), we have the estimate

$$C_L = \frac{\rho U_\infty \Gamma b}{\frac{1}{2} \rho U_\infty^2 b C} \approx 2\pi \alpha_{\text{eff}}$$

or

$$\Gamma \approx \pi C U_\infty \alpha_{\text{eff}} \quad (8.74)$$

Combining Eqs. (8.72) and (8.74), we obtain Prandtl's lifting-line theory for a finite-span wing

$$\Gamma(y) = \pi C(y) U_\infty \left[\alpha(y) - \frac{1}{4\pi U_\infty} \int_{-(1/2)b}^{(1/2)b} \frac{(d\Gamma/d\eta) d\eta}{y - \eta} \right] \quad (8.75)$$

This is an integrodifferential equation to be solved for $\Gamma(y)$ subject to the conditions $\Gamma(\frac{1}{2}b) = \Gamma(-\frac{1}{2}b) = 0$. It is similar to the thin-airfoil integral equation (8.61) and even more formidable. Once it is solved, the total wing lift and induced drag are given by

$$L = \rho U_\infty \int_{-(1/2)b}^{(1/2)b} \Gamma(y) dy \quad D_i = \rho U_\infty \int_{-(1/2)b}^{(1/2)b} \Gamma(y) \alpha_i(y) dy \quad (8.76)$$

Here is a case where the drag is not zero in a frictionless theory because the downwash causes the lift to slant backward by angle α_i so that it has a drag component parallel to the free-stream direction, $dD_i = dL \sin \alpha_i \approx dL \alpha_i$.

The complete solution to Eq. (8.75) for arbitrary wing planform $C(y)$ and arbitrary

twist $\alpha(y)$ is treated in advanced texts [for example, 11]. It turns out that there is a simple representative solution for an untwisted wing of elliptical planform

$$C(y) = C_0 \left[1 - \left(\frac{2y}{b} \right)^2 \right]^{1/2} \quad (8.77)$$

The area and aspect ratio of this wing are

$$A_p = \int_{-(1/2)b}^{(1/2)b} C \, dy = \frac{1}{4} \pi b C_0 \quad AR = \frac{4b}{\pi C_0} \quad (8.78)$$

The solution to Eq. (8.75) for this $C(y)$ is an elliptical circulation distribution of exactly similar shape

$$\Gamma(y) = \Gamma_0 \left[1 - \left(\frac{2y}{b} \right)^2 \right]^{1/2} \quad (8.79)$$

Substituting into Eq. (8.75) and integrating give a relation between Γ_0 and C_0

$$\Gamma_0 = \frac{\pi C_0 U_\infty \alpha}{1 + 2/AR} \quad (8.80)$$

where α is assumed constant across the untwisted wing.

Substitution into Eq. (8.76) gives the elliptical-wing lift

$$L = \frac{1}{4} \pi^2 b C_0 \rho U_\infty^2 \alpha / (1 + 2/AR)$$

or

$$C_L = \frac{2\pi\alpha}{1 + 2/AR} \quad (8.81)$$

If we generalize this to a thick cambered finite wing of approximately elliptical planform, we obtain

$$C_L = \frac{2\pi \sin(\alpha + \beta)}{1 + 2/AR} \quad (8.82)$$

This result was given without proof as Eq. (7.70). From Eq. (8.72) the computed downwash for the elliptical wing is constant

$$w(y) = \frac{2U_\infty \alpha}{2 + AR} = \text{const} \quad (8.83)$$

Finally, the induced drag coefficient from Eq. (8.76) is

$$C_{Di} = C_L \frac{w}{U_\infty} = \frac{C_L^2}{\pi AR} \quad (8.84)$$

This was given without proof as Eq. (7.71).

Figure 8.23 shows the effectiveness of this theory when tested against a nonelliptical cambered wing by Prandtl in 1921 [14]. Figure 8.23a and b shows the measured lift curves and drag polars for five different aspect ratios. Note the increase in stall angle and drag and the decrease in lift slope as the aspect ratio decreases.

Figure 8.23c shows the lift data replotted against effective angle of attack $\alpha_{\text{eff}} = (\alpha + \beta)/(1 + 2/AR)$, as predicted by Eq. (8.82). These curves should be equivalent to

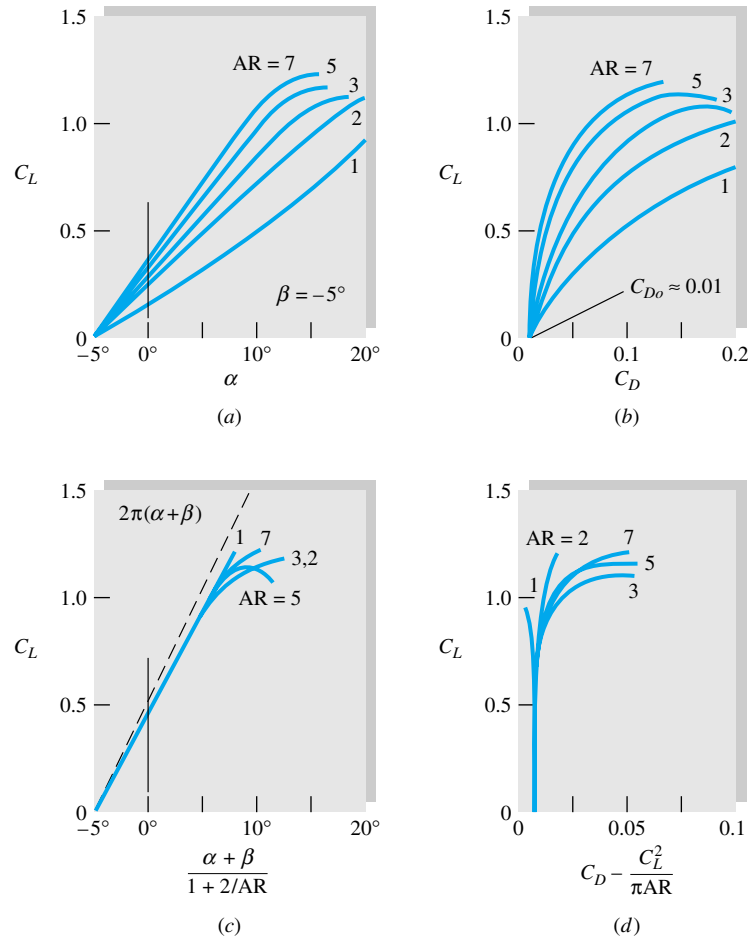


Fig. 8.23 Comparison of theory and experiment for a finite wing: (a) measured lift [14]; (b) measured drag polar [14]; (c) lift reduced to infinite aspect ratio; (d) drag polar reduced to infinite aspect ratio.

an infinite-aspect-ratio wing, and they do collapse together except near stall. Their common slope $dC_L/d\alpha$ is about 10 percent less than the theoretical value 2π , but this is consistent with the thickness and shape effects noted in Fig. 8.20.

Figure 8.23d shows the drag data replotted with the theoretical induced drag $C_{Di} = C_L^2 / (\pi AR)$ subtracted out. Again, except near stall, the data collapse onto a single line of nearly constant infinite-aspect-ratio drag $C_{D0} \approx 0.01$. We conclude that the finite-wing theory is very effective and may be used for design calculations.

8.8 Axisymmetric Potential Flow⁵

The same superposition technique which worked so well for plane flow in Sec. 8.3 is also successful for axisymmetric potential flow. We give some brief examples here.

Most of the basic results carry over from plane to axisymmetric flow with only slight changes owing to the geometric differences. Consider the following related flows:

⁵ This section may be omitted without loss of continuity.

Basic plane flow	Counterpart axisymmetric flow
Uniform stream	Uniform stream
Line source or sink	Point source or sink
Line doublet	Point doublet
Line vortex	No counterpart
Rankine half-body cylinder	Rankine half-body of revolution
Rankine-oval cylinder	Rankine oval of revolution
Circular cylinder	Sphere
Symmetric airfoil	Tear-shaped body

Since there is no such thing as a point vortex, we must forgo the pleasure of studying circulation effects in axisymmetric flow. However, as any smoker knows, there is an axisymmetric ring vortex, and there are also ring sources and ring sinks, which we leave to advanced texts [for example, 3].

Spherical Polar Coordinates

Axisymmetric potential flows are conveniently treated in the spherical polar coordinates of Fig. 8.24. There are only two coordinates (r , θ), and flow properties are constant on a circle of radius $r \sin \theta$ about the x -axis.

The equation of continuity for incompressible flow in these coordinates is

$$\frac{\partial}{\partial r} (r^2 v_r \sin \theta) + \frac{\partial}{\partial \theta} (r v_\theta \sin \theta) = 0 \quad (8.85)$$

where v_r and v_θ are radial and tangential velocity as shown. Thus a spherical polar stream function⁶ exists such that

$$v_r = -\frac{1}{r^2 \sin \theta} \frac{\partial \psi}{\partial \theta} \quad v_\theta = \frac{1}{r \sin \theta} \frac{\partial \psi}{\partial r} \quad (8.86)$$

In like manner a velocity potential $\phi(r, \theta)$ exists such that

$$v_r = \frac{\partial \phi}{\partial r} \quad v_\theta = \frac{1}{r} \frac{\partial \phi}{\partial \theta} \quad (8.87)$$

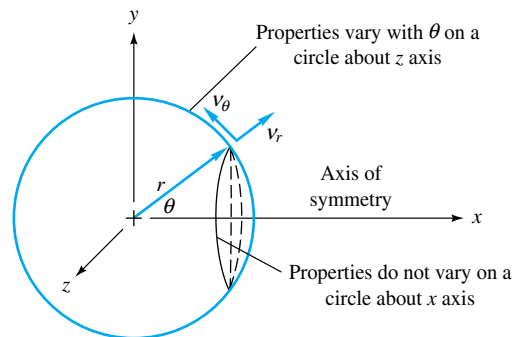


Fig. 8.24 Spherical polar coordinates for axisymmetric flow.

⁶ It is often called *Stokes' stream function*, having been used in a paper Stokes wrote in 1851 on viscous sphere flow.

These formulas serve to deduce the ψ and ϕ functions for various elementary-axisymmetric potential flows.

Uniform Stream in the x Direction A stream U_∞ in the x direction has components

$$v_r = U_\infty \cos \theta \quad v_\theta = -U_\infty \sin \theta$$

Substitution into Eqs. (8.86) and (8.87) and integrating give

$$\text{Uniform stream:} \quad \psi = -\frac{1}{2}U_\infty r^2 \sin^2 \theta \quad \phi = U_\infty r \cos \theta \quad (8.88)$$

As usual, arbitrary constants of integration have been neglected.

Point Source or Sink

Consider a volume flux Q issuing from a point source. The flow will spread out radially and at radius r will equal Q divided by the area $4\pi r^2$ of a sphere. Thus

$$v_r = \frac{Q}{4\pi r^2} = \frac{m}{r^2} \quad v_\theta = 0 \quad (8.89)$$

with $m = Q/(4\pi)$ for convenience. Integrating (8.86) and (8.87) gives

$$\text{Point source} \quad \psi = m \cos \theta \quad \phi = -\frac{m}{r} \quad (8.90)$$

For a point sink, change m to $-m$ in Eq. (8.90).

Point Doublet

Exactly as in Fig. 8.8, place a source at $(x, y) = (-a, 0)$ and an equal sink at $(+a, 0)$, taking the limit as a becomes small with the product $2am = \lambda$ held constant

$$\psi_{\text{doublet}} = \lim_{\substack{a \rightarrow 0 \\ 2am = \lambda}} (m \cos \theta_{\text{source}} - m \cos \theta_{\text{sink}}) = \frac{\lambda \sin^2 \theta}{r} \quad (8.91)$$

We leave the proof of this limit as a problem. The point-doublet velocity potential

$$\phi_{\text{doublet}} = \lim_{\substack{a \rightarrow 0 \\ 2am = \lambda}} \left(-\frac{m}{r_{\text{source}}} + \frac{m}{r_{\text{sink}}} \right) = \frac{\lambda \cos \theta}{r^2} \quad (8.92)$$

The streamlines and potential lines are shown in Fig. 8.25. Unlike the plane doublet flow of Fig. 8.8, neither set of lines represents perfect circles.

Uniform Stream plus a Point Source

By combining Eqs. (8.88) and (8.90) we obtain the stream function for a uniform stream plus a point source at the origin

$$\psi = -\frac{1}{2}U_\infty r^2 \sin^2 \theta + m \cos \theta \quad (8.93)$$

From Eq. (8.86) the velocity components are, by differentiation,

$$v_r = U_\infty \cos \theta + \frac{m}{r^2} \quad v_\theta = -U_\infty \sin \theta \quad (8.94)$$

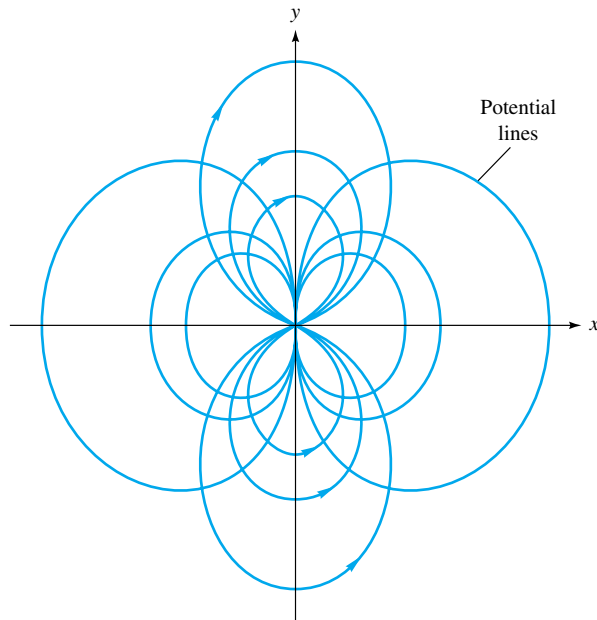


Fig. 8.25 Streamlines and potential lines due to a point doublet at the origin, from Eqs. (8.91) and (8.92).

Setting these equal to zero reveals a stagnation point at $\theta = 180^\circ$ and $r = a = (m/U_\infty)^{1/2}$, as shown in Fig. 8.26. If we let $m = U_\infty a^2$, the stream function can be rewritten as

$$\frac{\psi}{U_\infty a^2} = \cos \theta - \frac{1}{2} \left(\frac{r}{a} \right)^2 \sin^2 \theta \quad (8.95)$$

The stream surface which passes through the stagnation point $(r, \theta) = (a, \pi)$ has the value $\psi = -U_\infty a^2$ and forms a half-body of revolution enclosing the point source, as shown in Fig. 8.26. This half-body can be used to simulate a pitot tube. Far downstream the half-body approaches the constant radius $R = 2a$ about the x -axis. The maximum velocity and minimum pressure along the half-body surface occur at $\theta = 70.5^\circ$,

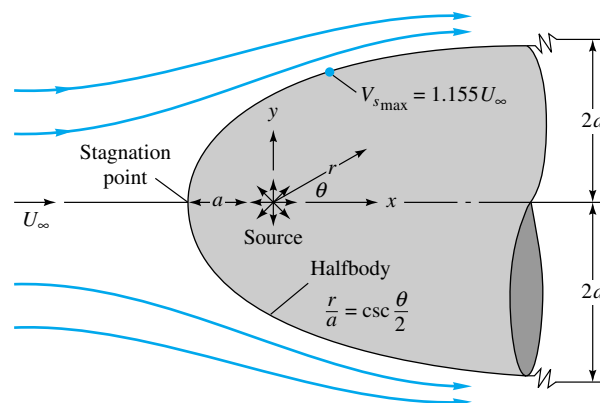


Fig. 8.26 Streamlines for a Rankine half-body of revolution.

$r = a\sqrt{3}$, $V_s = 1.155U_\infty$. Downstream of this point there is an adverse gradient as V_s slowly decelerates to U_∞ , but boundary-layer theory indicates no flow separation. Thus Eq. (8.95) is a very realistic simulation of a real half-body flow. But when the uniform stream is added to a sink to form a half-body rear surface, e.g., similar to Fig. 8.5c, separation is predicted and the inviscid pattern is not realistic.

Uniform Stream plus a Point Doublet

From Eqs. (8.88) and (8.91), combination of a uniform stream and a point doublet at the origin gives

$$\psi = -\frac{1}{2} U_\infty r^2 \sin^2 \theta + \frac{\lambda}{r} \sin^2 \theta \quad (8.96)$$

Examination of this relation reveals that the stream surface $\psi = 0$ corresponds to the sphere of radius

$$r = a = \left(\frac{2\lambda}{U_\infty}\right)^{1/3} \quad (8.97)$$

This is exactly analogous to the cylinder flow of Fig. 8.10a formed by combining a uniform stream and a line doublet.

Letting $\lambda = \frac{1}{2}U_\infty a^3$ for convenience, we rewrite Eq. (8.96) as

$$\frac{\psi}{\frac{1}{2}U_\infty a^2} = -\sin^2 \theta \left(\frac{r^2}{a^2} - \frac{a}{r}\right) \quad (8.98)$$

The streamlines for this sphere flow are plotted in Fig. 8.27. By differentiation from Eq. (8.86) the velocity components are

$$v_r = U_\infty \cos \theta \left(1 - \frac{a^3}{r^3}\right) \quad v_\theta = -\frac{1}{2} U_\infty \sin \theta \left(2 + \frac{a^3}{r^3}\right) \quad (8.99)$$

We see that the radial velocity vanishes at the sphere surface $r = a$, as expected. There is a stagnation point at the front (a, π) and the rear ($a, 0$) of the sphere. The maximum

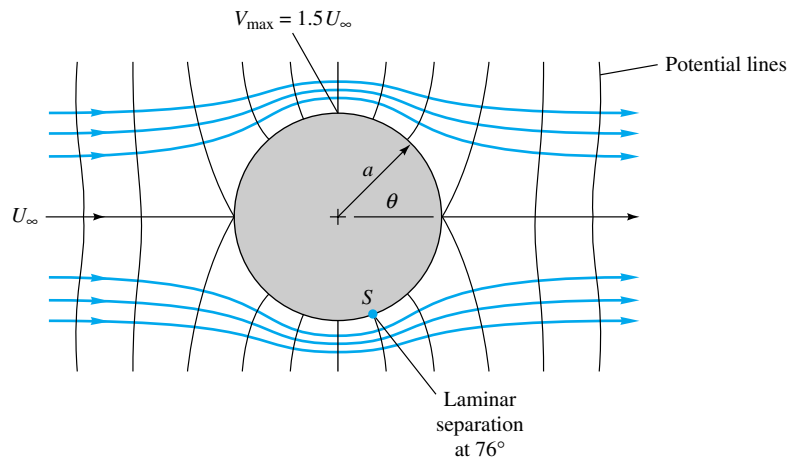


Fig. 8.27 Streamlines and potential lines for inviscid flow past a sphere.

velocity occurs at the shoulder ($a, \pm\frac{1}{2}\pi$), where $v_r = 0$ and $v_\theta = -1.5U_\infty$. The surface-velocity distribution is

$$V_s = -v_\theta|_{r=a} = \frac{3}{2}U_\infty \sin \theta \quad (8.100)$$

Note the similarity to the cylinder surface velocity equal to $2U_\infty \sin \theta$ from Eq. (8.34) with zero circulation.

Equation (8.100) predicts, as expected, an adverse pressure gradient on the rear ($\theta < 90^\circ$) of the sphere. If we use this distribution with laminar-boundary-layer theory [for example, 15, p. 298], separation is computed to occur at about $\theta = 76^\circ$, so that in the actual flow pattern of Fig. 7.14 a broad wake forms in the rear. This wake interacts with the free stream and causes Eq. (8.100) to be inaccurate even in the front of the sphere. The measured maximum surface velocity is equal only to about $1.3U_\infty$ and occurs at about $\theta = 107^\circ$ (see Ref. 15, sec. 4.10.4, for further details).

The Concept of Hydrodynamic Mass

When a body moves through a fluid, it must push a finite mass of fluid out of the way. If the body is accelerated, the surrounding fluid must also be accelerated. The body behaves as if it were heavier by an amount called the *hydrodynamic mass* (also called the *added* or *virtual mass*) of the fluid. If the instantaneous body velocity is $\mathbf{U}(t)$, the summation of forces must include this effect

$$\Sigma \mathbf{F} = (m + m_h) \frac{d\mathbf{U}}{dt} \quad (8.101)$$

where m_h , the hydrodynamic mass, is a function of body shape, the direction of motion, and (to a lesser extent) flow parameters such as the Reynolds number.

According to potential theory [2, sec. 6.4; 3, sec. 9.22], m_h depends only on the shape and direction of motion and can be computed by summing the total kinetic energy of the fluid relative to the body and setting this equal to an equivalent body energy

$$\text{KE}_{\text{fluid}} = \int \frac{1}{2} dm V_{\text{rel}}^2 = \frac{1}{2} m_h U^2 \quad (8.102)$$

The integration of fluid kinetic energy can also be accomplished by a body-surface integral involving the velocity potential [16, sec. 11].

Consider the previous example of a sphere immersed in a uniform stream. By subtracting out the stream velocity we can replot the flow as in Fig. 8.28, showing the streamlines relative to the moving sphere. Note the similarity to the doublet flow in Fig. 8.25. The relative-velocity components are found by subtracting U from Eqs. (8.99)

$$v_r = -\frac{Ua^3 \cos \theta}{r^3} \quad v_\theta = -\frac{Ua^3 \sin \theta}{2r^3}$$

The element of fluid mass, in spherical polar coordinates, is

$$dm = \rho(2\pi r \sin \theta) r dr d\theta$$

When dm and $V_{\text{rel}}^2 = v_r^2 + v_\theta^2$ are substituted into Eq. (8.102), the integral can be evaluated

$$\text{KE}_{\text{fluid}} = \frac{1}{3} \rho \pi a^3 U^2$$

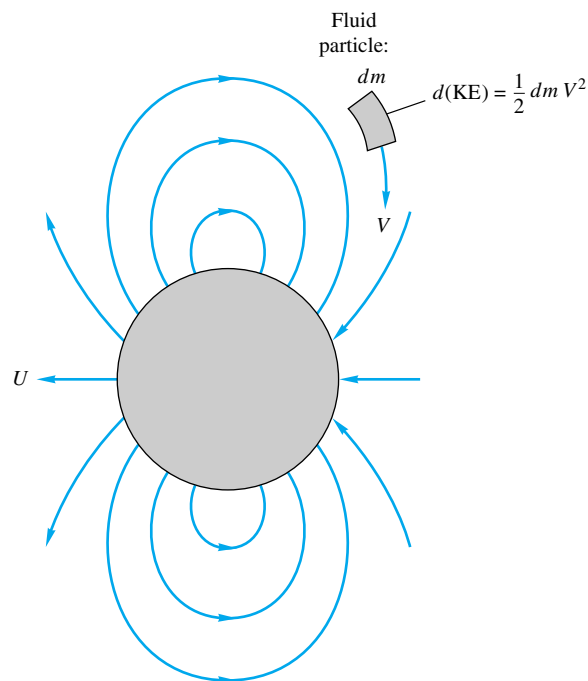


Fig. 8.28 Potential-flow streamlines relative to a moving sphere. Compare with Figs. 8.25 and 8.27.

$$\text{or} \quad m_h(\text{sphere}) = \frac{2}{3} \rho \pi a^3 \quad (8.103)$$

Thus, according to potential theory, the hydrodynamic mass of a sphere equals one-half of its displaced mass, independent of the direction of motion.

A similar result for a cylinder moving normal to its axis can be computed from Eqs. (8.33) after subtracting out the stream velocity. The result is

$$m_h(\text{cylinder}) = \rho \pi a^2 L \quad (8.104)$$

for a cylinder of length L , assuming two-dimensional motion. The cylinder's hydrodynamic mass equals its displaced mass.

Tables of hydrodynamic mass for various body shapes and directions of motion are given by Patton [17]. See also Ref. 21.

8.9 Numerical Analysis

When potential flow involves complicated geometries or unusual stream conditions, the classical superposition scheme of Secs. 8.3 and 8.4 becomes less attractive. Conformal mapping of body shapes, by using the complex-variable technique of Sec. 8.5, is no longer popular. Numerical analysis is the appropriate modern approach, and at least three different approaches are in use:

1. The finite-element method (FEM) [6, 19]
2. The finite-difference method (FDM) [5, 20]
3. *a.* Integral methods with distributed singularities [18]
b. The boundary-element method [7]

Methods 3a and 3b are closely related, having first been developed on an ad hoc basis by aerodynamicists in the 1960s [18] and then generalized into a multipurpose applied-mechanics technique in the 1970s [7].

Methods 1 (or FEM) and 2 (or FDM), though strikingly different in concept, are comparable in scope, mesh size, and general accuracy. We concentrate here on the latter method for illustration purposes.

The Finite-Element Method

The finite-element method [19] is applicable to all types of linear and nonlinear partial differential equations in physics and engineering. The computational domain is divided into small regions, usually triangular or quadrilateral. These regions are delineated with a finite number of *nodes* where the field variables—temperature, velocity, pressure, stream function, etc.—are to be calculated. The solution in each region is approximated by an algebraic combination of local nodal values. Then the approximate functions are integrated over the region, and their error is minimized, often by using a weighting function. This process yields a set of N algebraic equations for the N unknown nodal values. The nodal equations are solved simultaneously, by matrix inversion or iteration. For further details see Ref. 6 or 19.

The Finite-Difference Method

Although textbooks on numerical analysis [5, 20] apply finite-difference techniques to many different problems, here we concentrate on potential flow. The idea of FDM is to approximate the partial derivatives in a physical equation by “differences” between nodal values spaced a finite distance apart—a sort of numerical calculus. The basic partial differential equation is thus replaced by a set of algebraic equations for the nodal values. For potential (inviscid) flow, these algebraic equations are linear, but they are generally nonlinear for viscous flows. The solution for nodal values is obtained by iteration or matrix inversion. Nodal spacings need not be equal.

Here we illustrate the two-dimensional Laplace equation, choosing for convenience the stream-function form

$$\frac{\partial^2 \psi}{\partial x^2} + \frac{\partial^2 \psi}{\partial y^2} = 0 \quad (8.105)$$

subject to known values of ψ along any body surface and known values of $\partial\psi/\partial x$ and $\partial\psi/\partial y$ in the free stream.

Our finite-difference technique divides the flow field into equally spaced nodes, as shown in Fig. 8.29. To economize on the use of parentheses or functional notation, subscripts i and j denote the position of an arbitrary, equally spaced node, and $\psi_{i,j}$ denotes the value of the stream function at that node

$$\psi_{i,j} = \psi(x_0 + i \Delta x, y_0 + j \Delta y)$$

Thus, $\psi_{i+1,j}$ is just to the right of $\psi_{i,j}$, and $\psi_{i,j+1}$ is just above.

An algebraic approximation for the derivative $\partial\psi/\partial x$ is

$$\frac{\partial\psi}{\partial x} \approx \frac{\psi(x + \Delta x, y) - \psi(x, y)}{\Delta x}$$

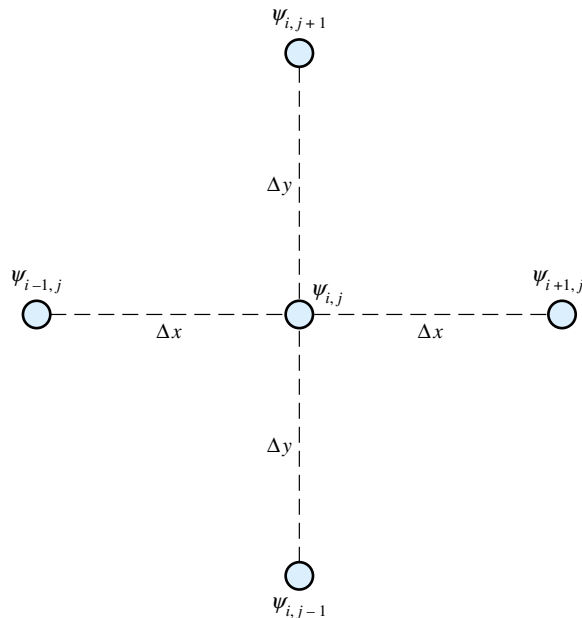


Fig. 8.29 Definition sketch for a two-dimensional rectangular finite-difference grid.

A similar approximation for the second derivative is

$$\frac{\partial^2 \psi}{\partial x^2} \approx \frac{1}{\Delta x} \left[\frac{\psi(x + \Delta x, y) - \psi(x, y)}{\Delta x} - \frac{\psi(x, y) - \psi(x - \Delta x, y)}{\Delta x} \right]$$

The subscript notation makes these expressions more compact

$$\begin{aligned} \frac{\partial \psi}{\partial x} &\approx \frac{1}{\Delta x} (\psi_{i+1,j} - \psi_{i,j}) \\ \frac{\partial^2 \psi}{\partial x^2} &\approx \frac{1}{\Delta x^2} (\psi_{i+1,j} - 2\psi_{i,j} + \psi_{i-1,j}) \end{aligned} \quad (8.106)$$

These formulas are exact in the calculus limit as $\Delta x \rightarrow 0$, but in numerical analysis we keep Δx and Δy finite, hence the term *finite differences*.

In an exactly similar manner we can derive the equivalent difference expressions for the y direction

$$\begin{aligned} \frac{\partial \psi}{\partial y} &\approx \frac{1}{\Delta y} (\psi_{i,j+1} - \psi_{i,j}) \\ \frac{\partial^2 \psi}{\partial y^2} &\approx \frac{1}{\Delta y^2} (\psi_{i,j+1} - 2\psi_{i,j} + \psi_{i,j-1}) \end{aligned} \quad (8.107)$$

The use of subscript notation allows these expressions to be programmed directly into a scientific computer language such as BASIC or FORTRAN.

When (8.106) and (8.107) are substituted into Laplace's equation (8.105), the result is the algebraic formula

$$2(1 + \beta)\psi_{i,j} \approx \psi_{i-1,j} + \psi_{i+1,j} + \beta(\psi_{i,j-1} + \psi_{i,j+1}) \quad (8.108)$$

where $\beta = (\Delta x/\Delta y)^2$ depends upon the mesh size selected. This finite-difference model of Laplace's equation states that every nodal stream-function value $\psi_{i,j}$ is a linear combination of its four nearest neighbors.

The most commonly programmed case is a square mesh ($\beta = 1$), for which Eq. (8.108) reduces to

$$\psi_{i,j} \approx \frac{1}{4}(\psi_{i,j+1} + \psi_{i,j-1} + \psi_{i+1,j} + \psi_{i-1,j}) \quad (8.109)$$

Thus, for a square mesh, each nodal value equals the arithmetic average of the four neighbors shown in Fig. 8.29. The formula is easily remembered and easily programmed. If $P(I, J)$ is a subscripted variable stream function, the BASIC or FORTRAN statement of (8.109) is

$$P(I, J) = 0.25 * (P(I, J + 1) + P(I, J - 1) + P(I + 1, J) + P(I - 1, J)) \quad (8.110)$$

This is applied in iterative fashion sweeping over each of the internal nodes (I, J) , with known values of P specified at each of the surrounding boundary nodes. Any initial guesses can be specified for the internal nodes $P(I, J)$, and the iteration process will converge to the final algebraic solution in a finite number of sweeps. The numerical error, compared with the exact solution of Laplace's equation, is proportional to the square of the mesh size.

Convergence can be speeded up by the *successive overrelaxation* (SOR) method, discussed by Patankar [5]. The modified SOR form of the iteration is

$$\begin{aligned} P(I, J) = & P(I, J) + 0.25 * A * (P(I, J + 1) + P(I, J - 1) \\ & + P(I + 1, J) + P(I - 1, J) - 4 * P(I, J)) \end{aligned} \quad (8.111)$$

The recommended value of the SOR convergence factor A is about 1.7. Note that the value $A = 1.0$ reduces Eq. (8.111) to (8.110).

Let us illustrate the finite-difference method with an example.

EXAMPLE 8.5

Make a numerical analysis, using $\Delta x = \Delta y = 0.2$ m, of potential flow in the duct expansion shown in Fig. 8.30. The flow enters at a uniform 10 m/s, where the duct width is 1 m, and is assumed to leave at a uniform velocity of 5 m/s, where the duct width is 2 m. There is a straight section 1 m long, a 45° expansion section, and a final straight section 1 m long.

Solution

Using the mesh shown in Fig. 8.30 results in 45 boundary nodes and 91 internal nodes, with i varying from 1 to 16 and j varying from 1 to 11. The internal points are modeled by Eq. (8.110). For convenience, let the stream function be zero along the lower wall. Then since the volume flow is $(10 \text{ m/s})(1 \text{ m}) = 10 \text{ m}^2/\text{s}$ per unit depth, the stream function must equal $10 \text{ m}^2/\text{s}$ along the upper wall. Over the entrance and exit planes, the stream function must vary linearly to give uniform velocities:

$$\begin{aligned} \text{Inlet:} & \quad \psi(1, J) = 2 * (J - 6) & \quad \text{for } J = 7 \text{ to } 10 \\ \text{Exit:} & \quad \psi(16, J) = J - 1 & \quad \text{for } J = 2 \text{ to } 10 \end{aligned}$$

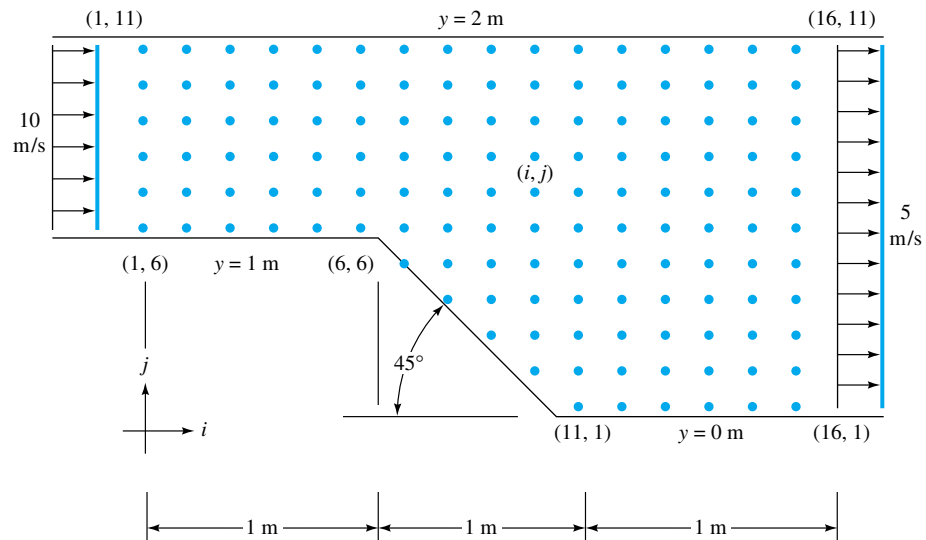


Fig. 8.30 Numerical model of potential flow through a two-dimensional 45° expansion. The nodal points shown are 20 cm apart. There are 45 boundary nodes and 91 internal nodes.

All these boundary values must be input to the program and are shown printed in Fig. 8.31.

Initial guesses are stored for the internal points, say, zero or an average value of $5.0 \text{ m}^2/\text{s}$. The program then starts at any convenient point, such as the upper left (2, 10), and evaluates Eq. (8.110) at every internal point, repeating this sweep iteratively until there are no further changes (within some selected maximum change) in the nodal values. The results are the finite-difference simulation of this potential flow for this mesh size; they are shown printed in Fig. 8.31 to three-digit accuracy. The reader should test a few nodes in Fig. 8.31 to verify that Eq. (8.110) is satisfied everywhere. The numerical accuracy of these printed values is difficult to estimate, since there is no known exact solution to this problem. In practice, one would keep decreasing the mesh size to see whether there were any significant changes in nodal values.

This problem is well within the capability of a small personal computer. The values shown in Fig. 8.31 were obtained after 100 iterations, or 6 min of execution time, on a Macintosh SE personal computer, using BASIC.

$\psi = 10.00$	10.00	10.00	10.00	10.00	10.00	10.00	10.00	10.00	10.00	10.00	10.00	10.00	10.00	10.00	10.00	
	8.00	8.02	8.04	8.07	8.12	8.20	8.30	8.41	8.52	8.62	8.71	8.79	8.85	8.91	8.95	9.00
	6.00	6.03	6.06	6.12	6.22	6.37	6.58	6.82	7.05	7.26	7.44	7.59	7.71	7.82	7.91	8.00
	4.00	4.03	4.07	4.13	4.26	4.48	4.84	5.24	5.61	5.93	6.19	6.41	6.59	6.74	6.88	7.00
	2.00	2.02	2.05	2.09	2.20	2.44	3.08	3.69	4.22	4.65	5.00	5.28	5.50	5.69	5.85	6.00
$\psi = 0.00$	0.00	0.00	0.00	0.00	0.00	0.00	1.33	2.22	2.92	3.45	3.87	4.19	4.45	4.66	4.84	5.00
							0.00	1.00	1.77	2.37	2.83	3.18	3.45	3.66	3.84	4.00
								0.00	0.80	1.42	1.90	2.24	2.50	2.70	2.86	3.00
									0.00	0.63	1.09	1.40	1.61	1.77	1.89	2.00
										0.00	0.44	0.66	0.79	0.87	0.94	1.00
											0.00	0.00	0.00	0.00	0.00	0.00

Fig. 8.31 Stream-function nodal values for the potential flow of Fig. 8.30. Boundary values are known inputs. Internal nodes are solutions to Eq. (8.110).

Although Fig. 8.31 is the computer solution to the problem, these numbers must be manipulated to yield practical engineering results. For example, one can interpolate these numbers to sketch various streamlines of the flow. This is done in Fig. 8.32*a*. We see that the streamlines are curved both upstream and downstream of the corner regions, especially near the lower wall. This indicates that the flow is not one-dimensional.

The velocities at any point in the flow can be computed from finite-difference formulas such as Eqs. (8.106) and (8.107). For example, at the point $(I, J) = (3, 6)$, from Eq. (8.107), the horizontal velocity is approximately

$$u(3, 6) \approx \frac{\psi(3, 7) - \psi(3, 6)}{\Delta y} = \frac{2.09 - 0.00}{0.2} = 10.45 \text{ m/s}$$

and the vertical velocity is zero from Eq. (8.106). Directly above this on the upper wall, we estimate

$$u(3, 11) \approx \frac{\psi(3, 11) - \psi(3, 10)}{\Delta y} = \frac{10.00 - 8.07}{0.2} = 9.65 \text{ m/s}$$

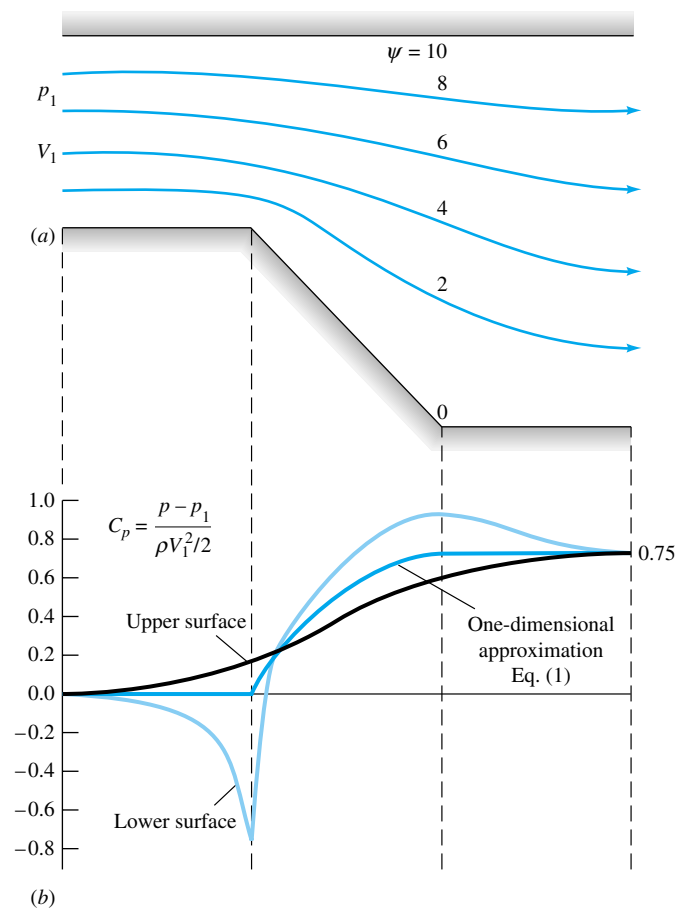


Fig. 8.32 Useful results computed from Fig. 8.31: (a) streamlines of the flow; (b) pressure-coefficient distribution along each wall.

The flow is not truly one-dimensional in the entrance duct. The lower wall, which contains the diverging section, accelerates the fluid, while the flat upper wall is actually decelerating the fluid.

Another output function, useful in making boundary-layer analyses of the wall regions, is the pressure distribution along the walls. If p_1 and V_1 are the pressure and velocity at the entrance ($I = 1$), conditions at any other point are computed from Bernoulli's equation (8.3), neglecting gravity

$$p + \frac{1}{2}\rho V^2 = p_1 + \frac{1}{2}\rho V_1^2$$

which can be rewritten as a dimensionless pressure coefficient

$$C_p = \frac{p - p_1}{\frac{1}{2}\rho V_1^2} = 1 - \left(\frac{V}{V_1}\right)^2$$

This determines p after V is computed from the stream-function differences in Fig. 8.31.

Figure 8.32*b* shows the computed wall-pressure distributions as compared with the one-dimensional continuity approximation $V_1 A_1 \approx V(x)A(x)$, or

$$C_p(\text{one-dim}) \approx 1 - \left(\frac{A_1}{A}\right)^2 \quad (1)$$

The one-dimensional approximation, which is rather crude for this large (45°) expansion, lies between the upper and lower wall pressures. One-dimensional theory would be much more accurate for a 10° expansion.

Analyzing Fig. 8.32*b*, we predict that boundary-layer separation will probably occur on the lower wall between the corners, where pressure is strongly rising (highly adverse gradient). Therefore potential theory is probably not too realistic for this flow, where viscous effects are strong. (Recall Figs. 6.27 and 7.8.)

Potential theory is *reversible*; i.e., when we reverse the flow arrows in Fig. 8.32*a*, then Fig. 8.32*b* is still valid and would represent a 45° contraction flow. The pressure would fall on both walls (no separation) from $x = 3$ m to $x = 1$ m. Between $x = 1$ m and $x = 0$, the pressure rises on the lower surface, indicating possible separation, probably just downstream of the corner.

This example should give the reader an idea of the usefulness and generality of numerical analysis of fluid flows.

The Boundary-Element Method

A relatively new technique for numerical solution of partial differential equations is the *boundary-element method* (BEM). Reference 7 is an introductory textbook outlining the concepts of BEM, including FORTRAN programs for potential theory and elastostatics. There are no interior elements. Rather, all nodes are placed on the boundary of the domain, as in Fig. 8.33. The “element” is a small piece of the boundary surrounding the node. The “strength” of the element can be either constant or variable.

For plane potential flow, the method takes advantage of the particular solution

$$\psi^* = \frac{1}{2\pi} \ln \frac{1}{r} \quad (8.112)$$

which satisfies Laplace's equation, $\nabla^2 \psi = 0$. Each element i is assumed to have a different strength ψ_i . Then r represents the distance from that element to any other point in the flow field. Summing all these elemental effects, with proper boundary conditions, will give the total solution to the potential-flow problem.

At each element of the boundary, we typically know either the value of ψ or the value of $\partial\psi/\partial n$, where n is normal to the boundary. (Mixed combinations of ψ and

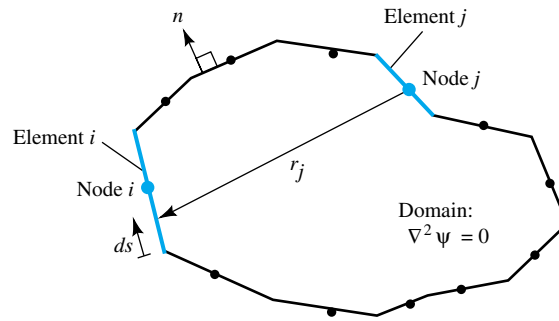


Fig. 8.33 Boundary elements of constant strength in plane potential flow.

$\partial\psi/\partial n$ are also possible but are not discussed here.) The correct strengths ψ_i are such that these boundary conditions are satisfied at every element. Summing these effects over N elements requires integration by parts plus a careful evaluation of the (singular) effect of element i upon itself. The mathematical details are given in Ref. 7. The result is a set of N algebraic equations for the unknown boundary values. In the case of elements of constant strength, the final expression is

$$\frac{1}{2} \psi_i + \sum_{j=1}^N \psi_j \left(\int_j \frac{\partial\psi^*}{\partial n} ds \right) = \sum_{j=1}^N \left(\frac{\partial\psi}{\partial n} \right)_j \left(\int_j \psi^* ds \right) \quad i = 1 \text{ to } N \quad (8.113)$$

The integrals, which involve the logarithmic particular solution ψ^* from Eq. (8.112), are evaluated numerically for each element. Reference 7 recommends – and gives a program for – gaussian quadrature formulas.

Equations (8.113) contain $2N$ element values, ψ_i and $(\partial\psi/\partial n)_i$, of which N are known from the given boundary conditions. The remaining N are solved simultaneously from Eqs. (8.113). Generally this completes the analysis – only the boundary solution is computed, and interior points are not studied. In most cases, the boundary velocity and pressure are all that is needed.

We illustrated the method with stream function ψ . Naturally the entire technique also applies to velocity potential ϕ , if we are given proper conditions on ϕ or $\partial\phi/\partial n$ at each boundary element. The method is readily extended to three dimensions [7].

Reference 7 gives a complete FORTRAN listing for solving Eqs. (8.113) numerically for constant, linear, and quadratic element strength variations. We now use their constant-element-strength program, POCONBE [7], to take an alternate look at Example 8.5, which used the finite-difference method.

EXAMPLE 8.6

Solve the duct expansion problem, Example 8.5, using boundary elements. Use the same grid spacing $\Delta x = \Delta y = 0.2$ m for the element sizes.

Solution

The boundary nodes are equally spaced, as shown in Fig. 8.34. There are only 45 nodes, whereas there were 91 interior points for the FDM solution of Example 8.5. We expect the same accuracy for 50 percent fewer nodes. (Had we reduced the grid size to 0.1 m, there would be 90

nodes as opposed to 406 interior points — a savings of 78 percent.) The program POCONE [7] asks you to input the location of these 45 nodes. The stream-function values are known all around the boundary: ψ equals 0 on the bottom and 10.0 on the top and is linearly increasing from 0 to 10.0 at entrance and exit. These values of ψ , shown on the outside in Fig. 8.34, are inputted into the program.

Once the input of nodes and element values is complete, the program immediately computes and displays or stores the 45 unknowns, which in this case are the values of $\partial\psi/\partial n$ all around the boundary. These values are shown on the inside of the top and bottom surfaces in Fig. 8.34 and represent the local surface velocity near each element, in m/s. The values of $\partial\psi/\partial n$ at entrance and exit, which are small fractions representing vertical velocity components, are not shown here.

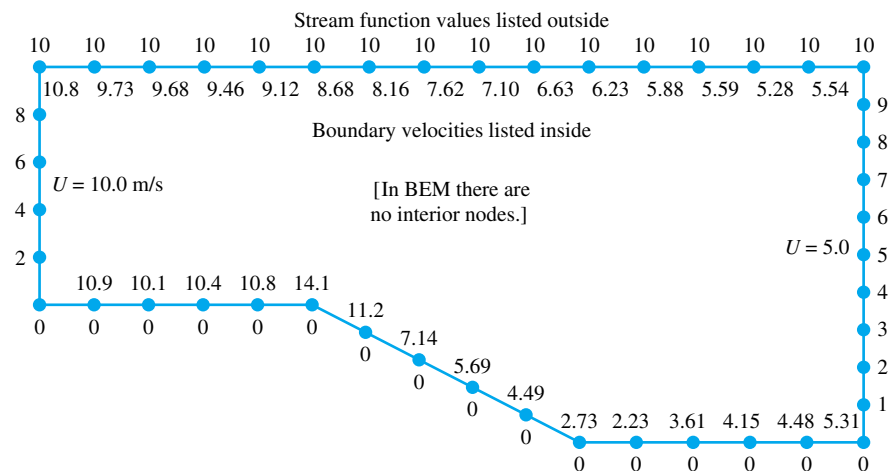


Fig. 8.34 Boundary elements corresponding to the same grid size as Fig. 8.31. Nodal values of stream function and computed surface velocity are shown.

The reader may verify that use of the surface velocities in Fig. 8.34 to compute surface pressure coefficients, as in Example 8.5, leads to curves very similar to those shown in Fig. 8.32. The BEM approach, using the same boundary nodes, has accuracy comparable to that for an FDM computation. For further details see Ref. 7.

Viscous-Flow Computer Models

Our previous finite-difference model of Laplace's equation, e.g., Eq. (8.109), was very well behaved and converged nicely with or without overrelaxation. Much more care is needed to model the full Navier-Stokes equations. The challenges are quite different, and they have been met to a large extent, so there are now many textbooks [20, 23 to 27] on (fully viscous) *computational fluid dynamics* (CFD). This is not a textbook on CFD, but we will address some of the issues in this section.

One-Dimensional Unsteady Flow

We begin with a simplified problem, showing that even a single viscous term introduces new effects and possible instabilities. Recall (or review) Prob. 4.85, where a wall moves and drives a viscous fluid parallel to itself. Gravity is neglected. Let the wall be the plane $y = 0$, moving at a speed $U_0(t)$, as in Fig. 8.35. A uniform vertical grid, of spacing Δy , has nodes n at which the local velocity u_n^j is to be calculated, where su-

perscript j denotes the time-step $j\Delta t$. The wall is $n = 1$. If $u = u(y, t)$ only and $v = w = 0$, continuity, $\nabla \cdot \mathbf{V} = 0$, is satisfied and we need only solve the x -momentum Navier-Stokes equation:

$$\frac{\partial u}{\partial t} = \nu \frac{\partial^2 u}{\partial y^2} \quad (8.114)$$

where $\nu = \mu/\rho$. Utilizing the same finite-difference approximations as in Eq. (8.106), we may model Eq. (8.114) algebraically as a forward time difference and a central spatial difference:

$$\frac{u_n^{j+1} - u_n^j}{\Delta t} \approx \nu \frac{u_{n+1}^j - 2u_n^j + u_{n-1}^j}{\Delta y^2}$$

Rearrange and find that we can solve explicitly for u_n at the next time-step $j + 1$:

$$u_n^{j+1} \approx (1 - 2\sigma) u_n^j + \sigma (u_{n-1}^j + u_{n+1}^j) \quad \sigma = \frac{\nu\Delta t}{\Delta y^2} \quad (8.115)$$

Thus u at node n at the next time-step $j + 1$ is a weighted average of three previous values, similar to the “four-nearest-neighbors” average in the laplacian model of Eq. (8.109). Since the new velocity is calculated immediately, Eq. (8.115) is called an *explicit* model. It differs from the well-behaved laplacian model, however, because it may be *unstable*. The weighting coefficients in Eq. (8.115) must all be positive to avoid divergence. Now σ is positive, but $(1 - 2\sigma)$ may not be. Therefore, our explicit viscous flow model has a stability requirement:

$$\sigma = \frac{\nu\Delta t}{\Delta y^2} \leq \frac{1}{2} \quad (8.116)$$

Normally one would first set up the mesh size Δy in Fig. 8.35, after which Eq. (8.116) would limit the time-step Δt . The solutions for nodal values would then be stable, but not necessarily that accurate. The mesh sizes Δy and Δt could be reduced to increase accuracy, similar to the case of the potential-flow laplacian model (8.109).

For example, to solve Prob. 4.85 numerically, one sets up a mesh with plenty of nodes (30 or more Δy within the expected viscous layer); selects Δt according to Eq.

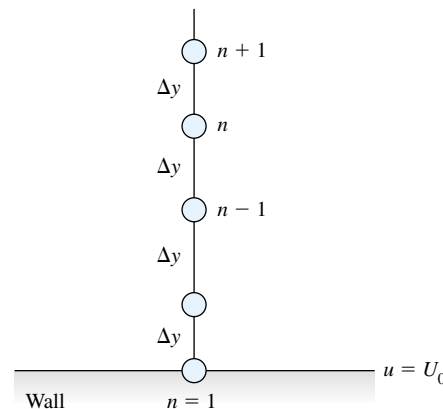


Fig. 8.35 An equally spaced finite-difference mesh for one-dimensional viscous flow [Eq. (8.114)].

(8.116); and sets two boundary conditions for all j : $u_1 = U_0 \sin \omega t^\dagger$ and $u_N = 0$, where N is the outermost node. For initial conditions, perhaps assume the fluid initially at rest: $u_n^1 = 0$ for $2 \leq n \leq N - 1$. Sweeping the nodes $2 \leq n \leq N - 1$ using Eq. (8.115) (an Excel spreadsheet is excellent for this), one generates numerical values of u_n^j for as long as one desires. After an initial transient, the final “steady” fluid oscillation will approach the classical solution in viscous-flow textbooks [15]. Try Prob. 8.115 to demonstrate this.

An Alternate Implicit Approach

In many finite-difference problems, a stability limitation such as Eq. (8.116) requires an extremely small time-step. To allow larger steps, one can recast the model in an implicit fashion by evaluating the second-derivative model in Eq. (8.114) at the *next* time-step:

$$\frac{u_n^{j+1} - u_n^j}{\Delta t} \approx \nu \frac{u_{n+1}^{j+1} - 2u_n^{j+1} + u_{n-1}^{j+1}}{\Delta y^2}$$

This rearrangement is unconditionally stable for any σ , but now we have *three* unknowns:

$$-\sigma u_{n-1}^{j+1} + (1 + 2\sigma)u_n^{j+1} - \sigma u_{n+1}^{j+1} \approx u_n^j \quad (8.117)$$

This is an *implicit* model, meaning that one must solve a large system of algebraic equations for the new nodal values at time $j + 1$. Fortunately, the system is narrowly banded, with the unknowns confined to the principal diagonal and its two nearest diagonals. In other words, the coefficient matrix of Eq. (8.117) is *tridiagonal*, a happy event. A direct method, called the *tridiagonal matrix algorithm* (TDMA), is available and explained in most CFD texts [20, 23 to 27]. Appendix A of Ref. 20 includes a complete program for solving the TDMA. If you have not learned the TDMA yet, Eq. (8.117) converges satisfactorily by rearrangement and iteration:

$$u_n^{j+1} \approx \frac{u_n^j + \sigma (u_{n-1}^{j+1} + u_{n+1}^{j+1})}{1 + 2\sigma} \quad (8.118)$$

At each time-step $j + 1$, sweep the nodes $2 \leq n \leq N - 1$ over and over, using Eq. (8.118), until the nodal values have converged. This implicit method is stable for any σ , however large. To ensure accuracy, though, one should keep Δt and Δy small compared to the basic time and length scales of the problem. This author’s habit is to keep Δt and Δy small enough that nodal values change no more than 10 percent from one (n, j) to the next.

EXAMPLE 8.7

SAE 30 oil at 20°C is at rest near a wall when the wall suddenly begins moving at a constant 1 m/s. Using the explicit model of Eq. (8.114), estimate the oil velocity at $y = 3$ cm after 1 second of wall motion.

[†]Finite differences are not analytical; one must set U_0 and ω equal to numerical values.

Solution

For SAE 30 oil, from Table A-3, $\nu = 0.29/891 = 3.25 \text{ E-4 m}^2/\text{s}$. For convenience in putting a node exactly at $y = 3 \text{ cm}$, choose $\Delta y = 0.01 \text{ m}$. The stability limit (8.116) is $\nu\Delta t/\Delta y^2 < 0.5$, or $\Delta t < 0.154 \text{ s}$. Again for convenience, to hit $t = 1 \text{ s}$ on the nose, choose $\Delta t = 0.1 \text{ s}$, or $\sigma = 0.3255$ and $(1 - 2\sigma) = 0.3491$. Then our explicit algebraic model (8.115) for this problem is

$$u_n^{j+1} \approx 0.3491 u_n^j + 0.3255(u_{n-1}^j + u_{n+1}^j) \quad (1)$$

We apply this relation from $n = 2$ out to at least $n = N = 15$, to make sure that the desired value of u at $n = 3$ is accurate. The wall no-slip boundary requires $u_1^j = 1.0 \text{ m/s} = \text{constant}$ for all j . The outer boundary condition is $u_N = 0$. The initial conditions are $u_n^1 = 0$ for $n \geq 2$. We then apply Eq. (1) repeatedly for $n \geq 2$ until we reach $j = 11$, which corresponds to $t = 1 \text{ s}$. This is easily programmed on a spreadsheet such as Excel. Here we print out only $j = 1, 6$, and 11 as follows:

j	t	u_1	u_2	u_3	u_4	u_5	u_6	u_7	u_8	u_9	u_{10}	u_{11}
1	0.000	1.000	0.000	0.000	0.000	0.000	0.000	0.000	0.000	0.000	0.000	0.000
6	0.500	1.000	0.601	0.290	0.107	0.027	0.004	0.000	0.000	0.000	0.000	0.000
11	1.000	1.000	0.704	0.446	0.250	0.123	0.052	0.018	0.005	0.001	0.000	0.000

Note: Units for t and u 's are s and m/s, respectively.

Our numerical estimate is $u_4^{11} = u(3 \text{ cm}, 1 \text{ s}) \approx 0.250 \text{ m/s}$, which is about 4 percent high—this problem has a known exact solution, $u = 0.241 \text{ m/s}$ [15]. We could improve the accuracy indefinitely by decreasing Δy and Δt .

Steady Two-Dimensional Laminar Flow

The previous example, unsteady one-dimensional flow, had only one viscous term and no convective accelerations. Let us look briefly at incompressible two-dimensional steady flow, which has four of each type of term, plus a nontrivial continuity equation:

$$\text{Continuity:} \quad \frac{\partial u}{\partial x} + \frac{\partial v}{\partial y} = 0 \quad (8.119a)$$

$$x \text{ momentum:} \quad u \frac{\partial u}{\partial x} + v \frac{\partial u}{\partial y} = -\frac{1}{\rho} \frac{\partial p}{\partial x} + \nu \left(\frac{\partial^2 u}{\partial x^2} + \frac{\partial^2 u}{\partial y^2} \right) \quad (8.119b)$$

$$y \text{ momentum} \quad u \frac{\partial v}{\partial x} + v \frac{\partial v}{\partial y} = -\frac{1}{\rho} \frac{\partial p}{\partial y} + \nu \left(\frac{\partial^2 v}{\partial x^2} + \frac{\partial^2 v}{\partial y^2} \right) \quad (8.119c)$$

These equations, to be solved for (u, v, p) as functions of (x, y) , are familiar to us from analytical solutions in Chaps. 4 and 6. However, to a numerical analyst, they are odd, because there is no *pressure equation*, that is, a differential equation for which the dominant derivatives involve p . This situation has led to several different “pressure-adjustment” schemes in the literature [20, 23 to 27], most of which manipulate the continuity equation to insert a pressure correction.

A second difficulty in Eq. (8.119b and c) is the presence of nonlinear convective accelerations such as $u(\partial u/\partial x)$, which create asymmetry in viscous flows. Early at-

tempts, which modeled such terms with a central difference, led to numerical instability. The remedy is to relate convection finite differences solely to the *upwind* flow entering the cell, ignoring the downwind cell. For example, the derivative $\partial u/\partial x$ could be modeled, for a given cell, as $(u_{\text{upwind}} - u_{\text{cell}})/\Delta x$. Such improvements have made fully viscous CFD an effective tool, with various commercial user-friendly codes available. For details beyond our scope, see Refs. 20 and 23 to 27.

Mesh generation and gridding have also become quite refined in modern CFD. Figure 8.36 illustrates a CFD solution of two-dimensional flow past an NACA 66(MOD) hydrofoil [28]. The gridding in Fig. 8.36a is of the C type, which wraps around the leading edge and trails off behind the foil, thus capturing the important near-wall and wake details without wasting nodes in front or to the sides. The grid size is 262 by 91.

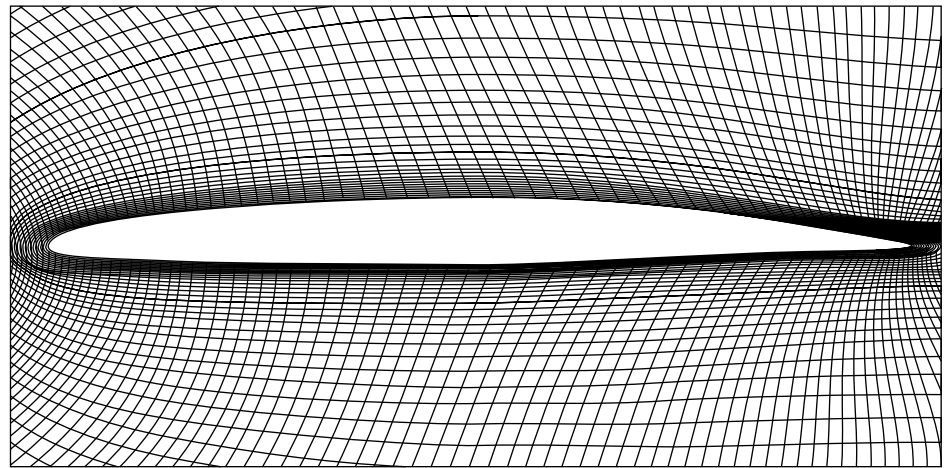
The CFD model for this hydrofoil flow is also quite sophisticated: a full Navier-Stokes solver with turbulence modeling [29] and allowance for cavitation bubble formation when surface pressures drop below the local vapor pressure. Figure 8.36b compares computed and experimental surface pressure coefficients for an angle of attack of 1° . The dimensionless pressure coefficient is defined as $C_p = (p_{\text{surface}} - p_\infty)/(\rho V_\infty^2/2)$. The agreement is excellent, as indeed it is also for cases where the hydrofoil cavitates [28]. Clearly, when properly implemented for the proper flow cases, CFD can be an extremely effective tool for engineers.

Commercial CFD Codes

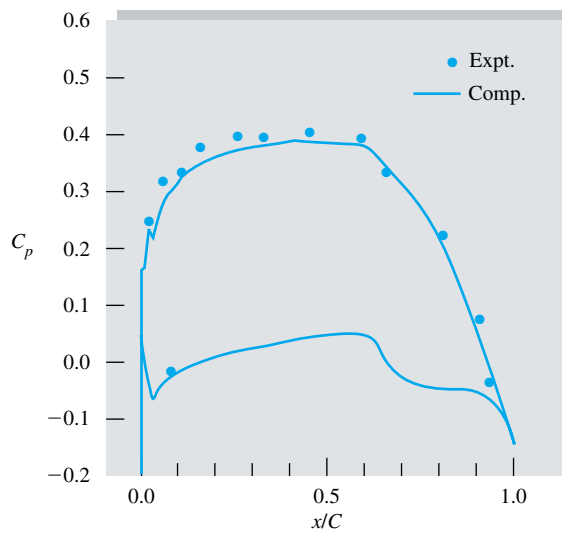
The coming of the third millennium has seen an enormous emphasis on computer applications in nearly every field, fluid mechanics being a prime example. It is now possible, at least for moderately complex geometries and flow patterns, to model on a digital computer, approximately, the equations of motion of fluid flow, with dedicated CFD textbooks available [20, 23 to 27]. The flow region is broken into a fine grid of elements and nodes, which algebraically simulate the basic partial differential equations of flow. While simple two-dimensional flow simulations have long been reported and can be programmed as student exercises, three-dimensional flows, involving thousands or even millions of grid points, are now solvable with the modern supercomputer.

Although elementary computer modeling was treated briefly here, the general topic of CFD is essentially for advanced study or professional practice. The big change over the past decade is that engineers, rather than laboriously programming CFD problems themselves, can now take advantage of any of several commercial CFD codes. These are extensive software packages which allow engineers to construct a geometry and boundary conditions to simulate a given viscous-flow problem. The software then grids the flow region and attempts to compute flow properties at each grid element. The convenience is great; the danger is also great. That is, computations are not merely automatic, like when using a hand calculator, but rather require care and concern from the user. Convergence and accuracy are real problems for the modeler. Use of the codes requires some art and experience. In particular, when the flow Reynolds number, $Re = \rho VL/\mu$, goes from moderate (laminar flow) to high (turbulent flow), the accuracy of the simulation is no longer assured in any real sense. The reason is that turbulent flows are not completely resolved by the full equations of motion, and one resorts to using approximate turbulence models.

Turbulence models [29] are developed for particular geometries and flow conditions and may be inaccurate or unrealistic for others. This is discussed by Freitas [30], who



(a)

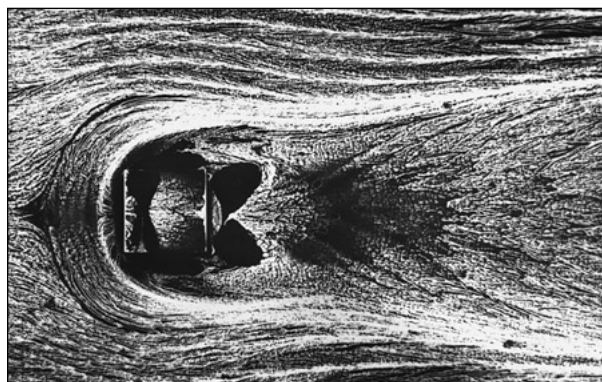


(b)

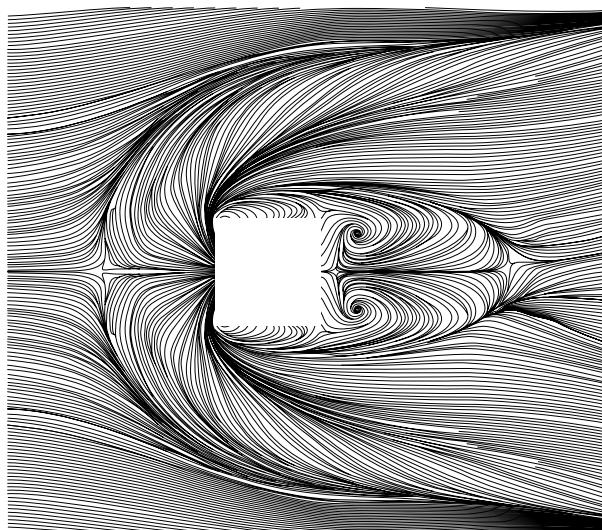
Fig. 8.36 CFD results for water flow past an NASA 66(MOD) hydrofoil [from Ref 28, with permission of the American Society of Mechanical Engineers]: (a) C gridting, 262 by 91 nodes; (b) surface pressures at $\alpha = 1^\circ$.

compared eight different commercial-code calculations (FLOW-3D, FLOTRAN, STAR-CD, N3S, CFD-ACE, FLUENT, CFDS-FLOW3D, and NISA/3D-FLUID) with experimental results for five benchmark flow experiments. Calculations were made by the vendors themselves. Freitas concludes that commercial codes, though promising in general, can be inaccurate for certain laminar- and turbulent-flow situations. Further research is recommended before engineers can truly rely upon such software to give generally accurate fluid-flow predictions.

In spite of the above warning to treat CFD codes with care, one should also realize that the results of a given CFD simulation can be spectacular. Figure 8.37 illustrates turbulent flow past a cube mounted on the floor of a channel whose clearance is twice



(a)



(b)



(c)

Fig. 8.37 Flow over a surface-mounted cube creates a complex and perhaps unexpected pattern: (a) experimental oil-streak visualization of surface flow at $Re = 40,000$ (based on cube height) (from Ref. 31, courtesy of Robert Martinuzzi, with the permission of the American Society of Mechanical Engineers); (b) computational large-eddy simulation of the surface flow in (a) (from Ref. 32, courtesy of Kishan Shah, Stanford University); and (c) a side view of the flow in (a) visualized by smoke generation and a laser light sheet (from Ref. 31, courtesy of Robert Martinuzzi, with the permission of the American Society of Mechanical Engineers).

the cube height. Compare Fig. 8.37*a*, a top view of the experimental surface flow [31] as visualized by oil streaks, with Fig. 8.37*b*, a CFD supercomputer result using the method of large-eddy simulation [32, 33]. The agreement is remarkable. The C-shaped flow pattern in front of the cube is caused by formation of a horseshoe vortex, as seen in a side view of the experiment [31] in Fig. 8.37*c*. Horseshoe vortices commonly result when surface shear flows meet an obstacle. We conclude that CFD has a tremendous potential for flow prediction.

Summary

This chapter has analyzed a highly idealized but very useful type of flow: inviscid, incompressible, irrotational flow, for which Laplace's equation holds for the velocity potential (8.1) and for the plane stream function (8.7). The mathematics is well developed, and solutions of potential flows can be obtained for practically any body shape.

Some solution techniques outlined here are (1) superposition of elementary line or point solutions in both plane and axisymmetric flow, (2) the analytic functions of a complex variable, (3) use of variable-strength vortex sheets, and (4) numerical analysis on a digital computer. Potential theory is especially useful and accurate for thin bodies such as airfoils. The only requirement is that the boundary layer be thin, i.e., that the Reynolds number be large.

For blunt bodies or highly divergent flows, potential theory serves as a first approximation, to be used as input to a boundary-layer analysis. The reader should consult the advanced texts [for example, 2 to 4, 10 to 13] for further applications of potential theory. Section 8.9 discusses computational methods for viscous (nonpotential) flows.

Problems

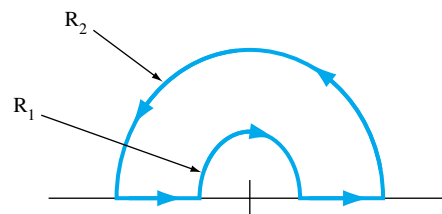
Most of the problems herein are fairly straightforward. More difficult or open-ended assignments are labeled with an asterisk. Problems labeled with an EES icon will benefit from the use of the Engineering Equation Solver (EES), while problems labeled with a computer disk may require the use of a computer. The standard end-of-chapter problems 8.1 to 8.115 (categorized in the problem list below) are followed by word problems W8.1 to W8.7, comprehensive problems C8.1 to C8.3, and design projects D8.1 to D8.3.

Problem Distribution

Section	Topic	Problems
8.1	Introduction and review	8.1–8.7
8.2	Elementary plane-flow solutions	8.8–8.17
8.3	Superposition of plane flows	8.18–8.34
8.4	Plane flow past closed-body shapes	8.35–8.59
8.5	The complex potential	8.60–8.71
8.6	Images	8.72–8.79
8.7	Airfoil theory: Two-dimensional	8.80–8.84
8.7	Airfoil theory: Finite-span wings	8.85–8.90
8.8	Axisymmetric potential flow	8.91–8.103
8.8	Hydrodynamic mass	8.104–8.105
8.9	Numerical methods	8.106–8.115

P8.1 Prove that the streamlines $\psi(r, \theta)$ in polar coordinates from Eqs. (8.10) are orthogonal to the potential lines $\phi(r, \theta)$.

P8.2 The steady plane flow in Fig. P8.2 has the polar velocity components $v_\theta = \Omega r$ and $v_r = 0$. Determine the circulation Γ around the path shown.



P8.2

P8.3 Using cartesian coordinates, show that each velocity component (u, v, w) of a potential flow satisfies Laplace's equation separately.

P8.4 Is the function $1/r$ a legitimate velocity potential in plane polar coordinates? If so, what is the associated stream function $\psi(r, \theta)$?

P8.5 Consider the two-dimensional velocity distribution $u = -By, v = Bx$, where B is a constant. If this flow possesses a

stream function, find its form. If it has a velocity potential, find that also. Compute the local angular velocity of the flow, if any, and describe what the flow might represent.

P8.6 An incompressible flow has the velocity potential $\phi = 2Bxy$, where B is a constant. Find the stream function of this flow, sketch a few streamlines, and interpret the pattern.

P8.7 Consider a flow with constant density and viscosity. If the flow possesses a velocity potential as defined by Eq. (8.1), show that it exactly satisfies the full Navier-Stokes equations (4.38). If this is so, why for inviscid theory do we back away from the full Navier-Stokes equations?

P8.8 For the velocity distribution of Prob. 8.5, evaluate the circulation Γ around the rectangular closed curve defined by $(x, y) = (1, 1), (3, 1), (3, 2),$ and $(1, 2)$. Interpret your result, especially vis-à-vis the velocity potential.

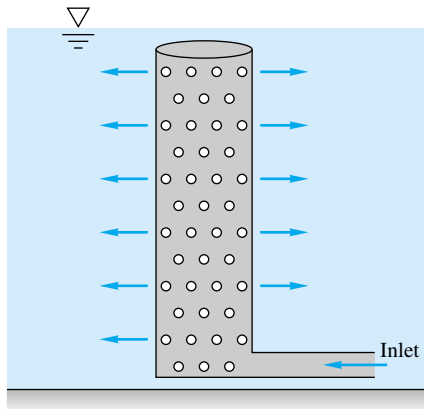
P8.9 Consider the two-dimensional flow $u = -Ax, v = Ay$, where A is a constant. Evaluate the circulation Γ around the rectangular closed curve defined by $(x, y) = (1, 1), (4, 1), (4, 3),$ and $(1, 3)$. Interpret your result, especially vis-à-vis the velocity potential.

P8.10 A mathematical relation sometimes used in fluid mechanics is the theorem of Stokes [1]

$$\oint_C \mathbf{V} \cdot d\mathbf{s} = \int_A (\nabla \times \mathbf{V}) \cdot \mathbf{n} dA$$

where A is any surface and C is the curve enclosing that surface. The vector $d\mathbf{s}$ is the differential arc length along C , and \mathbf{n} is the unit outward normal vector to A . How does this relation simplify for irrotational flow, and how does the resulting line integral relate to velocity potential?

P8.11 A power plant discharges cooling water through the manifold in Fig. P8.11, which is 55 cm in diameter and 8 m high and is perforated with 25,000 holes 1 cm in diameter. Does this manifold simulate a line source? If so, what is the equivalent source strength m ?



P8.11

P8.12 Consider the flow due to a vortex of strength K at the origin. Evaluate the circulation from Eq. (8.15) about the clockwise path from $(r, \theta) = (a, 0)$ to $(2a, 0)$ to $(2a, 3\pi/2)$ to $(a, 3\pi/2)$ and back to $(a, 0)$. Interpret the result.

P8.13 A well-known exact solution to the Navier-Stokes equations (4.38) is the unsteady circulating motion [15]

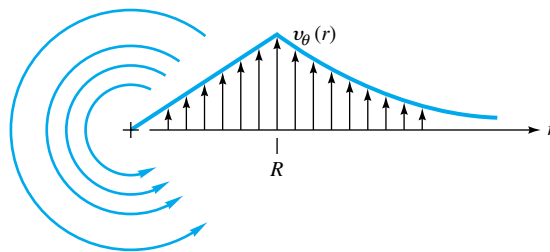
$$v_\theta = \frac{K}{2\pi r} \left[1 - \exp\left(-\frac{r^2}{4\nu t}\right) \right] \quad v_r = v_z = 0$$

where K is a constant and ν is the kinematic viscosity. Does this flow have a polar-coordinate stream function and/or velocity potential? Explain. Evaluate the circulation Γ for this motion, plot it versus r for a given finite time, and interpret compared to ordinary line vortex motion.

P8.14 A tornado may be modeled as the circulating flow shown in Fig. P8.14, with $v_r = v_z = 0$ and $v_\theta(r)$ such that

$$v_\theta = \begin{cases} \omega r & r \leq R \\ \frac{\omega R^2}{r} & r > R \end{cases}$$

Determine whether this flow pattern is irrotational in either the inner or outer region. Using the r -momentum equation (D.5) of App. D, determine the pressure distribution $p(r)$ in the tornado, assuming $p = p_\infty$ as $r \rightarrow \infty$. Find the location and magnitude of the lowest pressure.



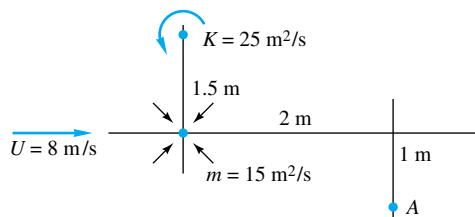
P8.14

P8.15 Evaluate Prob. 8.14 for the particular case of a small-scale tornado, $R = 100$ m, $v_{\theta, \max} = 65$ m/s, with sea-level conditions at $r = \infty$. Plot $p(r)$ out to $r = 400$ m.

P8.16 Consider inviscid stagnation flow, $\psi = Kxy$ (see Fig. 8.15b) superimposed with a source at the origin of strength m . Plot the resulting streamlines in the upper half plane, using the length scale $a = (m/K)^{1/2}$. Give a physical interpretation of the flow pattern.

P8.17 Examine the flow of Fig. 8.30 as an analytical (not a numerical) problem. Give the appropriate differential equation and the complete boundary conditions for both the stream function and the velocity potential. Is a Fourier-series solution possible?

- P8.18** Plot the streamlines and potential lines of the flow due to a line source of strength m at $(a, 0)$ plus a source $3m$ at $(-a, 0)$. What is the flow pattern viewed from afar?
- P8.19** Plot the streamlines and potential lines of the flow due to a line source of strength $3m$ at $(a, 0)$ plus a sink $-m$ at $(-a, 0)$. What is the pattern viewed from afar?
- P8.20** Plot the streamlines of the flow due to a line vortex $+K$ at $(0, +a)$ and a vortex $-K$ at $(0, -a)$. What is the pattern viewed from afar?
- P8.21** Plot the streamlines of the flow due to a line vortex $+K$ at $(+a, 0)$ and a vortex $-2K$ at $(-a, 0)$. What is the pattern viewed from afar?
- P8.22** Plot the streamlines of a uniform stream $\mathbf{V} = iU$ plus a clockwise line vortex $-K$ located at the origin. Are there any stagnation points?
- P8.23** Find the resultant velocity vector induced at point A in Fig. P8.23 by the uniform stream, vortex, and line source.



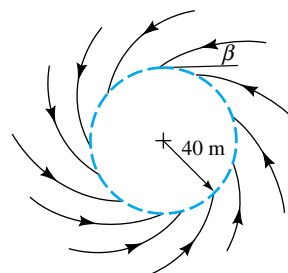
P8.23

- P8.24** Line sources of equal strength $m = Ua$, where U is a reference velocity, are placed at $(x, y) = (0, a)$ and $(0, -a)$. Sketch the stream and potential lines in the upper half plane. Is $y = 0$ a “wall”? If so, sketch the pressure coefficient

$$C_p = \frac{p - p_0}{\frac{1}{2}\rho U^2}$$

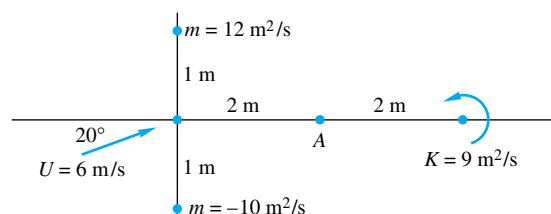
along the wall, where p_0 is the pressure at $(0, 0)$. Find the minimum pressure point and indicate where flow separation might occur in the boundary layer.

- P8.25** Let the vortex/sink flow of Eq. (4.134) simulate a tornado as in Fig. P8.25. Suppose that the circulation about the tornado is $\Gamma = 8500 \text{ m}^2/\text{s}$ and that the pressure at $r = 40 \text{ m}$ is 2200 Pa less than the far-field pressure. Assuming inviscid flow at sea-level density, estimate (a) the appropriate sink strength $-m$, (b) the pressure at $r = 15 \text{ m}$, and (c) the angle β at which the streamlines cross the circle at $r = 40 \text{ m}$ (see Fig. P8.25).



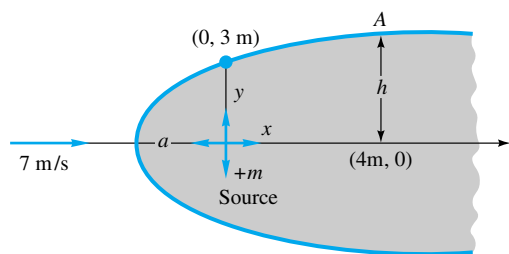
P8.25

- P8.26** Find the resultant velocity vector induced at point A in Fig. P8.26 by the uniform stream, line source, line sink, and vortex.



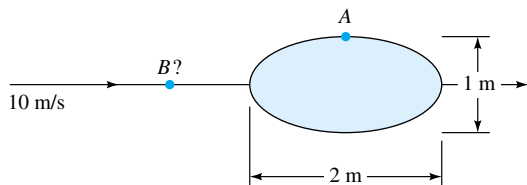
P8.26

- P8.27** A counterclockwise line vortex of strength $3K$ at $(x, y) = (0, a)$ is combined with a clockwise vortex K at $(0, -a)$. Plot the streamline and potential-line pattern, and find the point of minimum velocity between the two vortices.
- P8.28** Sources of equal strength m are placed at the four symmetric positions $(x, y) = (a, a)$, $(-a, a)$, $(-a, -a)$, and $(a, -a)$. Sketch the streamline and potential-line patterns. Do any plane “walls” appear?
- P8.29** A uniform water stream, $U_\infty = 20 \text{ m/s}$ and $\rho = 998 \text{ kg/m}^3$, combines with a source at the origin to form a half-body. At $(x, y) = (0, 1.2 \text{ m})$, the pressure is 12.5 kPa less than p_∞ . (a) Is this point outside the body? Estimate (b) the appropriate source strength m and (c) the pressure at the nose of the body.
- P8.30** Suppose that the total discharge from the manifold in Fig. P8.11 is $450 \text{ m}^3/\text{s}$ and that there is a uniform ocean current of 60 cm/s to the right. Sketch the flow pattern from above, showing the dimensions and the region where the cooling-water discharge is confined.
- P8.31** A Rankine half-body is formed as shown in Fig. P8.31. For the stream velocity and body dimension shown, compute (a) the source strength m in m^2/s , (b) the distance a , (c) the distance h , and (d) the total velocity at point A.



P8.31

- P8.32** Sketch the streamlines, especially the body shape, due to equal line sources $+m$ at $(-a, 0)$ and $(+a, 0)$ plus a uniform stream $U_\infty = ma$.
- P8.33** Sketch the streamlines, especially the body shape, due to equal line sources $+m$ at $(0, +a)$ and $(0, -a)$ plus a uniform stream $U_\infty = ma$.
- P8.34** Consider three equally spaced sources of strength m placed at $(x, y) = (0, +a)$, $(0, 0)$, and $(0, -a)$. Sketch the resulting streamlines, noting the position of any stagnation points. What would the pattern look like from afar?
- P8.35** Consider three equal sources m in a triangular configuration: one at $(a/2, 0)$, one at $(-a/2, 0)$, and one at $(0, a)$. Plot the streamlines for this flow. Are there any stagnation points? *Hint:* Try the MATLAB contour command [34].
- P8.36** When a line source-sink pair with $m = 2 \text{ m}^2/\text{s}$ is combined with a uniform stream, it forms a Rankine oval whose minimum dimension is 40 cm. If $a = 15 \text{ cm}$, what are the stream velocity and the velocity at the shoulder? What is the maximum dimension?
- P8.37** A Rankine oval 2 m long and 1 m high is immersed in a stream $U_\infty = 10 \text{ m/s}$, as in Fig. P8.37. Estimate (a) the velocity at point A and (b) the location of point B where a particle approaching the stagnation point achieves its maximum deceleration.



P8.37

- P8.38** A uniform stream U in the x direction combines with a source m at $(a, 0)$ and a sink $-m$ at $(-a, 0)$. Plot the resulting streamlines and note any stagnation points.
- P8.39** Sketch the streamlines of a uniform stream U_∞ past a line source-sink pair aligned vertically with the source at $+a$ and the sink at $-a$ on the y -axis. Does a closed-body shape form?

P8.40 Consider a uniform stream U_∞ plus line sources $+m$ at $(x, y) = (+a, 0)$ and $(-a, 0)$ and a single line sink $-2m$ at the origin. Does a closed-body shape appear? If so, plot its shape for $m/(U_\infty a)$ equal to (a) 1.0 and (b) 5.0.

P8.41 A Kelvin oval is formed by a line-vortex pair with $K = 9 \text{ m}^2/\text{s}$, $a = 1 \text{ m}$, and $U = 10 \text{ m/s}$. What are the height, width, and shoulder velocity of this oval?

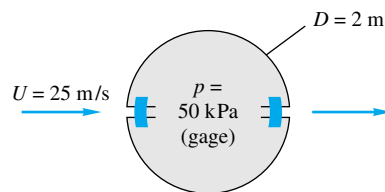
P8.42 For what value of $K/(U_\infty a)$ does the velocity at the shoulder of a Kelvin oval equal $4U_\infty$? What is the height h/a of this oval?

P8.43 Consider water at 20°C flowing at 6 m/s past a 1-m-diameter circular cylinder. What doublet strength λ in m^3/s is required to simulate this flow? If the stream pressure is 200 kPa, use inviscid theory to estimate the surface pressure at θ equal to (a) 180° , (b) 135° , and (c) 90° .

P8.44 Suppose that circulation is added to the cylinder flow of Prob. 8.43 sufficient to place the stagnation points at θ equal to 50° and 130° . What is the required vortex strength K in m^2/s ? Compute the resulting pressure and surface velocity at (a) the stagnation points and (b) the upper and lower shoulders. What will the lift per meter of cylinder width be?

P8.45 What circulation K must be added to the cylinder flow in Prob. 8.43 to place the stagnation point exactly at the upper shoulder? What will the velocity and pressure at the lower shoulder be then? What value of K causes the lower shoulder pressure to be 10 kPa?

P8.46 A cylinder is formed by bolting two semicylindrical channels together on the inside, as shown in Fig. P8.46. There are 10 bolts per meter of width on each side, and the inside pressure is 50 kPa (gage). Using potential theory for the outside pressure, compute the tension force in each bolt if the fluid outside is sea-level air.

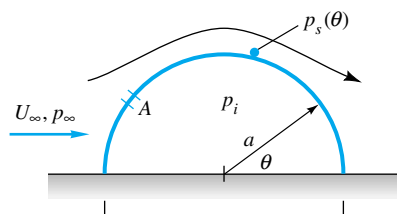


P8.46

P8.47 A circular cylinder is fitted with two surface-mounted pressure sensors, to measure p_a at $\theta = 180^\circ$ and p_b at $\theta = 105^\circ$. The intention is to use the cylinder as a stream velocimeter. Using inviscid theory, derive a formula for estimating U_∞ in terms of p_a , p_b , ρ , and the cylinder radius a .

***P8.48** Wind at U_∞ and p_∞ flows past a Quonset hut which is a half-cylinder of radius a and length L (Fig. P8.48). The internal pressure is p_i . Using inviscid theory, derive an ex-

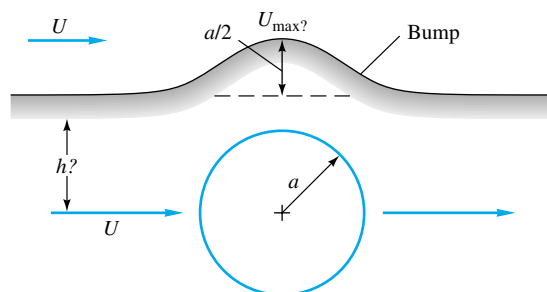
pression for the upward force on the hut due to the difference between p_i and p_s .



P8.48

P8.49 In strong winds the force in Prob. 8.48 can be quite large. Suppose that a hole is introduced in the hut roof at point A to make p_i equal to the surface pressure there. At what angle θ should hole A be placed to make the net wind force zero?

P8.50 It is desired to simulate flow past a two-dimensional ridge or bump by using a streamline which passes above the flow over a cylinder, as in Fig. P8.50. The bump is to be $a/2$ high, where a is the cylinder radius. What is the elevation h of this streamline? What is U_{\max} on the bump compared with stream velocity U ?



P8.50

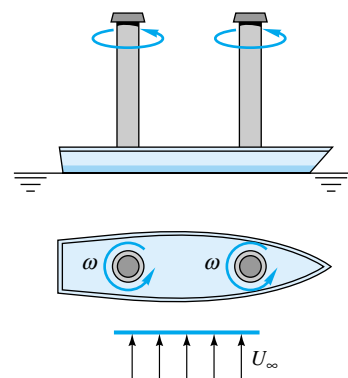
P8.51 Modify Prob. 8.50 as follows. Let the bump be such that $U_{\max} = 1.5U$. Find (a) the upstream elevation h and (b) the height of the bump.

P8.52 The Flettner rotor sailboat in Fig. E8.2 has a water drag coefficient of 0.006 based on a wetted area of 45 ft². If the rotor spins at 220 r/min, find the maximum boat velocity that can be achieved in a 15-mi/h wind. What is the optimum angle between the boat and the wind?

P8.53 Modify Prob. 8.52 as follows. For the same sailboat data, find the wind velocity, in mi/h, which will drive the boat at an optimum speed of 10 kn parallel to its keel.

P8.54 The original Flettner rotor ship was approximately 100 ft long, displaced 800 tons, and had a wetted area of 3500

ft². As sketched in Fig. P8.54, it had two rotors 50 ft high and 9 ft in diameter rotating at 750 r/min, which is far outside the range of Fig. 8.11. The measured lift and drag coefficients for each rotor were about 10 and 4, respectively. If the ship is moored and subjected to a crosswind of 25 ft/s, as in Fig. P8.54, what will the wind force parallel and normal to the ship centerline be? Estimate the power required to drive the rotors.



P8.54

P8.55 Assume that the Flettner rotorship of Fig. P8.54 has a water resistance coefficient of 0.005. How fast will the ship sail in seawater at 20°C in a 20-ft/s wind if the keel aligns itself with the resultant force on the rotors? *Hint:* This is a problem in relative velocities.

P8.56 The measured drag coefficient of a cylinder in crossflow, based on frontal area DL , is approximately 1.0 for the laminar-boundary-layer range (see Fig. 7.16a). Boundary-layer separation occurs near the shoulder (see Fig. 7.13a). This suggests an analytical model: the standard inviscid-flow solution on the front of the cylinder and constant pressure (equal to the shoulder value) on the rear. Use this model to predict the drag coefficient and comment on the results with reference to Fig. 7.13c.

P8.57 In principle, it is possible to use rotating cylinders as aircraft wings. Consider a cylinder 30 cm in diameter, rotating at 2400 r/min. It is to lift a 55-kN airplane cruising at 100 m/s. What should the cylinder length be? How much power is required to maintain this speed? Neglect end effects on the rotating wing.

P8.58 Plot the streamlines due to the combined flow of a line sink $-m$ at the origin plus line sources $+m$ at $(a, 0)$ and $(4a, 0)$. *Hint:* A cylinder of radius $2a$ will appear.

P8.59 By analogy with Prob. 8.58 plot the streamlines due to counterclockwise line vortices $+K$ at $(0, 0)$ and $(4a, 0)$ plus a clockwise vortex $-K$ at $(a, 0)$. Again a cylinder appears.

P8.60 One of the corner-flow patterns of Fig. 8.15 is given by the cartesian stream function $\psi = A(3yx^2 - y^3)$. Which one? Can the correspondence be proved from Eq. (8.49)?

P8.61 Plot the streamlines of Eq. (8.49) in the upper right quadrant for $n = 4$. How does the velocity increase with x outward along the x -axis from the origin? For what corner angle and value of n would this increase be linear in x ? For what corner angle and n would the increase be as x^5 ?

P8.62 Combine stagnation flow, Fig. 8.14*b*, with a source at the origin:

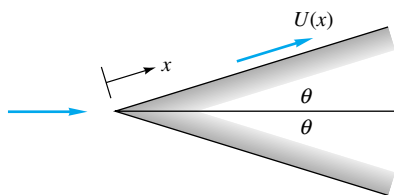
$$f(z) = Az^2 + m \ln z$$

Plot the streamlines for $m = AL^2$, where L is a length scale. Interpret.

P8.63 The superposition in Prob. 8.62 leads to stagnation flow near a curved bump, in contrast to the flat wall of Fig. 8.14*b*. Determine the maximum height H of the bump as a function of the constants A and m .

P8.64 Determine qualitatively from boundary-layer theory (Chap. 7) whether any of the three stagnation-flow patterns of Fig. 8.15 can suffer flow separation along the walls.

P8.65 Potential flow past a wedge of half-angle θ leads to an important application of laminar-boundary-layer theory called the *Falkner-Skan flows* [15, pp. 242–247]. Let x denote distance along the wedge wall, as in Fig. P8.65, and let $\theta = 10^\circ$. Use Eq. (8.49) to find the variation of surface velocity $U(x)$ along the wall. Is the pressure gradient adverse or favorable?



P8.65

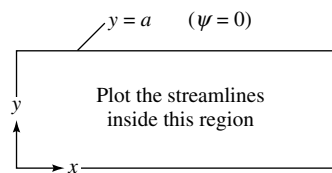
***P8.66** The inviscid velocity along the wedge in Prob. 8.65 has the analytic form $U(x) = Cx^m$, where $m = n - 1$ and n is the exponent in Eq. (8.49). Show that, for any C and n , computation of the boundary layer by Thwaites' method, Eqs. (7.53) and (7.54), leads to a unique value of the Thwaites parameter λ . Thus wedge flows are called *similar* [15, p. 244].

P8.67 Investigate the complex potential function $f(z) = U_\infty(z + a^2/z)$ and interpret the flow pattern.

P8.68 Investigate the complex potential function $f(z) = U_\infty z + m \ln [(z + a)/(z - a)]$ and interpret the flow pattern.

P8.69 Investigate the complex potential $f(z) = A \cosh [\pi(z/a)]$, and plot the streamlines inside the region shown in Fig.

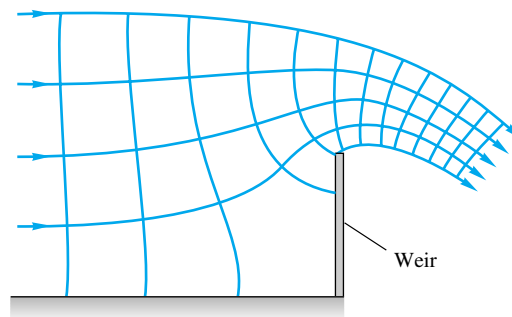
P8.69. What hyphenated word (originally French) might describe such a flow pattern?



P8.69

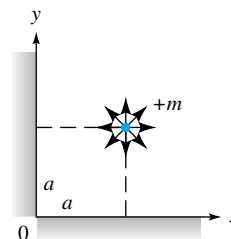
P8.70 Show that the complex potential $f = U_\infty \{z + \frac{1}{4}a \coth [\pi(z/a)]\}$ represents flow past an oval shape placed midway between two parallel walls $y = \pm \frac{1}{2}a$. What is a practical application?

P8.71 Figure P8.71 shows the streamlines and potential lines of flow over a thin-plate weir as computed by the complex potential method. Compare qualitatively with Fig. 10.16*a*. State the proper boundary conditions at all boundaries. The velocity potential has equally spaced values. Why do the flow-net "squares" become smaller in the overflow jet?



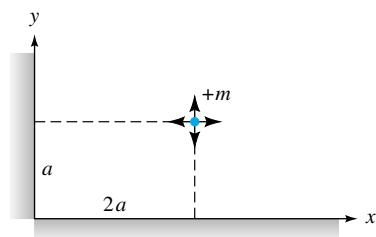
P8.71

P8.72 Use the method of images to construct the flow pattern for a source $+m$ near two walls, as shown in Fig. P8.72. Sketch the velocity distribution along the lower wall ($y = 0$). Is there any danger of flow separation along this wall?

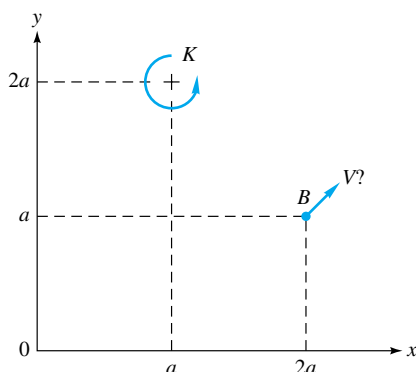


P8.72

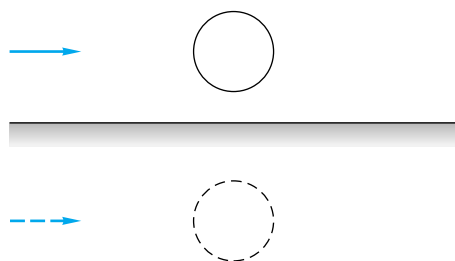
P8.73 Set up an image system to compute the flow of a source at unequal distances from two walls, as in Fig. P8.73. Find the point of maximum velocity on the y -axis.


P8.73

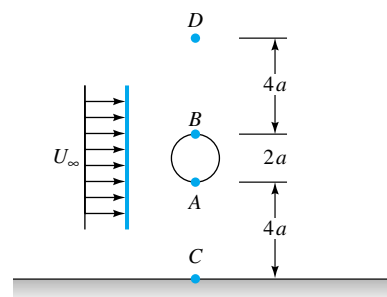
- P8.74** A positive line vortex K is trapped in a corner, as in Fig. P8.74. Compute the total induced velocity vector at point B , $(x, y) = (2a, a)$, and compare with the induced velocity when no walls are present.


P8.74

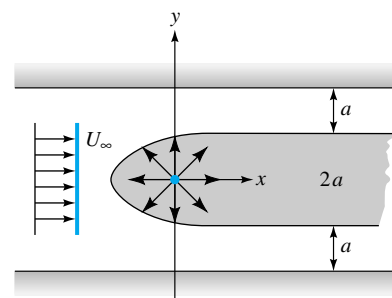
- P8.75** The flow past a cylinder very near a wall might be simulated by doublet images, as in Fig. P8.75. Explain why the result is not very successful and the cylinder shape becomes badly distorted.


P8.75

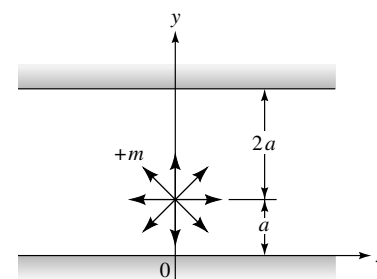
- P8.76** Use the method of images to approximate the flow pattern past a cylinder a distance $4a$ from a single wall, as in Fig. P8.76. To illustrate the effect of the wall, compute the velocities at corresponding points A , B and C , D , comparing with a cylinder flow in an infinite expanse of fluid.


P8.76

- P8.77** Discuss how the flow pattern of Prob. 8.58 might be interpreted to be an image-system construction for circular walls. Why are there two images instead of one?
- *P8.78** Indicate the system of images needed to construct the flow of a uniform stream past a Rankine half-body constrained between two parallel walls, as in Fig. P8.78. For the particular dimensions shown in this figure, estimate the position of the nose of the resulting half-body.


P8.78

- P8.79** Explain the system of images needed to simulate the flow of a line source placed unsymmetrically between two parallel walls as in Fig. P8.79. Compute the velocity on the lower wall at $x = a$. How many images are needed to estimate this velocity within 1 percent?


P8.79

***P8.80** The beautiful expression for lift of a two-dimensional airfoil, Eq. (8.69), arose from applying the Joukowski transformation, $\zeta = z + a^2/z$, where $z = x + iy$ and $\zeta = \eta + i\beta$. The constant a is a length scale. The theory transforms a certain circle in the z plane into an airfoil in the ζ plane. Taking $a = 1$ unit for convenience, show that (a) a circle with center at the origin and radius > 1 will become an ellipse in the ζ plane and (b) a circle with center at $x = -\epsilon \ll 1$, $y = 0$, and radius $(1 + \epsilon)$ will become an airfoil shape in the ζ plane. *Hint:* The Excel spreadsheet is excellent for solving this problem.

P8.81 A two-dimensional airfoil has 2 percent camber and 10 percent thickness. If $C = 1.75$ m, estimate its lift per meter when immersed in 20°C water at $\alpha = 6^\circ$ and $U = 18$ m/s.

P8.82 The ultralight plane *Gossamer Condor* in 1977 was the first to complete the Kremer Prize figure-eight course under human power. Its wingspan was 29 m, with $C_{av} = 2.3$ m and a total mass of 95 kg. The drag coefficient was approximately 0.05. The pilot was able to deliver $\frac{1}{4}$ hp to propel the plane. Assuming two-dimensional flow at sea level, estimate (a) the cruise speed attained, (b) the lift coefficient, and (c) the horsepower required to achieve a speed of 15 kn.

P8.83 Two-dimensional lift-drag data for the NACA 2412 airfoil with 2 percent camber (from Ref. 12) may be curve-fitted accurately as follows:

$$C_L \approx 0.178 + 0.109\alpha - 0.00109\alpha^2$$

$$C_D \approx 0.0089 + 1.97 \text{ E-4 } \alpha + 8.45 \text{ E-5 } \alpha^2$$

$$- 1.35 \text{ E-5 } \alpha^3 + 9.92 \text{ E-7 } \alpha^4$$

with α in degrees in the range $-4^\circ < \alpha < +10^\circ$. Compare (a) the lift-curve slope and (b) the angle of zero lift with theory, Eq. (8.69). (c) Prepare a polar lift-drag plot and compare with Fig. 7.26.

P8.84 Reference 12 contains inviscid-theory calculations for the upper and lower surface velocity distributions $V(x)$ over an airfoil, where x is the chordwise coordinate. A typical result for small angle of attack is as follows:

x/c	$V/U_\infty(\text{upper})$	$V/U_\infty(\text{lower})$
0.0	0.0	0.0
0.025	0.97	0.82
0.05	1.23	0.98
0.1	1.28	1.05
0.2	1.29	1.13
0.3	1.29	1.16
0.4	1.24	1.16
0.6	1.14	1.08
0.8	0.99	0.95
1.0	0.82	0.82

Use these data, plus Bernoulli's equation, to estimate (a) the lift coefficient and (b) the angle of attack if the airfoil is symmetric.

P8.85 A wing of 2 percent camber, 5-in chord, and 30-in span is tested at a certain angle of attack in a wind tunnel with sea-level standard air at 200 ft/s and is found to have lift of 30 lbf and drag of 1.5 lbf. Estimate from wing theory (a) the angle of attack, (b) the minimum drag of the wing and the angle of attack at which it occurs, and (c) the maximum lift-to-drag ratio.

P8.86 An airplane has a mass of 20,000 kg and flies at 175 m/s at 5000-m standard altitude. Its rectangular wing has a 3-m chord and a symmetric airfoil at 2.5° angle of attack. Estimate (a) the wing span, (b) the aspect ratio, and (c) the induced drag.

P8.87 A freshwater boat of mass 400 kg is supported by a rectangular hydrofoil of aspect ratio 8, 2 percent camber, and 12 percent thickness. If the boat travels at 8 m/s and $\alpha = 3.5^\circ$, estimate (a) the chord length, (b) the power required if $C_{D,\infty} = 0.01$, and (c) the top speed if the boat is refitted with an engine which delivers 50 hp to the water.

P8.88  The Boeing 727 airplane has a gross weight of 125,000 lbf, a wing area of 1200 ft², and an aspect ratio of 6. It is fitted with two turbofan engines and cruises at 532 mi/h at 30,000-ft standard altitude. Assume for this problem that its airfoil is the NACA 2412 section described in Prob. 8.83. If we neglect all drag except the wing, what thrust is required from each engine for these conditions?

P8.89 The Beechcraft T-34C aircraft has a gross weight of 5500 lbf and a wing area of 60 ft² and flies at 322 mi/h at 10,000-ft standard altitude. It is driven by a propeller which delivers 300 hp to the air. Assume for this problem that its airfoil is the NACA 2412 section described in Prob. 8.83, and neglect all drag except the wing. What is the appropriate aspect ratio for the wing?

P8.90 When moving at 15 m/s in seawater at its maximum lift-to-drag ratio of 18:1, a symmetric hydrofoil, of plan area 3 m², develops a lift of 120 kN. Estimate from wing theory (a) the aspect ratio and (b) the angle of attack in degrees.

P8.91 If $\phi(r, \theta)$ in axisymmetric flow is defined by Eq. (8.85) and the coordinates are given in Fig. 8.24, determine what partial differential equation is satisfied by ϕ .

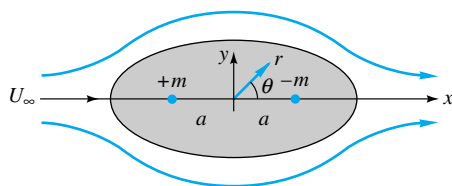
P8.92 A point source with volume flow $Q = 30$ m³/s is immersed in a uniform stream of speed 4 m/s. A Rankine half-body of revolution results. Compute (a) the distance from source to the stagnation point and (b) the two points (r, θ) on the body surface where the local velocity equals 4.5 m/s.

P8.93 The Rankine half-body of revolution (Fig. 8.26) could simulate the shape of a pitot-static tube (Fig. 6.30). Ac-

ording to inviscid theory, how far downstream from the nose should the static pressure holes be placed so that the local velocity is within ± 0.5 percent of U_∞ ? Compare your answer with the recommendation $x \approx 8D$ in Fig. 6.30.

P8.94 Determine whether the Stokes streamlines from Eq. (8.86) are everywhere orthogonal to the Stokes potential lines from Eq. (8.87), as is the case for cartesian and plane polar coordinates.

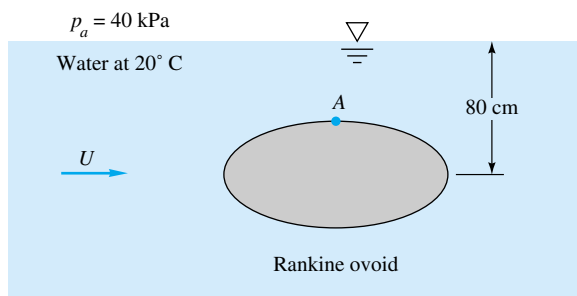
P8.95 Show that the axisymmetric potential flow formed by superposition of a point source $+m$ at $(x, y) = (-a, 0)$, a point sink $-m$ at $(+a, 0)$, and a stream U_∞ in the x direction forms a Rankine body of revolution as in Fig. P8.95. Find analytic expressions for determining the length $2L$ and maximum diameter $2R$ of the body in terms of m , U_∞ , and a .



P8.95

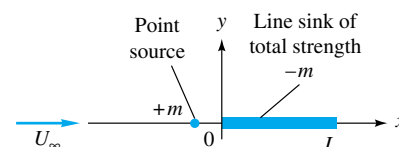
P8.96 Suppose that a sphere with a single stagnation hole is to be used as a velocimeter. The pressure at this hole is used to compute the stream velocity, but there are errors if the hole is not perfectly aligned with the oncoming stream. Using inviscid incompressible theory, plot the percent error in stream velocity estimate as a function of misalignment angle ϕ . At what angle is the error 10 percent?

P8.97 The Rankine body of revolution in Fig. P8.97 is 60 cm long and 30 cm in diameter. When it is immersed in the low-pressure water tunnel as shown, cavitation may appear at point A. Compute the stream velocity U , neglecting surface wave formation, for which cavitation occurs.



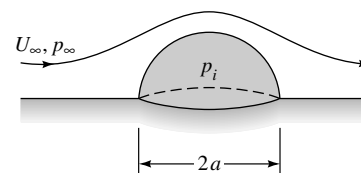
P8.97

P8.98 We have studied the point source (sink) and the line source (sink) of infinite depth into the paper. Does it make any sense to define a finite-length line sink (source) as in Fig. P8.98? If so, how would you establish the mathematical properties of such a finite line sink? When combined with a uniform stream and a point source of equivalent strength as in Fig. P8.98, should a closed-body shape be formed? Make a guess and sketch some of these possible shapes for various values of the dimensionless parameter $m/(U_\infty L^2)$.



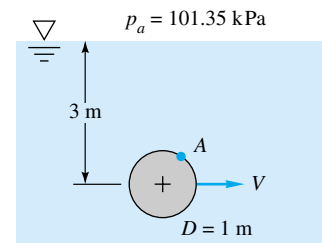
P8.98

***P8.99** Consider air flowing past a hemisphere resting on a flat surface, as in Fig. P8.99. If the internal pressure is p_i , find an expression for the pressure force on the hemisphere. By analogy with Prob. 8.49, at what point A on the hemisphere should a hole be cut so that the pressure force will be zero according to inviscid theory?



P8.99

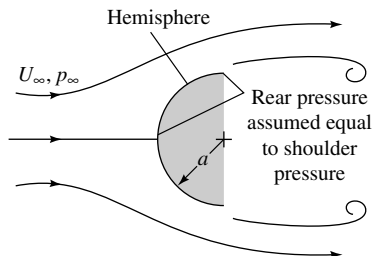
P8.100 A 1-m-diameter sphere is being towed at speed V in fresh water at 20°C as shown in Fig. P8.100. Assuming inviscid theory with an undistorted free surface, estimate the speed V in m/s at which cavitation will first appear on the sphere surface. Where will cavitation appear? For this condition, what will be the pressure at point A on the sphere which is 45° up from the direction of travel?



P8.100

P8.101 Normally by its very nature inviscid theory is incapable of predicting body drag, but by analogy with Fig. 8.16c we can analyze flow approaching a hemisphere, as in Fig.

P8.101. Assume that the flow on the front follows inviscid sphere theory, Eq. (8.96), and the pressure in the rear equals the shoulder pressure. Compute the drag coefficient and compare with experiment (Table 7.3). What are the defects and limitations of this analysis?

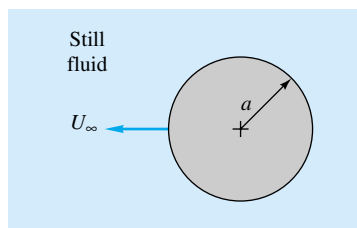


P8.101

P8.102 A golf ball weighs 0.102 lbf and has a diameter of 1.7 in. A professional golfer strikes the ball at an initial velocity of 250 ft/s, an upward angle of 20° , and a backspin (front of the ball rotating upward). Assume that the lift coefficient on the ball (based on frontal area) follows Fig. P7.108. If the ground is level and drag is neglected, make a simple analysis to predict the impact point (a) without spin and (b) with backspin of 7500 r/min.

P8.103  Modify Prob. 8.102 as follows. Golf balls are dimpled, not smooth, and have higher lift and lower drag ($C_L \approx 0.2$ and $C_D \approx 0.3$ for typical backspin). Using these values, make a computer analysis of the ball trajectory for the initial conditions of Prob. 8.102. If time permits, investigate the effect of initial angle for the range $10^\circ < \theta_0 < 50^\circ$.

P8.104 Consider a cylinder of radius a moving at speed U_∞ through a still fluid, as in Fig. P8.104. Plot the streamlines relative to the cylinder by modifying Eq. (8.32) to give the relative flow with $K = 0$. Integrate to find the total relative kinetic energy, and verify the hydrodynamic mass of a cylinder from Eq. (8.104).

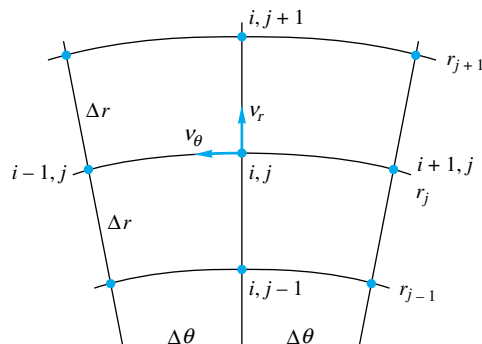


P8.104

*P8.105 In Table 7.2 the drag coefficient of a 4:1 elliptical cylinder in laminar-boundary-layer flow is 0.35. According to Patton [17], the hydrodynamic mass of this cylinder is $\pi\rho hb/4$, where b is width into the paper and h is the max-

imum thickness. Use these results to derive a formula from the time history $U(t)$ of the cylinder if it is accelerated from rest in a still fluid by the sudden application of a constant force F .

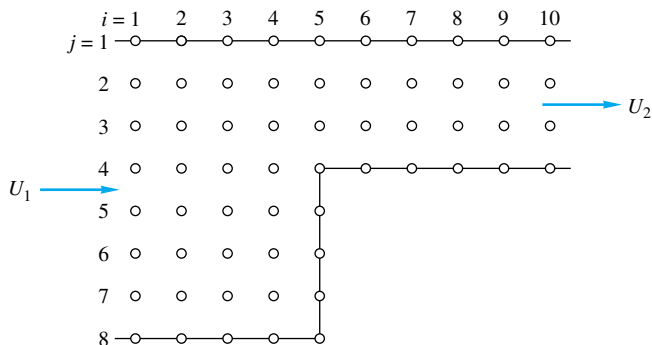
P8.106 Laplace's equation in plane polar coordinates, Eq. (8.11), is complicated by the variable radius. Consider the finite-difference mesh in Fig. P8.106, with nodes (i, j) equally spaced $\Delta\theta$ and Δr apart. Derive a finite-difference model for Eq. (8.11) similar to the cartesian expression (8.109).



P8.106

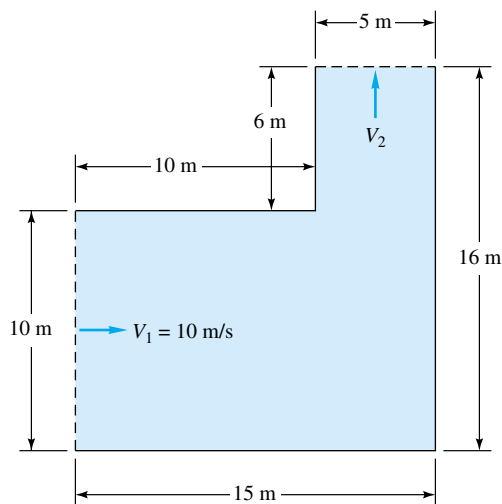
P8.107  Set up the numerical problem of Fig. 8.30 for an expansion of 30° . A new grid system and a nonsquare mesh may be needed. Give the proper nodal equation and boundary conditions. If possible, program this 30° expansion and solve on a digital computer.

P8.108  Consider two-dimensional potential flow into a step contraction as in Fig. P8.108. The inlet velocity $U_1 = 7$ m/s, and the outlet velocity U_2 is uniform. The nodes (i, j) are labeled in the figure. Set up the complete finite-difference algebraic relations for all nodes. Solve, if possible, on a digital computer and plot the streamlines in the flow.



P8.108

- P8.109** Consider inviscid flow through a two-dimensional 90° bend with a contraction, as in Fig. P8.109. Assume uniform flow at the entrance and exit. Make a finite-difference computer analysis for small grid size (at least 150 nodes), determine the dimensionless pressure distribution along the walls, and sketch the streamlines. (You may use either square or rectangular grids.)



P8.109

- P8.110** For fully developed laminar incompressible flow through a straight noncircular duct, as in Sec. 6.6, the Navier-Stokes equations (4.38) reduce to

$$\frac{\partial^2 u}{\partial y^2} + \frac{\partial^2 u}{\partial z^2} = \frac{1}{\mu} \frac{dp}{dx} = \text{const} < 0$$

where (y, z) is the plane of the duct cross section and x is along the duct-axis. Gravity is neglected. Using a non-square rectangular grid $(\Delta x, \Delta y)$, develop a finite-difference model for this equation, and indicate how it may be applied to solve for flow in a rectangular duct of side lengths a and b .

- P8.111** Solve Prob. 8.110 numerically for a rectangular duct of side length b by $2b$, using at least 100 nodal points. Evaluate the volume flow rate and the friction factor, and compare with the results in Table 6.4:

$$Q \approx 0.1143 \frac{b^4}{\mu} \left(-\frac{dp}{dx} \right) \quad f \text{Re}_{D_h} \approx 62.19$$

where $D_h = 4A/P = 4b/3$ for this case. Comment on the possible truncation errors of your model.

- P8.112** In his CFD textbook, Patankar [5] replaces the left-hand sides of Eq. (8.119*b* and *c*) with the following two expressions, respectively:

$$\frac{\partial}{\partial x}(u^2) + \frac{\partial}{\partial y}(vu) \quad \text{and} \quad \frac{\partial}{\partial x}(uv) + \frac{\partial}{\partial y}(v^2)$$

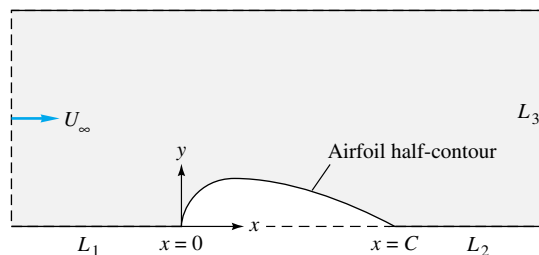
Are these equivalent expressions, or are they merely simplified approximations? Either way, why might these forms be better for finite-difference purposes?

- P8.113** Repeat Example 8.7 using the implicit method of Eq. (8.118). Take $\Delta t = 0.2$ s and $\Delta y = 0.01$ m, which ensures that an explicit model would diverge. Compare your accuracy with Example 8.7.

- P8.114** If your institution has an online potential-flow boundary-element computer code, consider flow past a symmetric airfoil, as in Fig. P8.114. The basic shape of an NACA symmetric airfoil is defined by the function [12]

$$\frac{2y}{t_{\max}} \approx 1.4845\zeta^{1/2} - 0.63\zeta - 1.758\zeta^2 + 1.4215\zeta^3 - 0.5075\zeta^4$$

where $\zeta = x/C$ and the maximum thickness t_{\max} occurs at $\zeta = 0.3$. Use this shape as part of the lower boundary for zero angle of attack. Let the thickness be fairly large, say, $t_{\max} = 0.12, 0.15,$ or 0.18 . Choose a generous number of nodes (≥ 60), and calculate and plot the velocity distribution V/U_∞ along the airfoil surface. Compare with the theoretical results in Ref. 12 for NACA 0012, 0015, or 0018 airfoils. If time permits, investigate the effect of the boundary lengths $L_1, L_2,$ and L_3 , which can initially be set equal to the chord length C .



P8.114

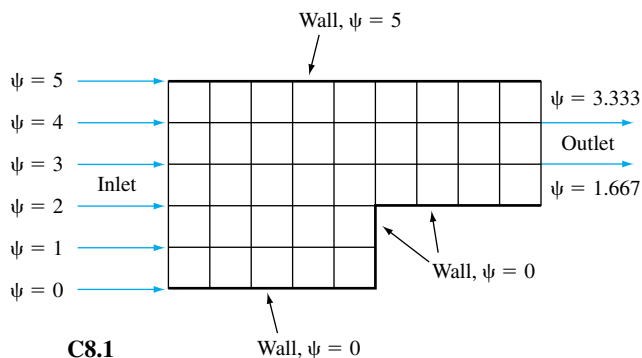
- P8.115** Use the explicit method of Eq. (8.115) to solve Prob. 4.85 numerically for SAE 30 oil at 20°C with $U_0 = 1$ m/s and $\omega = M$ rad/s, where M is the number of letters in your surname. (This author will solve the problem for $M = 5$.) When steady oscillation is reached, plot the oil velocity versus time at $y = 2$ cm.

Word Problems

- W8.1** What simplifications have been made, in the potential-flow theory of this chapter, which result in the elimination of the Reynolds number, Froude number, and Mach number as important parameters?
- W8.2** In this chapter we superimpose many basic solutions, a concept associated with *linear* equations. Yet Bernoulli's equation (8.3) is *nonlinear*, being proportional to the square of the velocity. How, then, do we justify the use of superposition in inviscid-flow analysis?
- W8.3** Give a physical explanation of circulation Γ as it relates to the lift force on an immersed body. If the line integral defined by Eq. (8.15) is zero, it means that the integrand is a perfect differential—but of what variable?
- W8.4** Give a simple proof of Eq. (8.42), namely, that both the real and imaginary parts of a function $f(z)$ are laplacian if $z = x + iy$. What is the secret of this remarkable behavior?
- W8.5** Figure 8.14 contains five body corners. Without carrying out any calculations, explain physically what the value of the inviscid fluid velocity must be at each of these five corners. Is any flow separation expected?
- W8.6** Explain the Kutta condition physically. Why is it necessary?
- W8.7** We have briefly outlined finite-difference and boundary-element methods for potential flow but have neglected the *finite-element* technique. Do some reading and write a brief essay on the use of the finite-element method for potential-flow problems.

Comprehensive Problems

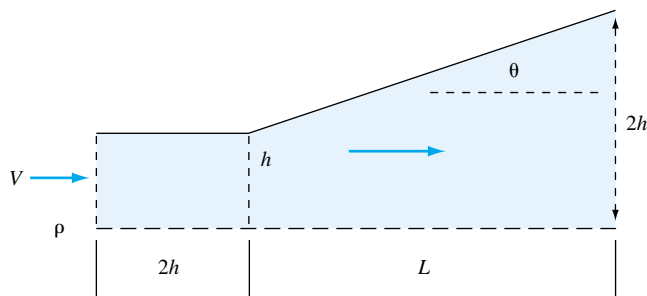
C8.1 Did you know that you can solve simple fluid mechanics problems with Microsoft Excel? The successive relaxation technique for solving the Laplace equation for potential-flow problems is easily set up on a spreadsheet, since the stream function at each interior cell is simply the average of its four neighbors. As an example, solve for the irrotational potential flow through a contraction, as given in Fig. C8.1. *Note:* To avoid the “circular reference” error, you must turn on the iteration option. Use the help index for more information. For full credit, attach a printout of your spreadsheet, with stream function converged and the value of the stream function at each node displayed to four digits of accuracy.



C8.2 Use an explicit method, similar to but not identical to Eq. (8.115), to solve the case of SAE 30 oil at 20°C starting from rest near a *fixed* wall. Far from the wall, the oil accelerates linearly, that is, $u_\infty = u_N = at$, where $a = 9 \text{ m/s}^2$. At $t = 1 \text{ s}$, determine (a) the oil velocity at $y = 1$

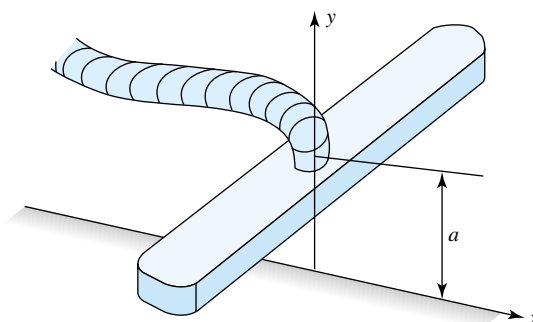
cm and (b) the instantaneous boundary-layer thickness (where $u \approx 0.99 u_\infty$). *Hint:* There is a nonzero pressure gradient in the outer (nearly shear-free) stream, $n = N$, which must be included in Eq. (8.114) and your explicit model.

C8.3 Consider plane inviscid flow through a symmetric diffuser, as in Fig. C8.3. Only the upper half is shown. The flow is to expand from inlet half-width h to exit half-width $2h$, as shown. The expansion angle θ is 18.5° ($L \approx 3h$). Set up a nonsquare potential-flow mesh for this problem, and calculate and plot (a) the velocity distribution and (b) the pressure coefficient along the centerline. Assume uniform inlet and exit flows.



C8.4 Use potential flow to approximate the flow of air being sucked up into a vacuum cleaner through a two-dimensional slit attachment, as in Fig. C8.4. In the x - y plane through the centerline of the attachment, model the flow as a line sink of strength $(-m)$, with its axis in the z -direction at height a above the floor. (a) Sketch the streamlines and locate any

stagnation points in the flow. (b) Find the magnitude of velocity $V(x)$ along the floor in terms of the parameters a and m . (c) Let the pressure far away be p_∞ , where velocity is zero. Define a velocity scale $U = m/a$. Determine the variation of dimensionless pressure coefficient, $C_p = (p - p_\infty)/(\rho U^2/2)$, along the floor. (d) The vacuum cleaner is most effective where C_p is a minimum, that is, where velocity is maximum. Find the locations of minimum pressure coefficient along the x -axis. (e) At which points along the x -axis do you expect the vacuum cleaner to work most effectively? Is it best at $x = 0$ directly beneath the slit, or at some other x location along the floor? Conduct a scientific experiment at home with a vacuum cleaner and some small pieces of dust or dirt to test your prediction. Report your results and discuss the agreement with prediction. Give reasons for any disagreements.



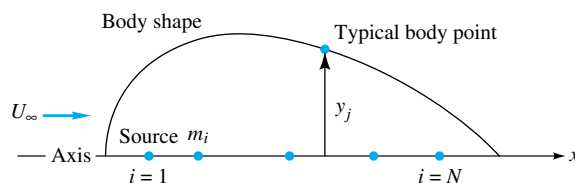
C8.4

C8.5 Consider a three-dimensional, incompressible, irrotational flow. Use the following two methods to prove that the viscous term in the Navier-Stokes equation is identically zero: (a) using vector notation; and (b) expanding out the scalar terms and substituting terms from the definition of irrotationality.

Design Projects

D8.1 In 1927, Theodore von Kármán developed a scheme to use a uniform stream, plus a row of sources and sinks, to generate an arbitrary closed-body shape. A schematic of the idea is sketched in Fig. D8.1. The body is symmetric and at zero angle of attack. A total of N sources and sinks are distributed along the axis within the body, with strengths m_i at positions x_i , for $i = 1$ to N . The object is to find the correct distribution of strengths which approximates a given body shape $y(x)$ at a finite number of surface locations and then to compute the approximate surface velocity and pressure. The technique should work for either two-dimensional bodies (distributed line sources) or bodies of revolution (distributed point sources).

For our body shape let us select the NACA 0018 airfoil, given by the formula in Prob. 8.114 with $t_{\max} = 0.18$. Develop the ideas stated above into N simultaneous algebraic equations which can be used to solve for the N unknown line source/sink strengths. Then program your equations for a computer, with $N \geq 20$; solve for m_i ; compute the surface velocities; and compare with the theoretical velocities for this shape in Ref. 12. Your goal should be to achieve accuracy within ± 1 percent of the classical results. If necessary, you should adjust N and the locations of the sources.



D8.1

D8.2 Modify Prob. D8.1 to solve for the point-source distribution which approximates an “0018” body-of-revolution shape. Since no theoretical results are published, simply make sure that your results converge to ± 1 percent.

D8.3 Consider water at 20°C flowing at 12 m/s in a water channel. A Rankine oval cylinder, 40 cm long, is to be placed parallel to the flow, where the water static pressure is 120 kPa . The oval’s thickness is a design parameter. Prepare a plot of the minimum pressure on the oval’s surface as a function of body thickness. Especially note the thicknesses where (a) the local pressure is 50 kPa and (b) cavitation first occurs on the surface.

References

- O. D. Kellogg, *Foundations of Potential Theory*, Dover, New York, 1969.
- J. M. Robertson, *Hydrodynamics in Theory and Application*, Prentice-Hall, Englewood Cliffs, NJ, 1965.
- L. M. Milne-Thomson, *Theoretical Hydrodynamics*, 4th ed., Macmillan, New York, 1960.
- I. G. Currie, *Fundamental Mechanics of Fluids*, 2d ed., McGraw-Hill, New York, 1993.
- S. V. Patankar, *Numerical Heat Transfer and Fluid Flow*, McGraw-Hill, New York, 1980.
- G. F. Carey and J. T. Oden, *Finite Elements: Fluid Mechanics*, vol. 6, Prentice-Hall, Englewood Cliffs, NJ, 1986.

7. C. A. Brebbia and J. Dominguez, *Boundary Elements—An Introductory Course*, 2d ed., Computational Mechanics Publications, Southampton, England, and McGraw-Hill, New York, 1991.
8. A. D. Moore, “Fields from Fluid Flow Mappers,” *J. Appl. Phys.*, vol. 20, 1949, pp. 790–804.
9. H. J. S. Hele-Shaw, “Investigation of the Nature of the Surface Resistance of Water and of Streamline Motion under Certain Experimental Conditions,” *Trans. Inst. Nav. Archit.*, vol. 40, 1898, p. 25.
10. R. H. F. Pao, *Fluid Dynamics*, Merrill, Columbus, OH, 1967.
11. A. M. Kuethe and C.-Y. Chow, *Foundations of Aerodynamics*, 5th ed., Wiley, New York, 1997.
12. I. H. Abbott and A. E. von Doenhoff, *Theory of Wing Sections*, Dover, New York, 1959.
13. B. Thwaites (ed.), *Incompressible Aerodynamics*, Clarendon Press, Oxford, England, 1960.
14. L. Prandtl, “Applications of Modern Hydrodynamics to Aeronautics,” *NACA Rep. 116*, 1921.
15. F. M. White, *Viscous Fluid Flow*, 2d ed., McGraw-Hill, New York, 1991.
16. C. S. Yih, *Fluid Mechanics*, McGraw-Hill, New York, 1969.
17. K. T. Patton, “Tables of Hydrodynamic Mass Factors for Translational Motion,” *ASME Winter Annual Meeting*, Paper 65-WA/UNT-2, 1965.
18. J. L. Hess and A. M. O. Smith, “Calculation of Nonlifting Potential Flow about Arbitrary Three-Dimensional Bodies,” *J. Ship Res.*, vol. 8, 1964, pp. 22–44.
19. K. H. Huebner, *The Finite Element Method for Engineers*, 3d ed., Wiley, New York, 1994.
20. J. C. Tannehill, D. A. Anderson, and R. H. Fletcher, *Computational Fluid Mechanics and Heat Transfer*, 2d ed., Taylor and Francis, Bristol, PA, 1997.
21. J. N. Newman, *Marine Hydrodynamics*, M.I.T. Press, Cambridge, MA, 1977.
22. H. Rouse, *Elementary Mechanics of Fluids*, Dover, New York, 1978.
23. J. H. Ferziger and M. Peric, *Computational Methods for Fluid Dynamics*, Springer-Verlag, New York, 1996.
24. C. Hirsch, *Numerical Computation of Internal and External Flows*, 2 vols., Wiley, New York, 1990.
25. K. A. Hoffmann and S. T. Chiang, *CFD for Engineers*, 2 vols., Engineering Education System, New York, 1993.
26. J. D. Anderson, *Computational Fluid Dynamics: The Basics with Applications*, McGraw-Hill, New York, 1995.
27. C. A. J. Fletcher, *Computational Techniques for Fluid Dynamics*, 2 vols., Springer Verlag, New York, 1997.
28. M. Deshpande, J. Feng, and C. L. Merkle, “Numerical Modeling of the Thermodynamic Effects of Cavitation,” *J. Fluids Eng.*, June 1997, pp. 420–427.
29. P. A. Libby, *An Introduction to Turbulence*, Taylor and Francis, Bristol, PA, 1996.
30. C. J. Freitas, “Perspective: Selected Benchmarks from Commercial CFD Codes,” *J. Fluids Eng.*, vol. 117, June 1995, pp. 208–218.
31. R. Martinuzzi and C. Tropea, “The Flow Around Surface-Mounted, Prismatic Obstacles in a Fully Developed Channel Flow,” *J. Fluids Eng.*, vol. 115, March 1993, pp. 85–92.
32. K. B. Shah and J. H. Ferziger, “Large Eddy Simulations of Flow Past a Cubic Obstacle,” *Thermosciences Division Report*, Dept. of Mechanical Engineering, Stanford University, Stanford, CA, 1996.
33. B. Galperin and S. A. Orszag (eds.), *Large Eddy Simulation of Complex Engineering and Geophysical Flows*, Cambridge University Press, New York, 1993.
34. W. J. Palm, *Introduction to MATLAB for Engineers*, McGraw-Hill, New York, 1998.
35. D. Hanselman and B. Littlefield, *The Student Edition of MATLAB*, Prentice-Hall, Upper Saddle River, NJ, 1997.
36. J. W. Hoyt and R. H. J. Sellin, “Flow Over Tube Banks—A Visualization Study,” *J. Fluids Eng.*, vol. 119, June 1997, pp. 480–483.